

AD _____

Award Number: W81XWH-06-1-0003

TITLE: Intra-Operative Dosimetry in Prostate Brachytherapy

PRINCIPAL INVESTIGATOR: Ameet Jain

CONTRACTING ORGANIZATION: Johns Hopkins University
Baltimore, MD 21218-2686

REPORT DATE: November 2007

TYPE OF REPORT: Annual Summary

PREPARED FOR: U.S. Army Medical Research and Materiel Command
Fort Detrick, Maryland 21702-5012

DISTRIBUTION STATEMENT: Approved for Public Release;
Distribution Unlimited

The views, opinions and/or findings contained in this report are those of the author(s) and should not be construed as an official Department of the Army position, policy or decision unless so designated by other documentation.

REPORT DOCUMENTATION PAGE				Form Approved OMB No. 0704-0188	
Public reporting burden for this collection of information is estimated to average 1 hour per response, including the time for reviewing instructions, searching existing data sources, gathering and maintaining the data needed, and completing and reviewing this collection of information. Send comments regarding this burden estimate or any other aspect of this collection of information, including suggestions for reducing this burden to Department of Defense, Washington Headquarters Services, Directorate for Information Operations and Reports (0704-0188), 1215 Jefferson Davis Highway, Suite 1204, Arlington, VA 22202-4302. Respondents should be aware that notwithstanding any other provision of law, no person shall be subject to any penalty for failing to comply with a collection of information if it does not display a currently valid OMB control number. PLEASE DO NOT RETURN YOUR FORM TO THE ABOVE ADDRESS.					
1. REPORT DATE 01-11-2007		2. REPORT TYPE Annual Summary		3. DATES COVERED 15 Oct 2005 – 14 Oct 2007	
4. TITLE AND SUBTITLE Intra-Operative Dosimetry in Prostate Brachytherapy				5a. CONTRACT NUMBER	
				5b. GRANT NUMBER W81XWH-06-1-0003	
				5c. PROGRAM ELEMENT NUMBER	
6. AUTHOR(S) Ameet Jain E-Mail: jain@cs.jhu.edu				5d. PROJECT NUMBER	
				5e. TASK NUMBER	
				5f. WORK UNIT NUMBER	
7. PERFORMING ORGANIZATION NAME(S) AND ADDRESS(ES) Johns Hopkins University Baltimore, MD 21218-2686				8. PERFORMING ORGANIZATION REPORT NUMBER	
9. SPONSORING / MONITORING AGENCY NAME(S) AND ADDRESS(ES) U.S. Army Medical Research and Materiel Command Fort Detrick, Maryland 21702-5012				10. SPONSOR/MONITOR'S ACRONYM(S)	
				11. SPONSOR/MONITOR'S REPORT NUMBER(S)	
12. DISTRIBUTION / AVAILABILITY STATEMENT Approved for Public Release; Distribution Unlimited					
13. SUPPLEMENTARY NOTES Original contains colored plates: ALL DTIC reproductions will be in black and white.					
14. ABSTRACT Favorable outcome in prostate brachytherapy critically depends on the accurate placement of radioactive sources in their planned locations. Unfortunately, there is variety of mechanical factors that cause the seeds to divert from their planned locations. While this problem has been known to brachytherapists, current technology does not allow for reliable localization of the implanted sources, thereby prohibiting the prediction and modification of seed distribution intra-operatively. The Research Objective of the proposal is to develop and evaluate ex-vivo a method for intra-operative localization of the implanted seeds in relation to the prostate, to facilitate in-situ dosimetric optimization and exit dosimetry. In particular, we will: [1] Registration of Ultrasound to Fluoroscopy (RUF): Develop methods for reconstruction of seed implants from X-ray fluoroscopy and spatially register them to the prostate anatomy identified in TRUS [2] System Integration: Integrate the above methods in a software package and link it with the FDA-approved CMS Interplant® prostate brachytherapy system to enable in-situ dosimetry calculation [3] Experimental Validation: Evaluate the performance of the RUF system on phantoms and pre-recorded patient data.					
15. SUBJECT TERMS Prostate Brachytherapy, X-ray reconstruction, C-arm, TRUS					
16. SECURITY CLASSIFICATION OF:			17. LIMITATION OF ABSTRACT	18. NUMBER OF PAGES	19a. NAME OF RESPONSIBLE PERSON
a. REPORT	b. ABSTRACT	c. THIS PAGE			USAMRMC
U	U	U	UU	69	19b. TELEPHONE NUMBER (include area code)

Table of Contents

Introduction.....	4
Body.....	4
Key Research Accomplishments.....	7
Reportable Outcomes.....	7
Conclusions.....	7
References.....	8
Appendices.....	9

Progress Report Summary

Project Year 2 (2006 –2007)

A INTRODUCTION

For several decades, the definitive treatment for low and medium risk prostate cancer was radical prostatectomy or external beam radiation therapy, but low dose rate permanent seed brachytherapy (shortly brachytherapy) today can achieve equivalent outcomes. Brachytherapy, if accurately executed, can achieve a sharp demarcation between the treated volume and healthy structures, and thereby achieve superior tumor control with reduced morbidity. In contemporary practice, however, faulty needle and source placement often cause insufficient dose to the cancer and/or inadvertent radiation of the rectum, urethra, and bladder. Another fallacy of the current implant techniques is that reliable and accurate exit dosimetry is not possible. The contribution of the proposed research will be making C-arm fluoroscopy available for safe, simple, and robust intra-operative localization of brachytherapy sources relative to the prostate. We will develop a method for the registration of ultrasound to fluoroscopy (RUF), to fuse TRUS (Trans-rectal ultrasound can view the prostate but not the seeds) with C-arm fluoroscopy (which is capable of viewing the seeds but not the prostate). This feature will allow for dosimetric optimization of the prostate brachytherapy implants and exit dosimetry before the patient is released from the operating room; thereby enabling significant improvement on current clinical practice. A further promise is that fluoroscopy-based exit dosimetry may obviate CT-based post-implant dosimetry.

B BODY

B.1 Brief System Concept

The system concept for registration of ultrasound to fluoroscopy (RUF) is summarized in Figure 1. The fluoroscope is calibrated and corrected from image distortion pre-operatively. The implant procedure starts as usual: TRUS is used to guide each individual needle and a C-arm placed over the patient's abdomen. The C-arm is tracked with an X-ray fiducial system called FTRAC that is composed of optimally selected polynomial space curves. The fiducials are mounted rigidly to the TRUS frame in the

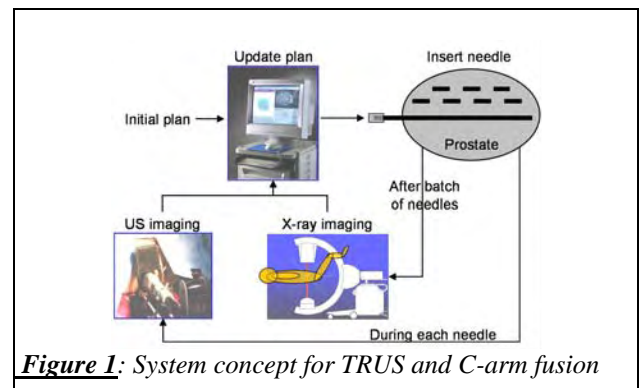


Figure 1: System concept for TRUS and C-arm fusion

field of view in a known calibrated pose relative to the TRUS, thereby providing spatial registration between the C-arm and TRUS. Upon implanting a batch of needles (typically a row of needles), we collect a set of TRUS and C-arm images. The locations of the implanted seeds are recovered from the C-arm fluoroscopy images with the use of a network flow based method called MARSHAL that provides seed segmentation, matching, and reconstruction method. Then the cloud of seeds is superimposed over the spatially co-registered TRUS images. The 3D dose distribution is rapidly calculated from the union of the already and yet to be implanted seeds. The dose distribution is analyzed with tools currently available in the brachytherapy system used. Then the implant plan can be optimized to account for discrepancies from the ideal dose distribution. The procedure continues with the next batch of needles in the cycle described above. After the last needle, a complete dosimetry check is performed, which provides a final opportunity to patch up any cold spots with additional seeds.

B.2 Proposed Statement of Work

We proposed to develop a method for the registration of ultrasound to fluoroscopy (RUF) to allow for intra-operative dosimetry in prostate brachytherapy and prototype mathematical algorithms (Aim-1), integrate them with an existing FDA approved prostate brachytherapy system that provides dosimetry analysis (Aim-2), and evaluate the system experimentally on phantoms and pre-recorded patient data (Aim-3). Algorithmic design (Aim-1) and experimental evaluation (Aim-3), will progress hand in hand. System integration (Aim-2) will be

performed immediately when a workable subset of RUF package becomes available from Aim-1 and again revisited towards at the end of the project. Therefore, the timeline will be somewhat non-linear. The detailed statement of work was as follows:

- Aim-1: Registration of Ultrasound to Fluoroscopy (RUF):** Develop a methods for reconstruction of seed implants from X-ray fluoroscopy and spatially registering them to the prostate anatomy identified in TRUS
- Aim-2: System Integration:** Integrate the above methods in a software package and link it with the FDA-approved CMS Interplant® prostate brachytherapy system to enable dosimetry calculation
- Aim-3: Experimental Validation:** Evaluate the performance of the RUF system on phantoms and pre-recorded patient data. (Neither of which require an IRB approval)

B.3 Progress Report for Second Year

In Aim1: the three main aspects were (a) Registration of X-ray to ultrasound; (b) C-arm tracking; (c) Seed reconstruction.; and (d) C-arm calibration.

These issues were satisfactorily addressed in the year-1 report.

In Aim2: we had reported preliminary work and proposed approach towards the system integration in the year 1 annual report. We made further progress and completed this integration process in the second year.

We employ a regular clinical brachytherapy setup, without alteration, including a treatment planning workstation and stabilizer/stepper (Interplant®, CMS, St Louis), TRUS (B&K Medical), C-arm (GE OEC, Salt Lake City, UT). The C-arm is interfaced with a standalone laptop computer through an NTSC video line and frame grabber.

Workflow: The clinical workflow is identical to the standard procedure until the clinician decides to run a reconstruction and optimization, typically at each half of the procedure. A set of C-arm images are collected with as wide separation as possible (15°) and transferred to the laptop. After processing the fluoro images, the seeds are reconstructed in TRUS space and exported to the Interplant®. The physician uses standard Interplant® features to analyze the dose and modify the remainder of the implant plan, in order to optimize it. The procedure concludes when the exit dosimetry shows no cold spots.

Dosimetry Analysis and Implant Optimization: The seed locations are exported in template coordinates to the Interplant® system. A software patch added to the Interplant® then removes the already implanted seeds from the complete implant plan, thereby producing a “residual implant plan”. The total dose is calculated by combining the seeds in the residual implant plan and the seeds already implanted. The physician uses standard Interplant® tools (isodose coverage, DVH, etc.) for dose analysis. If it is necessary to change the total dose distribution, then the residual plan is modified with standard Interplant® dose planning functions. Note that as the procedure progresses, the residual plan reduces and there is less and less degree of freedom to optimize the overall dose distribution. In fact, at some point it becomes impossible to reduce dose in the hot spots, because once seeds are delivered, they cannot be taken back. Fortunately, we always can fix cold spots by adding more seeds to the implant plan.

In Aim3: we proposed to evaluate the workspace constraints and the overall performance of the system. In addition to the results presented at the end of year 1, further extensive validation was conducted, including detailed phantom experiments for engineering validation and some clinical validation.

Soft Training Phantoms: We fully seeded three standard prostate brachytherapy phantoms with realistic implant plans (45, 49, 87 seeds). Seed locations reconstructed from fluoro using a realistic 15° net C-arm motion were compared to corresponding locations segmented manually in CT (1mm slice thickness). The average seed reconstruction error wrt the FTRAC fiducial was below 1.5mm (0.2mm relative accuracy – there was a translation offset). These results made us confident that the system would perform reasonably for actual humans. To measure the full system error, 5 needles (tips) were inserted, reconstructed and exported into a standard prostate brachytherapy phantom. Manual segmentation of the needles in TRUS (sagittal for depth and transverse for X-Y) provided ground truth locations. The average residual error for the 5 needle tips was 3.4 mm. There is about a 3mm constant translation offset/bias, due to cascading effects in the Interplant® pre-operative registration, the reconstruction process & US beam thickness. After correcting for these biases, the mean residual registration error dropped to 0.82mm (STD=0.17mm).

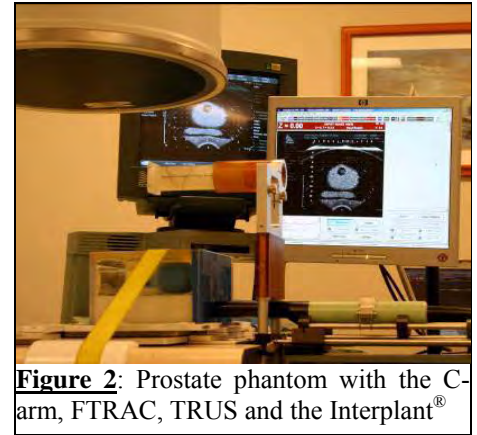


Figure 2: Prostate phantom with the C-arm, FTRAC, TRUS and the Interplant®

Clinical Data: From a small cohort of 6 patients so far we have treated 4. An actual OR picture in Figure 2 shows the setup with the FTRAC fluoroscopy tracking fiducial mounted over the template and TRUS stepper.

Implant reconstruction and dose analysis was performed halfway of the implant and also in the end (an additional one was used for a research comparison to post-op CT). *In all the patients, the final dosimetry detected one or more cold spots (Figure 5).* In the fourth patient, 9 additional seeds (initial 67) were inserted to bring up V100 dose to the desired level. Apparently, the physician grew quickly to trust

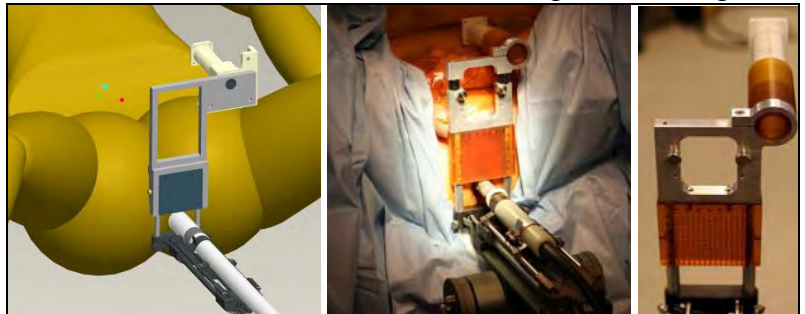


Figure 3: Fluoroscope tracking (FTRAC) fiducial: Mounting over the abdomen in CAD model (left) and actual clinical setup (middle), the connector between FTRAC and template (right).

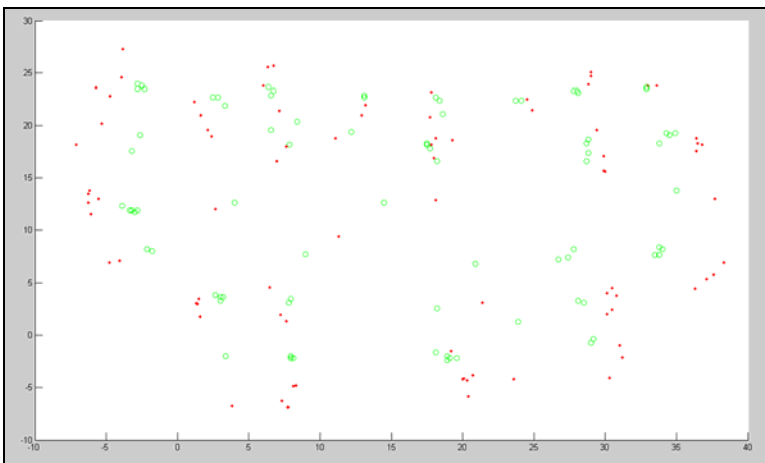


Figure 4: Intra-operative visualization of the edema is possible with the system. The 'planned' (green) versus the 'reconstructed' (red) seed positions as seen in the X-Y plane (template view). The image acquisition is at end of procedure. A trend of outward radiation of the seeds from their initial seed position is observed. This is due to edema occurring during the procedure.

the system in catching cold spots, and instead became very cautious not to create hot spots. Importantly, all patients were released from the operating room with satisfactory V100/V90 dose and favorable DVH for all relevant structures. The use of the system added about 45 minutes to the OR time, with each set of three implant reconstructions taking about 15 minutes, including image capture, processing, 3D reconstruction, and dosimetry evaluation. We anticipate needing only a single reconstruction in the post-research phase. *Intra-operative visualization of edema was also possible with the system, which was found to be significant in 2 patients of the total 4 (Figure 4).* The seeds showed a clear tendency of outward migration from their drop positions as the procedure progressed. Although comparative quantitative

conclusions cannot be made based on the limited available data, comparison of the intra-operative dosimetry with the post-implant CT reveal close correlation.

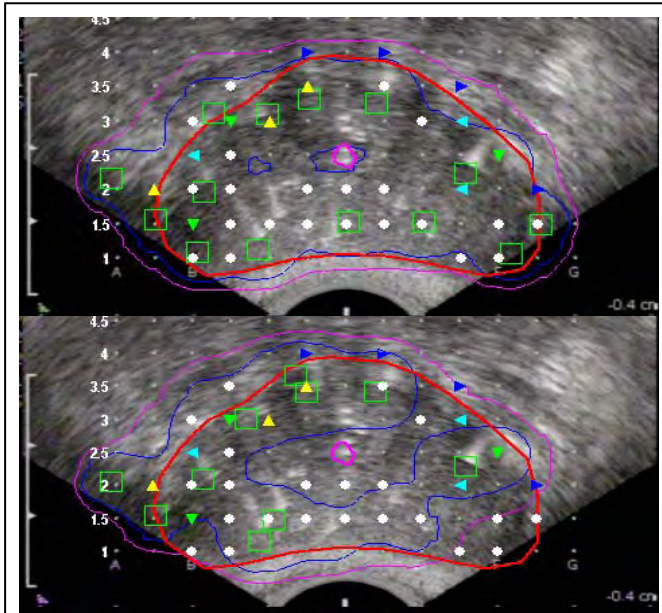


Figure 5: The system is able to detect *cold spots*. The V100 contours (blue) as assumed by the planning system (top) and as computed by the proposed system (bottom). In this patient, 3 cold spots were discovered in exit dosimetry. The prostate boundary is delineated by dark red contours and the green squares mark current seed coordinates. Note that the system also detected 4 seeds that have drifted out of slice, owing largely to the swelling effects of edema.

C KEY RESEARCH ACCOMPLISHMENTS

1. Ability to intra-operatively compute 3D seed locations in prostate brachytherapy.
2. Minimal alterations to the current prostate brachytherapy clinical protocol.
3. A complete integrated clinical research system ready for multi-center trials.
4. Extensive validation – both on phantom data as promised, and additionally also on real clinical data.

D KEY TRAINING ACCOMPLISHMENTS

1. Close interaction with clinicians, medical physicists, and industry advisors.
2. Various international training courses, workshops & conferences in medical imaging processing.
3. Ability to do independent research, including mentoring undergraduate students for their research.
4. Successful completion of the PhD requirements.

E REPORTABLE OUTCOMES

1. Publications in leading conferences and journals, as listed in the publications section (including three flagship conference publications in MICCAI).
2. A poster award at SPIE Medical Imaging 2007 for work on C-arm calibration.
3. A prototype for subsequent commercialization and integration into the Interplant software.

F CONCLUSIONS

In conclusion, the system was exquisitely accurate in technical (phantom) trials and has shown usefulness and great potential in a limited trial. Further development is underway to reduce added time and manual labor in the OR. We have addressed the issue of intra-operative reconstruction of brachytherapy seeds, with minimal

alteration to the current clinical protocol or any significant increase in cost. A prototype system for clinical trials and potential commercialization has also been tested & implemented.

So what: The success of brachytherapy chiefly depends on our ability to intra-operatively cover the prostate with sufficient radiation while still avoiding excessive radiation to surrounding organs. Currently, such level of precision is not always achievable even by the most experienced physicians. Thus many implants fail or cause severe side effects owing to faulty seed placement, a problem what still cannot be corrected in the operating room. Our results indicate the feasibility of a system that could achieve intra-operative localization of the implanted seeds in relation to the prostate, to allow for in-situ dosimetric optimization and exit dosimetry. This ability to perform intra-operative dosimetry may change the standard of care in brachytherapy by allowing the physician to achieve technically excellent brachytherapy implants, resulting in improved disease control and quality of life for a large and steadily growing group of patients.

G PUBLICATIONS (List of publications in year 2 arising from the grant, sorted by publication date)

A Jain, A Deguet, I Iordachita, G Chintalapani, J Blevins, Y Le, E Armour, C Burdette, D Song, G Fichtinger: *Detection of Intra-operative Edema in Prostate Brachytherapy*. SPIE Medical Imaging Feb 2008 (accepted)

A Jain, A Deguet, I Iordachita, G Chintalapani, J Blevins, Y Le, E Armour, C Burdette, D Song, G Fichtinger: *Intra-operative Guidance in Prostate Brachytherapy Using an non-isocentric C-arm*. Tenth International Conference on Medical Image Computing and Computer-Assisted Intervention (MICCAI), Oct 2007

X Liu, **A Jain**, G Fichtinger: *Prostate Implant Reconstruction with Discrete Tomography*. Tenth International Conference on Medical Image Computing and Computer-Assisted Intervention (MICCAI), Oct 2007

Labat C, **A Jain**, G Fichtinger, J Prince: *Toward optimal matching for 3D reconstruction of brachytherapy seeds*. Tenth International Conference on Medical Image Computing and Computer-Assisted Intervention (MICCAI), Oct 2007

A Jain, A Deguet, I Iordachita, J Blevins, Y Le, E Armour, C Burdette, D Song, G Fichtinger: *C-arm based Intra-operative Dosimetry in Prostate Brachytherapy*, AAPM, July 2007

A. **Jain**, M An, N Chitphakdithai, G Chintalapani, G Fichtinger: *C-arm Calibration - is it really Necessary?*, SPIE Feb 2007 **Winner of poster award (Honorably mentioned)**.

G Chintalapani, **A Jain**, RH Taylor: *Statistical Characterization of C-arm Distortion with Application to Intra-Operative Distortion Correction*. SPIE Medical Imaging Feb 2007.

D Burkhardt, **A Jain**, G Fichtinger: *A Cheap and Easy Method for 3D C-arm Reconstruction using Elliptic Curves*. SPIE Medical Imaging Feb 2007.

Intra-operative 3D Guidance in Prostate Brachytherapy using a non-isocentric C-arm ^{*}

A. Jain^{1,3}, A. Deguet¹, I. Iordachita¹, G. Chintalapani¹, J. Blevins², Y. Le¹, E. Armour¹, C. Burdette², D. Song¹, G. Fichtinger¹

1 - Johns Hopkins University; 2 - Acoustic MedSystems Inc.; 3 - Philips Research North America

Abstract. Intra-operative guidance in Transrectal Ultrasound (TRUS) guided prostate brachytherapy requires localization of inserted radioactive seeds relative to the prostate. Seeds were reconstructed using a typical C-arm, and exported to a commercial brachytherapy system for dosimetry analysis. Technical obstacles for 3D reconstruction on a non-isocentric C-arm included pose-dependent C-arm calibration; distortion correction; pose estimation of C-arm images; seed reconstruction; and C-arm to TRUS registration. In precision-machined hard phantoms with 40-100 seeds, we correctly reconstructed 99.8% seeds with a mean 3D accuracy of 0.68 mm. In soft tissue phantoms with 45-87 seeds and clinically realistic 15° C-arm motion, we correctly reconstructed 100% seeds with an accuracy of 1.3 mm. The reconstructed 3D seed positions were then registered to the prostate segmented from TRUS. In a Phase-1 clinical trial, so far on 4 patients with 66-84 seeds, we achieved intra-operative monitoring of seed distribution and dosimetry. We optimized the 100% prescribed iso-dose contour by inserting an average of 3.75 additional seeds, making intra-operative dosimetry possible on a typical C-arm, at negligible additional cost to the existing clinical installation.

1 Introduction

With an approximate annual incidence of 220,000 new cases and 33,000 deaths (United States) prostate cancer continues to be the most common cancer in men. Transrectal Ultrasound (TRUS) guided permanent low-dose-rate brachytherapy (insertion of radioactive seeds into the prostate) has emerged as a common & effective treatment modality for early stage low risk prostate cancer, with an expected 50,000 surgeries every year. The success of brachytherapy (i.e. maximizing its efficacy while minimizing its co-morbidity) chiefly depends on our ability to tailor the therapeutic dose to the patient's individual anatomy. The main limitation in contemporary brachytherapy is intra-operative tissue expansion (edema), causing incorrect seed placement, which may potentially lead to insufficient dose to the cancer and/or excessive radiation to the rectum, urethra, or bladder. The former might permit the cancer to relapse, while the latter causes adverse side effects like rectal ulceration. According to a comprehensive review by the American Brachytherapy Society [1], *the pre-planned technique*

^{*} Supported by DoD PC050170, DoD PC050042 and NIH 2R44CA099374

used for permanent prostate brachytherapy has limitations that may be overcome by intra-operative planning.

Prostate brachytherapy is almost exclusively performed under TRUS guidance. Various researchers have tried to segment the seeds from TRUS images by linking seeds with spacers, using X-rays to initialize segmentation, using vibro-acoustography or transurethral ultrasound as a new imaging modality, or segmenting them directly in TRUS images by using corrugated seeds that are better visible than conventional ones [2]. But even when meticulously hand-segmented, up to 25% of the seeds may remain hidden in ultrasound. C-arms are also ubiquitous, though used only for gross visual assessment of the implanted seed positions (approximately 60% of the practitioners using it in the operating room [3]). In spite of significant efforts that have been made towards computational fluoroscopic guidance in general surgery [4], C-arms cannot yet be used for intra-operative brachytherapy guidance due to a plethora of technical limitations. While several groups have published protocols and clinical outcomes favorably supporting C-arm fluoroscopy for intra-operative dosimetric analysis [5–7], this technique is yet to become a standard of care across hospitals. In this paper we report a system to reconstruct 3D seed positions (visible in X-ray) and spatially register them to the prostate (visible in TRUS). Our **primary contribution** is our ability to use any typical non-isocentric uncalibrated C-arm present in most hospitals, in comparison to the use of calibrated isocentric machines [5, 6] or an approximate reconstruction [7], as reported in the literature.

2 Methods and Materials

The system is designed to easily integrate with commercial brachytherapy installations. We employ a regular clinical brachytherapy setup, without alteration, including a treatment planning workstation & stabilizer/stepper (Interplant®, CMS, St Louis), TRUS (B&K Medical Pro Focus) and a C-arm (GE OEC 98/9900). The C-arm is interfaced with a laptop through an NTSC video line and frame grabber, making the image capture independent of the C-arm model.

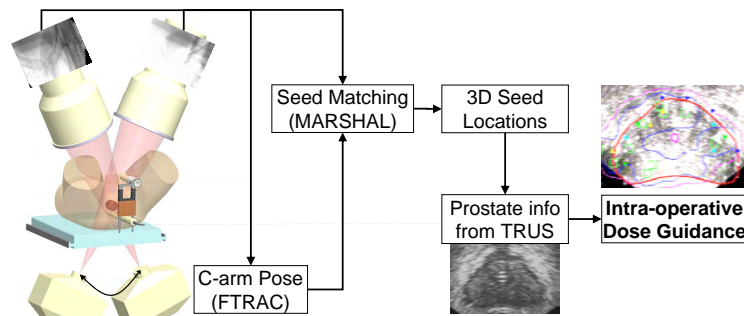


Fig. 1. Overview of the proposed solution. The FTRAC fiducial tracks C-arms, and also registers TRUS to C-arm images, making quantitative brachytherapy possible.

Workflow: The clinical workflow (Fig. 1) is identical to the standard procedure until the clinician decides to run a reconstruction and optimization. A set of C-arm images are collected with *a separation as wide as clinically possible* ($10-15^\circ$ around AP-axis) and synchronously transferred to the laptop. After processing the images, the seeds are reconstructed and exported to the Interplant[®] system. The physician uses standard Interplant[®] tools to analyze, optimize and modify the remainder of the plan. The procedure concludes when the exit dosimetry shows no cold spots (under-radiated locations).

Numerous technical obstacles have to be overcome to realize C-arm based intra-operative dosimetry: (a) C-arm calibration; (b) image distortion correction; (c) pose estimation of C-arm images; (d) seed reconstruction; (e) registration of C-arm to TRUS; (f) dosimetry analysis; and finally (g) implant optimization. We have developed a system that overcomes these limitations in providing quantitative intra-operative dosimetry. In what follows, we will describe briefly each component of the system, skipping the mathematical framework for lack of space.

C-arm Source Calibration and Image Distortion: Since both C-arm calibration and distortion are pose-dependent, contemporary fluoroscopy calibrates/distortion-corrects at each imaging pose using a cumbersome calibration-fixture, which is a significant liability. Our approach is a complete departure. Using a mathematical & experimental framework, we demonstrated that calibration is not critical for prostate seed reconstruction. Just an approximate pre-operative calibration suffices [8]. The central intuition is that object reconstruction using a mis-calibrated C-arm changes only the absolute positions of the objects, but not their relative ones (Fig. 2). Additionally, statistical analysis of the distortion in a 15° limited workspace around the AP-axis revealed that just a pre-operative correction can reduce the average distortion from 3.31 mm to 0.51 mm, sufficient for accurate 3D reconstruction. The numbers are expected to be similar for other C-arms too.

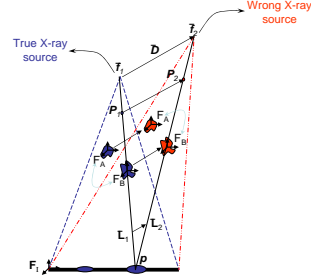


Fig. 2. Mis-calibration conserves relative reconstruction between objects A and B (eg. seeds).

Pose Estimation: The most critical component for 3D reconstruction is C-arm pose estimation. C-arms available in most hospitals do not have encoded rotational joints, making the amount of C-arm motion unavailable. C-arm tracking using auxiliary trackers is expensive, inaccurate in the presence of metal (EM tracking) or intrudes in the operating room (optical tracking). There has been some work on fiducial based tracking, wherein a fiducial (usually large for accuracy) is introduced in the X-ray FOV and its projection in the image encodes the 6 DOF pose of the C-arm. We proposed a new fluoroscope tracking (FTRAC) [9] fiducial design that uses an ellipse (key contribution), allowing for a small ($3 \times 3 \times 5$ cm) yet accurate fiducial. In particular, the small size makes it easier to

be always in the FOV & to be robust to image distortion. Extensive phantom experiments indicated a mean tracking accuracy on distorted C-arms of 0.56 mm in translation and 0.25° in rotation, an accuracy comparable to expensive external trackers.

Seed Segmentation: We developed an automated seed segmentation algorithm that employs the morphological top-hat transform to perform the basic seed segmentation, followed by thresholding, region labeling, and finally a two-phase classification to segment both single seeds & clusters. The result of the segmentation is verified on the screen to allow for a manual bypass by the surgeon.

Seed Correspondence & Reconstruction: The 3D coordinates of the implanted seeds can now be triangulated by resolving the correspondence of seeds in the multiple X-ray images. We formalized seed correspondence to a network-flow-based combinatorial optimization, wherein the desired solution is the flow with minimum cost. Using this abstraction, we proposed an algorithm (MARSHAL [10]) that runs in cubic-time using any number of images. In comparison, previous solutions have predominantly been heuristic explorations of the large search space (10^{300}). In addition, the framework also robustly resolves all the seeds that are hidden in the images (typically 4-7% due to the high density). MARSHAL typically reconstructs 99.8% of the seeds and runs in under 5s in MATLAB (a 95% minimum-detection-rate is usually deemed sufficient [11]).

Registration of C-arm to TRUS: The FTRAC is attached to the needle-insertion template by a precisely machined mechanical connector (Fig. 4) in a known relative way (pre-calibration). The template has already been calibrated to TRUS as per the usual clinical protocol. Thus a simple application of the various known frame transformations, registers the 3D seeds (FTRAC) to the prostate (TRUS).

System Implementation, Dosimetry Analysis and Implant Optimization: We have integrated

all the above functions into a MATLAB program with a GUI. The package runs on a laptop that sends reconstructed seed positions (in template coordinates) to the Interplant[®] system. In order to not require a new FDA approval, we maintain the integrity of the FDA-approved Interplant[®] by not modifying the commercial software, and instead use a text file to export the 3D seed locations. The physician uses standard Interplant[®] tools (isodose coverage, etc.) for dose analysis, and if needed, modifies the residual plan to avoid hot spots or fill in cold spots. This process can be repeated multiple times during the surgery.

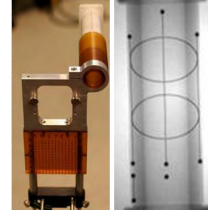


Fig. 3. The FTRAC fiducial mounted over the seed-insertion needle template using a mechanical connector. An X-ray image of the same.

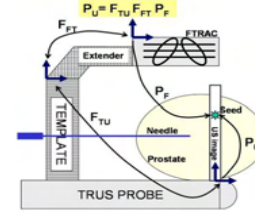


Fig. 4. FTRAC & template pre-calibration using a rigid mount.

3 Phantom Experiments and Results

We have extensively tested the system and its components in various phantoms and in an ongoing Phase-1 clinical trial. To do so, we introduce the terms **absolute** and **relative** reconstruction errors. Using X-ray images, the seeds are reconstructed with respect to (w.r.t.) the FTRAC frame. In experiments where the ground truth location of the seeds w.r.t. the FTRAC is known, the comparative analysis is called absolute accuracy. Sometimes (eg. in patients), the true seed locations w.r.t. the FTRAC are not available and the reconstruction can only be compared to the seeds extracted from post-op data (using a rigid point-cloud transform), in which case the evaluation is called relative accuracy.

Solid Seed Phantom: An acetol (Delrin) phantom consisting of ten slabs (5mm each) was fabricated (Fig. 5 (a)). This phantom provides a multitude of implants with sub-mm ground truth accuracy. The fiducial was *rigidly* attached to the phantom in a known way, establishing the accurate ground truth 3D location of each seed. Realistic prostate implants (1.56 seeds/cc, 40-100 seeds) were imaged within a 30° cone around the AP-axis. The true correspondence was manually established by using the 3D locations, known from the precise fabrication. Averaged results indicate that we correctly match 98.5% & 99.8% of the seeds using 3 & 4 images (100 & 75 total trials) respectively. The mean 3D absolute reconstruction accuracy was 0.65 mm (STD 0.27 mm), while the relative accuracy was 0.35 mm. Furthermore, using 4 images yielded only one poorly mis-matched seed from the 75 datasets, suggesting the use of 4 images for better clinical guidance.

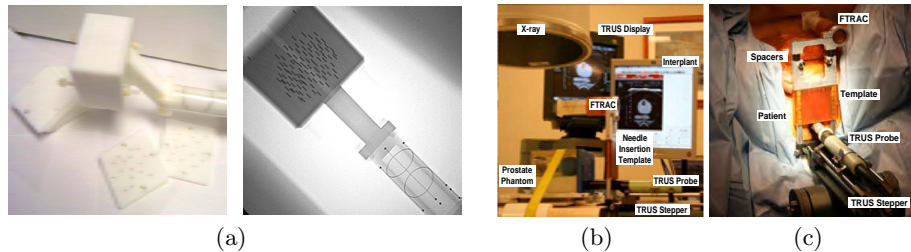


Fig. 5. (a) An image of the solid seed phantom attached to the fiducial with a typical X-ray image of the combination. (b) An annotated image of the experimental setup for the training phantom experiment. (c) The clinical setup from the Phase-I clinical trial

Soft Training Phantoms: We fully seeded three standard prostate brachytherapy phantoms (Fig. 5 (b)) with realistic implant plans (45, 49, 87 seeds). Seed locations reconstructed from fluoro using realistic (maximum available clinically) image separation (about 15°) were compared to their corresponding ground truth locations segmented manually in CT (1mm slice thickness). Additionally, the 45 & 87-seed phantoms were rigidly attached to the FTRAC, providing the absolute ground truth (from CT). The 49-seed phantom was used to conduct a full scale

practice-surgery, in which case the 3D reconstruction could be compared only to the seed cloud from post-op CT (without FTRAC), providing just relative accuracy. *Note that our reconstruction accuracy (as evident from the previous experiments) is better than the CT resolution.* The absolute reconstruction errors for the 45, 87-seed phantoms were 1.64 mm & 0.95 mm (STD 0.17 mm), while the relative reconstruction errors for the 45, 49, 87-seed phantoms were 0.22 mm, 0.29 mm, 0.20 mm (STD 0.13 mm). A mean translation shift of 1.32 mm was observed in the 3D reconstructions, predominantly due to the limited C-arm workspace (solid-phantom experiments with 30° motion have 0.65 mm accuracy). It was observed that the shift was mostly random & not in any particular direction. Nevertheless, the accuracy is sufficient for brachytherapy, especially since a small shift still detects the cold spots.

Patients: A total of 11 batches of reconstructions were carried out on 4 patients with 2 – 3 batches/patient & 22 – 84 seeds/batch. Since the seeds migrate by the time a post-operative CT is taken, there is no easy ground truth for real patients. Hence, for each reconstruction, 5 – 6 additional X-ray images were taken. The reconstructed 3D seed locations were projected on these additional images and compared to their segmented corresponding 2D locations. The results from 55 projections gave a 2D mean error of 1.59 mm (STD 0.33 mm, max 2.44 mm), indicating a sub-mm 3D accuracy (errors get magnified when projected).

Registration Accuracy: To measure the accuracy of the fiducial to template registration, three batches of five needles each were inserted randomly at random depths into the template. Their reconstructed tip locations were then compared to their true measured locations (both in template coordinates). The limited-angle image-capture protocol was kept similar to that used in the clinic. The average absolute error (reconstruction together with registration) was 1.03 mm (STD 0.20 mm), while the average relative error was 0.36 mm (STD 0.31 mm), with an average translation shift of 0.97 mm.

System Accuracy: To measure the full system error, 5 needles (tips) were inserted into a prostate brachytherapy training phantom, reconstructed in 3D and exported to the Interplant[®] software. Manual segmentation of the needles in TRUS images (sagittal for depth and transverse for X-Y) provided ground truth. The mean absolute error for the 5 needle tips was 4 mm (STD 0.53 mm), with a translation shift of 3.94 mm. In comparison, the relative error for the complete system was only 0.83 mm (STD 0.18 mm). The shift can mainly be attributed to a bias in the Template-TRUS pre-calibration (~ 3 mm) done as part of current clinical practice, & in the 3D reconstruction (~ 1 mm). Nevertheless, we removed this shift in the clinical cases by applying a translation-offset to the reconstructed X-ray seed coordinates. This offset was intra-operatively estimated by comparing the centroid of the reconstructed seeds with that of the planned seed locations, and by aligning the two together. Note that the centroid is a first-order statistic and robust to any spatially symmetric noise/displacement model. Though a heuristic, it provided excellent qualitative results according

to the surgeon, who read the visual cues at the reconstructed seed locations in TRUS images. Based on the experiments so far and the surgeon’s feedback, the overall accuracy of the system is expected to be $1 - 2\text{ mm}$ during clinical use.

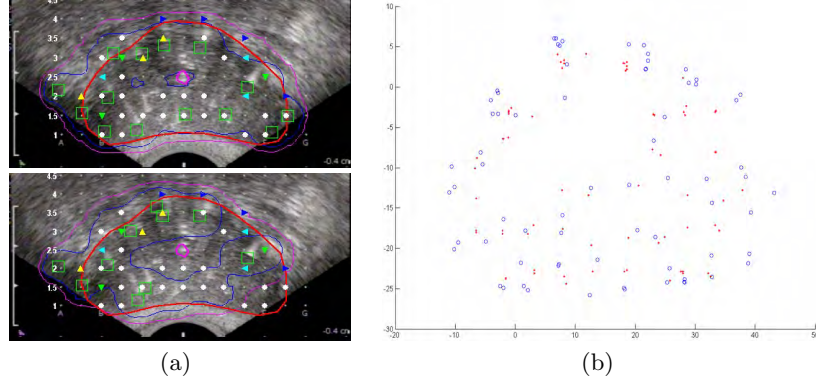


Fig. 6. (a) The system is able to detect cold spots. The 100% iso-dose contours (pink) as assumed by the planning system (top) and as computed by the proposed system (bottom), discovering 2 cold spots. Red marks the prostate boundary. The green squares delineate the seed coordinates, detecting 4 seeds that had drifted out of slice. (b) The system can visualize intra-operative edema (mean 4.6 mm, STD 2.4 mm, max 12.3 mm). The 'planned' (red) versus the 'reconstructed' (blue) seed positions as seen in the template view. A trend of outward radiation from their initial locations is observed.

Phase-I Clinical Trial: We have treated 4 patients so far (Fig. 5 (c)), out of a total of 6 that will be enrolled. Intra-operative dosimetry was performed halfway during the surgery, at the end, and after additional seed insertions. The current protocol adds 15 minutes to the OR time for each reconstruction, including the capture of extra images (validation), reconstruction, and dosimetry optimization. In regular clinical practice, we anticipate the need for only a single exit-dosimetry reconstruction, increasing the OR time by about 10 minutes. *In all the patients the final dosimetry detected cold spots* (Fig. 6 (a)). The clinician grew quickly to trust the system in detecting cold spots, and instead minimized potential hot spots during the surgery. All patients were released from the operating room with satisfactory outcomes. *Intra-operative visualization of edema (prostate swelling) was also possible* (Fig. 6 (b)), which was found to be 0.73, 4.64, 4.59, 4.05 mm (STD 1.1, 2.2, 2.34, 2.37 mm). *The seeds (and hence the prostate) showed a clear tendency for outward migration from their drop positions (with maximums up to 15 mm)*. Edema is the single largest factor that makes the perfect delivery of the pre-planned dose nearly impossible. In almost all the patients, towards the end of the surgery, it was found that the apex of the prostate (surgeon-end) was under-dosed. The medical team found the intra-operative visualization of under-dosed regions valuable, inserting an additional 1, 2, 3, 9 seeds to make the 100% prescribed iso-dose contour cover the prostate. A further comparison of the exit implant to Day-0 CTs (2 mm slices) showed mean errors of 5.43, 6.16, 3.13,

5.15 mm (STD 2.46, 2.96, 2.02, 2.71 mm), indicating a further post-operative seed migration. Though, post-operative seed migration is an inherent limitation in brachytherapy, surgeons usually accommodate for it by slightly over-dosing the patient (note that sub-mm seed placement is non-critical). A study with 40 patients is currently being planned, to make a statistically relevant evaluation of the medical benefit of the system using clinical indicators.

4 Conclusion, Shortcomings and Future Work

A system for brachytherapy seed reconstruction has been presented, with extensive phantom and clinical trials. The absolute seed reconstruction accuracy from phantom trials is 1.3 mm using 15° C-arm motion, sufficient for detection of any cold spots. It shows usefulness and great potential from the limited Phase-1 patient trials. The system (a) requires no significant hardware; (b) does not alter the current clinical workflow; (c) can be used with any C-arm; & (d) integrates easily with any pre-existing brachytherapy installation, making it economically sustainable and scalable. There is some added radiation to the patient, though insignificant when compared to that from the seeds. Though not critical, primary shortcomings include (a) 15 minute additional OR time; (b) supervision during segmentation; & (c) a small translation bias. Furthermore, a TRUS based quantitative methodology is necessary to evaluate both the final system performance and clinical outcomes. Research is currently underway to remove these limitations, and to conduct a more detailed study using clinical indicators.

References

1. Nag et al: Intraoperative planning and evaluation of permanent prostate brachytherapy: report of the american brachytherapy society. *IJROBP* **51** (2001)
2. Tornes, A., Eriksen, M.: A new brachytherapy seed design for improved ultrasound visualization. In: *IEEE Symposium on Ultrasonics*. (2003) 1278–83
3. Prestidge et al: A survey of current clinical practice of permanent prostate brachytherapy in the united states. *IJROBP* **15;40(2)** (1998) 461–5
4. Hofstetter et al: Fluoroscopy as an imaging means for computer-assisted surgical navigation. *CAS* **4(2)** (1999) 65–76
5. Reed et al: Intraoperative fluoroscopic dose assessment in prostate brachytherapy patients. *Int J Radiat Oncol Biol Phys* **63** (2005) 301–7
6. Todor et al: Intraoperative dynamic dosimetry for prostate implants. *Phys Med Biol* **48(9)** (2003) 1153–71
7. French et al: Computing intraoperative dosimetry for prostate brachytherapy using trus and fluoroscopy. *Acad. Rad.* **12** (2005) 1262–72
8. Jain et al: C-arm calibration - is it really necessary ? In: *SPIE Medical Imaging; Visualization, Image-Guided Procedures, and Display*. (2007)
9. Jain et al: A robust fluoroscope tracking fiducial. *Med Phys* **32** (2005) 3185–98
10. Kon, R., Jain, A., Fichtinger, G.: Hidden seed reconstruction from c-arm images in brachytherapy. In: *IEEE ISBI*. (2006) 526–29
11. Su et al: Examination of dosimetry accuracy as a function of seed detection rate in permanent prostate brachytherapy. *Med Phy* **32** (2005) 3049–56

Detection of Intra-operative Edema in Prostate Brachytherapy

A. Jain^{1,3}, A. Deguet¹, I. Iordachita¹, G. Chintalapani¹, J. Blevins², Y. Le¹, E. Armour¹, C. Burdette², D. Song¹, G. Fichtinger¹

1 - Johns Hopkins University; 2 - Acoustic MedSystems Inc.; 3 - Philips Research North America

Abstract

Prostate Brachytherapy has emerged as a common treatment modality for early stage prostate cancer, wherein small seeds are implanted into the prostate to eradicate the cancer by emitting radiation. The main limitation in contemporary brachytherapy is faulty seed placement, predominantly due to the presence of intra-operative edema (tissue expansion). Intra-operative measurement of edema in prostate brachytherapy requires localization of inserted radioactive seeds relative to the prostate. Seeds were reconstructed using a typical non-isocentric C-arm, and exported to the commercial brachytherapy delivery system. Technical obstacles for 3D reconstruction on a non-isocentric C-arm included pose-dependent C-arm calibration; distortion correction; pose estimation of C-arm images; seed reconstruction; and C-arm to TRUS registration.

In precision-machined hard phantoms with 40-100 seeds and soft tissue phantoms with 45-87 seeds, we correctly reconstructed the seed implant shape with an average 3D precision of 0.35 mm and 0.24 mm, respectively. The reconstructed 3D seed positions were then registered to the pre-plan computed from TRUS. In a Phase-1 clinical trial on 6 patients with 49-82 planned seeds, we achieved intra-operative monitoring of seed distribution and dosimetry. We optimized the 100% prescribed iso-dose contour by inserting an average of 4.17 additional seeds, making intra-operative detection of edema (and subsequent dose optimization) possible on a typical non-isocentric C-arm, at negligible additional cost to the existing clinical installation. Furthermore, the proposed system is the first of its kind that can intra-operatively detect seed migration patterns. For many seeds, the results indicate a migration greater than 10 mm from their intended dropped locations.

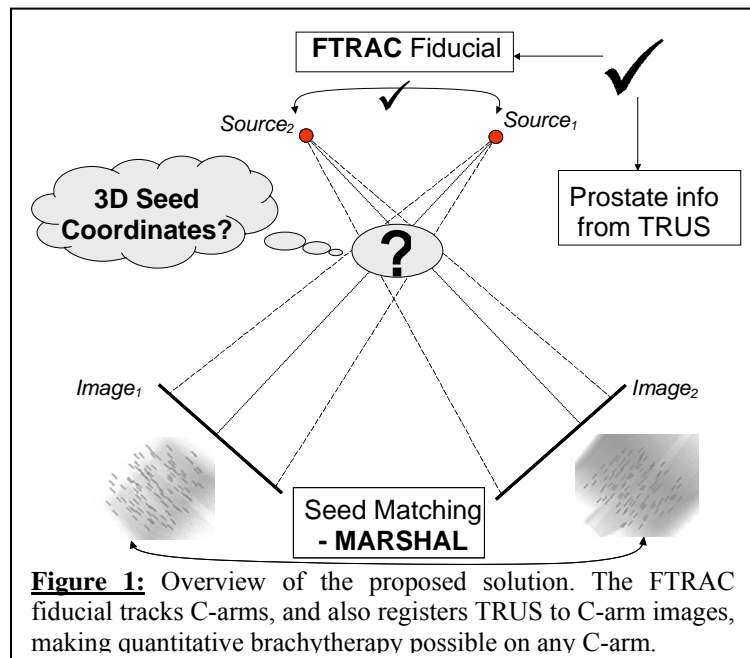
Keywords: Prostate Brachytherapy, Edema, Intra-operative Dosimetry.

Description of purpose: Prostate cancer continues to be a significant health problem, both nationally and worldwide. Permanent low dose rate brachytherapy has emerged as a definitive treatment modality of early stage low risk prostate cancer. The main limitation in contemporary brachytherapy is faulty seed placement, which may cause insufficient dose to the cancer cells and/or inadvertent radiation of the rectum, urethra, and bladder. One of the main reasons is edema, a natural response of the body, wherein the prostate tissue expands during the surgery owing to repeated needle-insertions and high radiation dose delivered to the tissue. It is one of the leading causes for under-dosed regions in the prostate, rendering any pre-operative planning imperfect. LDR prostate brachytherapy is almost exclusively performed with transrectal ultrasound (TRUS) guidance, while C-arm fluoroscopy is ubiquitously applied for gross visual assessment of the implant. C-arms are ubiquitous in contemporary LDR prostate brachytherapy, yet they cannot be used for real-time intra-operative dosimetric analysis due to a plethora of technical limitations. We developed a system that overcame these limitations toward providing quantitative dosimetry

analysis and implant optimization. In this paper we report novel method and system to reconstruct and spatially register the implanted seeds (that are visible in fluoroscopy) and soft tissue anatomy (that is visible in TRUS).

Method: We employ a regular clinical brachytherapy setup, without alteration, including a treatment planning workstation and stabilizer/stepper (Interplant®, CMS, St Louis), TRUS (B&K Medical), C-arm (GE OEC, Salt Lake City, UT). The C-arm is interfaced with a standalone laptop computer through an NTSC video line and frame grabber.

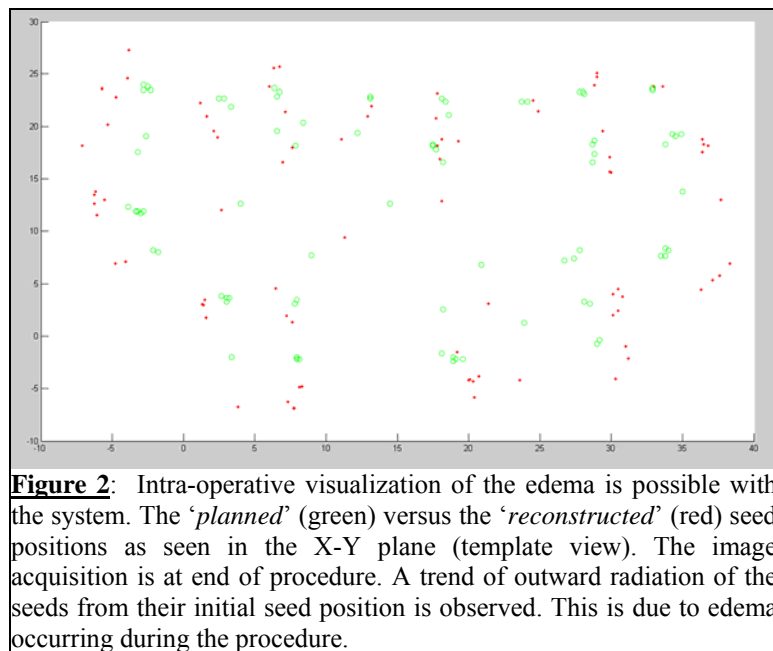
Workflow: The clinical workflow is identical to the standard procedure until the clinician decides to run a reconstruction and optimization, typically at each half of the procedure. A set of C-arm images are collected with as wide separation as possible (15°) and transferred to the laptop. After processing the fluoro images, the seeds are reconstructed in TRUS space and exported to the Interplant®. The physician uses standard Interplant® features to analyze the dose and modify the remainder of the implant plan, in order to optimize it. The procedure concludes when the exit dosimetry shows no cold spots.



Numerous technical obstacles had to be overcome in realizing the workflow above: (a) C-arm calibration; (b) image distortion correction; (c) pose estimation of C-arm images; (d) registration of C-arm to TRUS; (e) seed reconstruction, (f) dosimetry analysis, and finally (g) implant optimization.

Experiments and Results: We present results from 6 patients enrolled in a Phase-I clinical trial.

Implant reconstruction and dose analysis was performed halfway of



the implant and also in the end (an additional one was used for a research comparison to post-op CT). *In all the patients, the final dosimetry detected one or more cold spots (Figure 3).* In the fourth patient, 9 additional seeds (initial 67) were inserted to bring up V100 dose to the desired level. Apparently, the physician grew quickly to trust the system in catching cold spots, and instead became very cautious not to create hot spots. Importantly, all patients were released from the operating room with satisfactory V100/V90 dose and favorable DVH for all relevant structures. The use of the system added about 45 minutes to the OR time, with each set of three implant reconstructions taking about 15 minutes, including image capture, processing, 3D reconstruction, and dosimetry evaluation. We anticipate needing only a single reconstruction in the post-research phase. *Intra-operative visualization of edema was also possible with the system, which was found to be significant (Figure 2). The seeds showed a clear tendency of outward migration from their drop positions as the procedure progressed. Furthermore, post-operative edema can also be computed from a comparison of intra-op seed coordinates to their post-implant CT coordinates.*

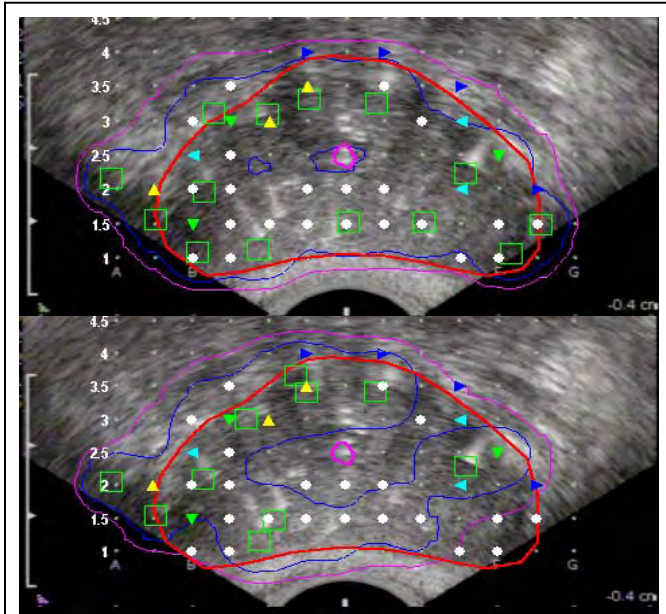


Figure 3: The system is able to detect *cold spots*. The V100 contours (blue) as assumed by the planning system (top) and as computed by the proposed system (bottom). In this patient, 3 cold spots were discovered in exit dosimetry. The prostate boundary is delineated by dark red contours and the green squares mark current seed coordinates. Note that the system also detected 4 seeds that have drifted out of slice, owing largely to the swelling effects of edema.

Conclusions: The system was exquisitely accurate in technical trials and has shown usefulness and great potential in a limited Phase-1 trial. It can quantitatively measure the amount of edema and the associated patterns observed in a patient.

New or breakthrough work to be presented: A first of a kind system that can use a non-isocentric C-arm to intra-operatively measure the pattern and extent of seed migration in prostate brachytherapy.

Indicate whether the work is being, or has been, submitted for publication or presentation elsewhere, and, if so, indicate how the submissions differ: Some preliminary results of the whole system have been accepted for publication at MICCAI 2007. This submission includes complete and detailed results with extensive analysis from all the patients enrolled in the Phase-I clinical trial.

Support: DoD/PC-050170, DoD/PC-050042, NIH-1R43CA099374, NSF-9731478.

Prostate Implant Reconstruction with Discrete Tomography

Xiaofeng Liu¹, Ameet K. Jain^{1,2} and Gabor Fichtinger¹

¹Department of Computer Science, Johns Hopkins University, Baltimore, MD, USA

²Philips Research North America, Briarcliff, NY, USA

Abstract. We developed a discrete tomography method for prostate implant reconstructions using only a limited number of X-ray projection images. A 3D voxel volume is reconstructed by back-projection and using distance maps generated from the projection images. The true seed locations are extracted from the voxel volume while false positive seeds are eliminated using a novel optimal geometry coverage model. The attractive feature of our method is that it does not require exact seed segmentation of the X-ray images and it yields near 100% correct reconstruction from only six images with an average reconstruction accuracy of 0.86 mm (std=0.46mm).

1. Introduction

Brachytherapy is a definitive treatment for low risk prostate cancer that represents the vast majority of new cases diagnosed nowadays. The brachytherapy procedure entails permanently implanting small radioactive seeds into the prostate. The main limitation of contemporary brachytherapy is faulty seed placement that may result in insufficient dose to the cancer and/or inadvertent radiation to the rectum, urethra, and bladder. Intra-operative implant optimization promises a major clinical breakthrough, but for this technique to succeed the implanted seeds must be reconstructed and registered with the anatomy [1]. This work concentrates on the first problem, reconstruction.

C-arm X-ray fluoroscopy is the gold standard in observing brachytherapy seeds and therefore is a natural candidate for implant localization. The 3D coordinates of the seeds can be calculated from multiple X-ray images upon solving the correspondence problem [2-6]. These methods uniformly require that seeds are accurately segmented in the X-ray images. Significant research has been dedicated to this problem, still without clinically robust and practical solution. To make the problem worse, typically 7%, but often as much as 43% of the seeds can be hidden in the X-ray images [7], and the recovery of these seeds is an exigent task that often leaves seeds undetected. Su *et al.* [7] proposed a solution to the hidden seed problem by resolving seed clusters and extending previously published approach [3], but it still required perfectly localizing all visible seeds all projection images.

Classic tomosynthesis might seem a suitable reconstruction, but unfortunately, it is impractical in brachytherapy because (1) the swing space of the C-arm is limited due to collision hazards and (2) the number of X-ray images is strictly limited in order to

save the patient and the OR crew from excessive toxic radiation. Tutar *et al.* [8] has proposed a variant of tomosynthesis denoted as selective back projection. However this method demands a large number of images (≥ 7) and wide C-arm angle ($\geq 25^\circ$) to succeed. It is also prone to introducing false positive (FP) seeds, which from a dosimetric point of view are more troublesome than hidden seeds, because they act toward underdosing the cancer. Tutar *et al.* use a heuristic rule to recognize FP seeds by their sizes, but since C-arm pose estimation and calibration errors affect the size of objects, this may result in faulty separation of the true and false seeds.

Our approach using discrete tomography is different in that after generating a 3D volume using back-projection we detect and remove the false positive seeds by solving an optimal coverage problem. We achieved high reconstruction rate with fewer images.

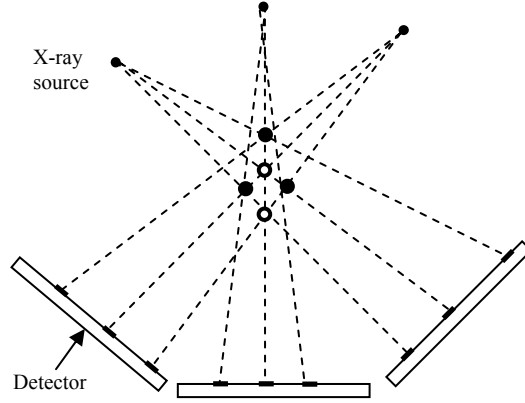


Fig. 1. Two false positive seeds are introduced by three legitimate seeds when their projectiles intersect the same voxels.

2. Method

In the example in Figure 1, three X-ray images are used. Three seeds project in each image and leave a “mark” in the image, typically a dark blotch in fluoroscopy. After reconstructing a 3D voxel volume with common back-projection, five candidate seeds are found in the volume and all appear to be legitimate seeds in each image. The question is how to separate the true seeds from the false positives. In this simplistic example, it is very easy to identify the legitimate seeds (solid circles) because any other choice will lead to an inconsistency: there will be “seed marks” in one or more X-ray images to which no seed in the volume projects. Therefore, the intuition behind the reasoning is that each “seed mark” in each image must be “covered” by at least one seed in the voxel volume. To support this intuition, we develop a theoretical framework based on optimal geometry coverage.

Tomosynthesis with Distance Map and Seed Localization. Tomosynthesis [10] is the technique to reconstruct a 3D volume from multiple 2D projection images within a limited angle. The most commonly used approach is the back projection method, which was first introduced for CT reconstruction. In this method, each voxel in a 3D volume is projected onto all the images. The value assigned to this voxel is calculated as the average of the intensity values of its projected locations in the images.

A local coordinate system must be defined for the C-arm. For any arbitrary 3D point in the space, after C-arm calibration, its projected coordinates on the 2D image plane can be calculated by the rules of perspective projection.

In practice, the C-arm’s pose is estimated with some error. Since the size of the seeds is small relative to the focal length, the reconstruction is quite sensitive to pose

error. To make the reconstruction more robust to pose error, in the reconstruction of the 3D voxel volume we use distance maps rather than the projection image itself.

As preprocessing, in each image we first extract the so called 2D seed regions--areas that contain seeds' projections--using adaptive thresholding and morphological operators and call the resulting images "seed-only" image. Then for each seed-only image, a distance map is calculated using a distance transform: the value at each pixel is the Euclidean distance to its nearest 2D seed region. (Pixels inside a 2D seed region all take a value of zero.) In reconstructing the 3D volume, the value of a voxel is the average of the distance values at all of its projected locations.

After the 3D voxel volume is reconstructed, candidate 3D seed regions are extracted by thresholding. The threshold value is based on estimated pose error. For example, in case of small pose error of less than 1 degree rotation, such as in Jain *et al.* [6], the threshold is set to $\frac{1}{2}$ pixel. Upon thresholding, connected 3D seed regions are considered as candidate seeds. The candidate seeds are then labeled using the standard 3D "connected component labeling" method, i.e. any two neighboring voxels in the 3D seed regions are assigned the same label and considered as parts of the same seed. After that, the centroids of all the candidate seeds are calculated by averaging the 3D coordinates of all voxels wearing the same label. Each candidate seed is then represented by the location of its centroid, in addition to its label.

As we mentioned earlier, a decisive advantage of tomosynthesis over the three-film technique and its derivatives [6] is that, in addition to not requiring precise seed segmentation, it can reconstruct all hidden seeds. But the disadvantage is that tomosynthesis introduces false positive seeds, often as much as 20%. Next, we propose a theoretical framework for separating the true seeds from the false ones.

Theoretical Framework for Separating True Seeds. The problem is formulated as an optimal geometric coverage problem [11]. The general optimal coverage problem arises, for example, in wireless network design. From a given set of "server" points, we must select the minimum subset that can cover a given set of "client" points. The goal is formulated as to minimize a total cost function, which is the sum of the cost functions defined on all the selected server points.

In our problem, based on the intuition mentioned earlier, we want to find the M true seeds from the set of N candidates, such that all the 2D seed regions are "covered" in all projection images, i.e. every 2D seed region must have at least one true seed projected in it. In constructing the appropriate cost function, we can use the observation that a false positive (FP) seed, owing to its very nature, is projected close to some true seed in every image. While a true seed may be projected close to some other true seeds in some images, it usually is not the case for every image. (While it is common that a true seed can be hidden in some projection images, we have never encountered a situation where a true seed was hidden in all images. We also note that no existing method can recover such a seed.)

Hence for the server model, we define the cost function of a given seed (potential server point) as the sum of the closest distances between the projections of this seed and the projections of all other true seeds, in all images. We formulate the problem as such a general optimal coverage problem: Given the N candidate seeds, we want to find M seeds (x_1, x_2, \dots, x_M) from them such that all 2D seed regions in the seed-only images are covered, and the below cost function is minimized

$$C = - \sum_{m=1}^M \sum_{i=1}^n \hat{d}_i(x_m) \quad (2)$$

$$\text{where } \hat{d}_i(x_n) = \min_m \|P^j x_m - P^j x_n\|, \quad \forall n \in [1, 2, \dots, M], \text{ and } n \neq m \quad (3)$$

and P^j is the projection operator that projects a 3D point onto the j^{th} image.

Unfortunately, the optimal coverage problem is NP-hard [12] and its computational complexity is $O(C_M^N)$, where C_M^N means N choose M . Thus for a large set of seeds, it is not possible to find its global optimal solution. We, however, managed to reduce the size of the problem by using the 2D seed-only images for regularization. To further reduce the problem, we also used greedy search to minimize local costs rather than the global cost function in Eq. (2).

Seed Clustering. To ensure that the projections of selected true seeds cover all the 2D seed regions in all seed-only images, the candidate seeds are clustered based on their projections in each image. For this purpose, we label all 2D seed regions in all seed-only images, in the similar way as 3D labeling described, e.g. the separated seed regions are assigned different labels and pixels in the same connected region wear the same label. The projections of seeds can then be clustered based on these labels. An example is shown in Fig. 2. Unlike Su *et al.* [7], the purpose of seed clustering is not to segment the 2D seed projections from 2D seed clusters in the images, or to identify the number of true seeds in each cluster. Instead, we use the seed clustering as a way to relating the 3D seeds, and the relationship is used in the coverage function that is to be minimized.



Fig. 2. (Left) X-ray image on phantom data; (Middle) the seed-only image resulted after preprocessing; (Right) Example of seed region labeling and seed grouping.

On a projection image, the projections of all candidate seeds are first computed using Eq. (1). We denote a 3D candidate seed as x_n , and its 2D projection on the j^{th} image is $P^j x_n$. For each $P^j x_n$, we find its nearest seed region, which is labeled as $L^j(P^j x_n)$. The distance from $P^j x_n$ to its closest seed region is also calculated and denoted as d_n^j ($d_n^j = 0$ if $P^j x_n$ is inside a seed region). The seed projections are then clustered based on $L^j(P^j x_n)$. Let there be K^j seed regions on the j^{th} seed-only image, and they are labeled as $1, 2, \dots, K^j$. The projections of the N candidate seeds on the j^{th} image are then clustered into K^j sets Ω_k^j , such that

$$\forall p_1, p_2 \in \Omega_k^j, L^j(p_1) = L^j(p_2), \quad j = 1, 2, \dots, N_p, \quad k = 1, 2, \dots, K^j \quad (4)$$

Let $|\Omega_k^j|$ be the cardinal of set Ω_k^j , we say the seed region with label k in j^{th} image is

covered by $\|\Omega_k^j\|$ seeds. $\|\Omega_k^j\| \geq 1$. The clustering is repeated on all images.

In the example in Fig. 2(c), the seed regions are labeled from 1 to 5 and red asterisks mark the 2D projections of the candidate seeds. The three regions labeled with 1, 4 and 5 contain one true seed each. The two regions labeled with 2 and 3 contain two (or more) true seeds each. Since the seeds in region 2 (and 3) are connected, it is considered as a single seed region. The candidate seeds include both true seeds and a few false seeds. In this example, upon clustering, the sets with label from 1 to 5 have 2, 3, 4, 1, and 1 element(s) individually

Local Coverage and Greedy Search. The seed clustering according to each projection can help reduce the size of our optimization problem. If a seed region is covered only by one seed, this seed must be a true one, because otherwise this region is not covered. The set of such seeds can be expressed as:

$$\mathbf{G} = \bigcup_j \{x_n : L^j(P^j x_n) = k \text{ and } \|\Omega_k^j\| = 1, k = 1, 2, \dots, K^j\}, j = 1, 2, \dots, N_p \quad (5)$$

where N_p is the number of projection images. These seeds are always chosen as true seeds. Hence the optimization problem is reduced to choose $(M - \|\mathbf{G}\|)$ true seeds from $(N - \|\mathbf{G}\|)$ candidate seeds. This can also be seen in the example in Fig. 2(c). The two regions labeled with 4 and 5 contain only one seed each. Therefore these two seeds are considered as true seeds and are always chosen.

Besides, instead of finding the global optimization of the cost function in (2), we use greedy search to find an approximate optimal solution. We also redefine the local coverage cost function as

$$C = \sum_n c(x_n), \quad c(x_n) = -\sum_{j=1}^{N_p} \frac{1 + D^j(x_n)}{1 + d_n^j}, \text{ for all } x_n \notin \mathbf{G} \quad (6)$$

where

$$D^j(x_n) = \min_{m \neq n} \|P^j x_n - P^j x_m\|, \quad \forall x_m \in \mathbf{S} - \mathbf{G}, \text{ and } L^j(P^j x_n) = L^j(P^j x_m) \quad (7)$$

is the minimum distance between the projection of x_n and the projections of other seeds in the cluster in the j^{th} image that includes x_n , and d_n^j is the distance from $P^j x_n$ to the nearest seed region. d_n^j is added in the cost function to include the effect of imperfect X-ray pose estimation.

The minimization problem in (6) is solved using greedy search iteratively. During each cycle of iteration, the seed that has the largest cost value $c(x_n)$ is considered as a false seed and is removed from the candidate seed set. \mathbf{G} is updated at the beginning of each cycle of iteration, for after the removal of one seed, there may be additional seeds that cover some region alone (i.e. no other seed covers this region.) These seeds need to be extracted and added to \mathbf{G} . The algorithm is summarized as below.

Algorithm 1: find M good seeds from N candidate seeds using greedy search

1. Initialize \mathbf{S} be the set of candidate seeds.
2. For $i = 1:N-M$
3. Calculate \mathbf{G} using (5).
4. Calculate local cost function $c(x)$ of all seeds x in $\mathbf{S} - \mathbf{G}$ using (6).
5. Find $x_k \in \mathbf{S} - \mathbf{G}$, such that $x_k = \arg_x \min c(x)$.
6. Remove x_k from \mathbf{S} : $\mathbf{S} = \mathbf{S} - \{x_k\}$.

3. Experiments and Results

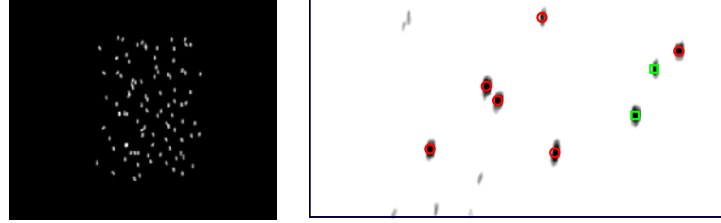


Fig. 3. (Left) Part of a synthetic C-arm image; (Right) One slice of the reconstructed 3D volume. The red circles mark the true seeds, and the green squares represent the FP seeds.

Simulations. Synthetic C-arm images were used to verify our method. The images simulated a 50 cc prostate with a seed density of 2.0 seed/cc. The C-arm's focal length was 1000 mm, and the pixel size was 0.25 mm. Six images were generated on a 20° cone around the AP axis with evenly distributed angles. The seeds were represented by cylinders with a radius of 0.4 mm and a length of 1.45 mm. A typical synthetic image is shown in Fig. 3(a). No pose estimation error was assumed.

Table 1. Seed reconstruction results using different number of synthetic images

Number of images used	Number of true seeds implanted	Number of candidate seeds before FP removal	Correctly reconstructed seeds after FP removal (%)	Mean reconstruction error (mm)	Reconstruction error STD (mm)
3	96	105.6	99.4	0.19	0.19
4	96	97.7	100	0.12	0.09

We reconstructed the seeds using 3, 4 and 6 images. For 3 images, 20 experiments were performed by using all the 20 combinations of selecting 3 images from the 6 available images. For 4 images, four experiments were performed using different image combinations. The results are shown in Table 1. In each experiment, the number of implanted seeds was assumed known. After FP removal, a set of candidate seeds that equal to the number of implanted seeds were chose. These chosen seeds were then compared with the known 3D locations of implanted seeds. When using 3 images, there were about 10% FP seeds reconstructed initially and then almost all were successfully removed, indicated by the near 100% correct final reconstruction rate. This means that when there is no pose estimation error, the seeds can be reconstructed accurately even from as few as 3 images using our method.

Phantom Studies. Experiments were performed on a seed phantom constructed from acetol. The FTRAC fiducial was used to track the C-arm (with accuracy of 0.56 mm translation and 0.33° rotation). It was attached to the seed phantom, as shown in Fig. 4. The seed phantom is comprised of twelve slabs with 5mm thickness each. Each slab has more than 100 holes with 5 mm spacing, into which the seed can be inserted. By precise manufacturing, the seed phantom was attached in a known position to a radiographic C-arm tracking fiducial, replicated after Jain *et al.* [13]. In this way, the exact location of each implanted seed was known relative to the tracking fiducial, serving as ground truth. Because some rotation error got introduced during

assembly, the ground absolute seed positions had about 0.5 mm error. (Note that their relative positions were precisely known.) The seed density was about 1.56 seed/cc. Five data sets were collected with the number of seeds varying from 40 to. For each data set, six images within a 20° cone around the AP axis were taken using a *Phillips integris V3000* fluoroscope and dewarped using the pin-cushion test. We used four, five and six images to reconstruct the seeds, by using all the combinations of the six available images, i.e. 15 experiments using four images, 6 using five images, and 1 using six images for each data set. The reconstructed seeds were compared with the computed ground truth, and the results were shown in Table 2.

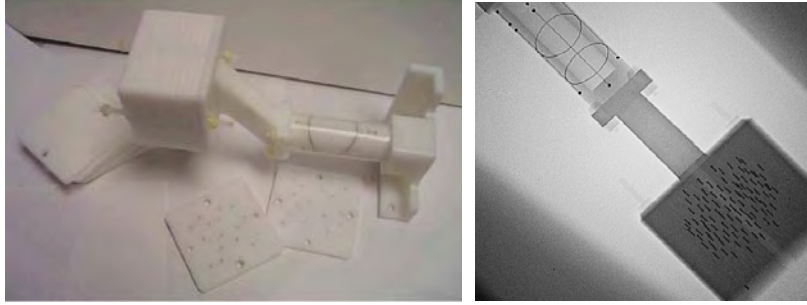


Fig. 4 (Left) An image of the seed phantom attached to the FTRAC fiducial. (Right) A typical X-ray image of the combination (with 100 seeds inserted)

Table 2. Seed reconstruction results on phantom data using different number of images

Number of images used	Number of seeds implanted	Number of candidate seeds before FP removal	Correctly reconstructed seeds after FP removal (%)	Mean reconstruction error (mm)	Reconstruction error STD (mm)
6	40	46	100	1.04	0.56
	55	58	100	0.67	0.39
	70	82	98.6	0.72	0.42
	85	94	100	0.97	0.44
	100	112	98	0.94	0.52
5	40	46.3	99.5	1.02	0.53
	55	68.3	98.8	0.85	0.46
	70	92.3	97.8	0.85	0.46
	85	105.3	97.0	1.00	0.57
	100	121.3	92.5	1.19	0.81
4	40	53.7	96.8	1.24	0.76
	55	82.1	94.7	0.99	0.69
	70	112	94.3	0.91	0.77
	85	135.8	90.1	1.13	0.62
	100	159.7	86.3	1.44	0.91

It was shown in [12] that in prostate brachytherapy, 95% of the implanted seeds must be recovered in order to obtain clinically accurate estimation of the dose. Our results showed that (1) from six images more than 98% seeds can be successfully reconstructed, and (2) six images were sufficient for deriving clinically accurate dose estimation. Furthermore, the number of required images depends on the number of

seeds implanted. For a smaller number of seeds (40, 55, 70), only four to five images were required. Additionally the performance of our method depends on the ratio between the number of FP seeds and the implanted seeds, which in turn depends on both the number of images used and the number of implanted seeds. Generally the lower is this ratio, the higher is the seed reconstruction ratio we may achieve.

In summary, we presented a novel method for prostate brachytherapy seed reconstruction using C-arm images. We generate distance maps from the 2D projection images, then a 3D volume is then reconstructed using tomosynthesis using the distance maps, and finally true seeds are extracted from the voxel volume. The attractive feature of our method is that it does not require exact seed segmentation of the X-ray images. As a tradeoff, our method requires slightly higher number of images than the methods that requires elaborate explicit segmentation. Our method yields near 100% correct reconstruction from only six images with an average reconstruction accuracy of 0.86 mm (std=0.46mm). The method was robust to pose error present in radiographic C-arm tracking.

Acknowledgements. This work was funded by NSF grant EEC-9741748, NIH grant 2R44CA099374, and DoD grant PC050170.

References

- [1] M.J. Zelefsky, *et al.*, “Five-year outcome of intraoperative conformal permanent I-125 interstitial implantation for patients with clinically localized prostate cancer,” *Int. J. Radiat. Oncol. Biol. Phys.*, 67(1):65-70, 2007
- [2] D. Tubic, *et al.*, “Automated seed detection and three-dimensional reconstruction II, reconstruction of permanent prostate implants using simulated annealing,” *Med. Phys.*, 28(11):2272-9, 2001
- [3] S. Narayanan, P. Cho, and R. Marks, “Fast cross-projection algorithm for reconstruction of seeds in prostate brachytherapy,” *Med. Phys.*, 29(7): 1572-9, 2002
- [4] D. Todor, *et al.*, “Operator-free, film-based 3D seed reconstruction in brachytherapy,” *Phys. Med. Biol.*, 47(12):2031-48, Jun 2002
- [5] S. T. Lam, *et al.*, “Three-dimensional seed reconstruction for prostate brachytherapy using Hough trajectories,” *Phys. Med. Biol.*, 49(4): 557-69, 2004
- [6] A. Jain, *et al.*, “Matching and reconstruction of brachytherapy seeds using the Hungarian algorithm (MARSHAL),” *Med. Phys.*, 32(11):3475-92, 2005
- [7] Y. Su, *et al.*, “Prostate brachytherapy seed localization by analysis of multiple projections: identifying and addressing the seed overlap problem,” *Med. Phys.*, 31(5):1277-87, 2004
- [8] I. B. Tutar, *et al.*, “Tomosynthesis-based localization of radioactive seeds in prostate brachytherapy,” *Med. Phys.*, 30(12):3135-3142, 2003
- [9] D. G. Grant, “Tomosynthesis: A three-dimensional radiographic imaging technique,” *IEEE Trans. Biomed. Eng.*, 19:20-28, 1972
- [10] G. T. Herman, and A. Kuba, “Discrete tomography in medical imaging,” *Proceeding of the IEEE*, 91(10):1612-1626, 2003
- [11] M. Marengoni, B. Draper, A. Hanson, and R. Sitaraman, “A system to place observers on a polyhedral terrain in polynomial time,” *Image and Vision Computing*, 18(10):773-80, 2000
- [12] Y. Su, *et al.*, “Examination of dosimetry accuracy as a function of seed detection rate in permanent prostate brachytherapy,” *Med. Phys.*, 32(9):3049-3056, 2005
- [13] A. Jain, *et al.*, “Robust Fluoroscope Tracking Fiducial,” *Med. Phys.*, 32(10):3185-98, 2005

Toward optimal matching for 3D reconstruction of brachytherapy seeds [★]

Christian Labat¹, Ameet Jain^{1,3}, Gabor Fichtinger¹ and Jerry Prince²

¹ Department of Computer Science,

² Department of Electrical and Computer Engineering,
Johns Hopkins University, Baltimore, MD 21218, USA.

³ Philips Research North America, Briarcliff, NY.

Abstract. X-ray C-arm fluoroscopy is a natural choice for intra-operative seed localization in prostate brachytherapy. Resolving the correspondence of seeds in the projection images can be modeled as an assignment problem that is NP-hard. Our approach rests on the practical observation that the optimal solution has almost zero cost if the pose of the C-arm is known accurately. This allowed us to derive an equivalent problem of reduced dimensionality that, with linear programming, can be solved efficiently in polynomial time. Additionally, our method demonstrates significantly increased robustness to C-arm pose errors when compared to the prior art. Because under actual clinical circumstances it is exceedingly difficult to track the C-arm, easing on this constraint has additional practical utility.

1 Introduction

Intraoperative dosimetric quality assurance in prostate brachytherapy critically depends on discerning the three-dimensional (3D) locations of implanted seeds. The ability to reconstruct the implanted seeds intraoperatively will allow us to make immediate provisions for dosimetric deviations from the optimal implant plan. A method for seed reconstruction from pre-segmented C-arm fluoroscopy images has been proposed, among other works, by Jain et al. in [1], where the 3D coordinates of the implanted seeds are calculated upon resolving the matching of seeds in multiple X-ray images.

At least three images are necessary to eliminate ambiguities. The resulting optimization problem is NP-hard. Heuristic approaches, such as of Jain et al. [1], have been proposed to approximately solve the optimization problem. However, the use of a heuristics leads to *algorithmic error*, in addition to physical errors like the inaccuracy in knowing the relative poses of the C-arm shots (pose error). To tackle this issue, we propose to consider all the images simultaneously, instead of suboptimal subsets of two images such as proposed in [1].

The optimization problem has a salient feature: since the images represent a real situation (i.e. an existing object, the set of seeds, is being imaged), the

[★] This work has been supported by DoD PC050042, DoD PC050170 and NIH 2R44CA099374.

optimal solution has a near-zero cost when the pose error is low, and is actually zero without pose error. We propose to utilize this feature of the problem to reduce its number of variables, thereby allowing to obtain the optimal solution at a reasonable computational cost. This exact *dimensionality reduction* is only possible when the pose error is sufficiently low. We claim that this is not restrictive in our framework since a high pose error leads to high error in the estimation of the 3D coordinates of the implanted seeds, which is not acceptable. Actually, the idea of dimensionality reduction is not new. For instance, in [1, p. 3480] the original tripartite matching is projected into inspired bipartite matchings, while introducing inaccuracy. In contrast, the proposed method performs dimensionality reduction while ensuring equivalency to the original problem.

The MARSHAL method of Jain et al. has demonstrated solid performance [1] and we chose this work as the benchmark and basis of comparison for our work. A comparison between MARSHAL and our method was conducted to evaluate the sensitivity to pose errors on simulated and phantom data. The proposed method shows significant increase in robustness to pose errors.

2 Method

Consider a collection of X-ray images of a constellation of implanted seeds. We assume that the 2D seed locations can be identified on each of the X-ray images, and we consider the problem of identifying corresponding seeds in all the images. Given these matched seed locations, a reconstruction of the seed locations in 3D can be achieved provided there are no ambiguities. It is more likely that such ambiguities are avoided when there are more X-ray images, but this in turn increases the complexity of the problem. Here we do not consider CT or limited angle tomosynthesis, as our work focuses on reconstruction from a very limited number of images. We propose a solution for three images, which is often sufficient in practice, and which is extendable to more images.

2.1 3D Reconstruction as a matching problem

The 3D locations of the implanted seeds, modeled as points, can be reconstructed through 3D triangulation from the X-ray images upon resolving the correspondence of seeds, which is the focus of this paper. Let n be the number of points in the clinical work volume. Let s_{lm} be the position of l^{th} point in m^{th} image. When three images are used, the matching problem can be formulated as an axial 3D assignment problem (3DAP) [1]:

$$\min_{x_{ijk}} \sum_{i=1}^n \sum_{j=1}^n \sum_{k=1}^n c_{ijk} x_{ijk}, \quad \text{where} \quad (1)$$

$$\begin{cases} x_{ijk} \in \{0, 1\} \\ \sum_{i=1}^n \sum_{j=1}^n x_{ijk} = 1, & \forall k \\ \sum_{i=1}^n \sum_{k=1}^n x_{ijk} = 1, & \forall j \\ \sum_{j=1}^n \sum_{k=1}^n x_{ijk} = 1, & \forall i \end{cases} \quad (2)$$

c_{ijk} is the cost of matching point s_{i1} to points s_{j2} and s_{k3} . x_{ijk} is a binary variable deciding the correctness of the match $\langle i, j, k \rangle$. (2) force every segmented point to be chosen once. Thus, x represents any feasible global match, with the cost of that correspondence given by $\sum \sum \sum c_{ijk} x_{ijk}$. One good choice for a cost-metric c is projection error (PE) [1]. For any given set of poses and correspondence, the intersection of the three lines that join each projection to its respective X-ray source can be computed using a closed form solution that minimizes the L_2 norm of the error. PE can be computed by projecting this 3D point in each image and then measuring the distance between the projected location and the observed location of the point.

A feasible solution x of the above problem is a 3D permutation array. This problem has $(n!)^2$ feasible solutions. Branch and bound is a classical algorithm for optimally solving the 3DAP. This can be generally achieve only for n small because of the combinatorial explosion. Thus, it has been proposed heuristics that approximately solve the 3DAP, such as MARSHAL in [1]. MARSHAL sub-optimally projects the original 3DAP into three distinct 2DAP that can be solved in polynomial time by using the Hungarian algorithm.

We point out that the 3DAP has a salient feature that we can exploit. Since the images represent a real situation, the optimal solution has a near-zero cost when the pose error is low and the optimal cost is actually zero without no pose error. In the next section, we use this feature to reduce the number of variables in the problem, thus permitting us to get the optimal solution at a reasonable computational cost. This new method tackles the complete optimization problem without using suboptimal projections, such as in MARSHAL.

2.2 Dimensionality reduction

Let $N = n^3$. We rewrite the variables x_{ijk} and the costs c_{ijk} in a vectorial form such that $\mathbf{x}, \mathbf{c} \in \mathbb{R}^N$. In the sequel we also make use of the notation u_ℓ to denote u_{ijk} . The 3DAP (1)-(2) reads as the following integer linear program

$$P : \min_{\mathbf{x} \in \mathcal{C}} \mathbf{c}^t \mathbf{x}, \quad (3)$$

with the constraint set $\mathcal{C} = \{\mathbf{x} : \mathbf{M}\mathbf{x} = [1, \dots, 1]^t, x_\ell \in \{0, 1\}\}$, where $\mathbf{M}\mathbf{x} = [1, \dots, 1]^t$ is a matrix form of (2).

Principle: Since the coefficients of x are either 0 or 1 and there must be n 1's, an optimal solution of P can be thought of as the selection of n cost coefficients such that the resulting cost is minimum while constraints \mathcal{C} are satisfied. Given a feasible solution, Lemma 1 (below) states that all cost coefficients that are greater than the cost associated with this solution cannot be selected in the optimal solution. Since those coefficients can never be selected, the dimension of the problem can be reduced by removing those coefficients from further consideration. This yields an equivalent problem of reduced dimensionality. If the reduction in dimensionality is sufficiently large, then the new problem can be

solved exactly in reasonable time even though the original problem is far too costly to solve.

Lemma 1. *Let us assume that the cost coefficients c_ℓ are positive. Let $\mathbf{x}_0 \in \mathcal{C}$ be a feasible solution. The integer linear problem P defined by (3) is equivalent to the following integer linear problem (ie., they share the same optimal solutions)*

$$P' : \min_{\mathbf{x} \in \mathcal{C}} (\mathbf{c}')^t \mathbf{x}, \quad \text{where} \quad c'_\ell = \begin{cases} c_\ell, & \text{if } c_\ell \leq m_P(\mathbf{x}_0) \\ \infty, & \text{if } c_\ell > m_P(\mathbf{x}_0) \end{cases} \quad (4)$$

and where $m_P(\mathbf{x}) = \mathbf{c}^t \mathbf{x}$ is the cost of problem P at the feasible solution \mathbf{x} .

Proof. Let $\mathbf{x}^* \in \mathcal{C}$ be an optimal solution to problem P . We have for all $\mathbf{x}_0 \in \mathcal{C}$

$$m_P(\mathbf{x}^*) \leq m_P(\mathbf{x}_0). \quad (5)$$

Let us consider $c_\ell > m_P(\mathbf{x}_0)$. From (5) we have $c_\ell > m_P(\mathbf{x}^*)$. Since c_ℓ are positive and x_ℓ^* are binary, we have necessarily $x_\ell^* = 0$. \square

The dimensionality reduction can be illustrated as follows:

$$P : \begin{bmatrix} c_1 \\ c_2 \\ \vdots \\ c_N \end{bmatrix} \longrightarrow P' : \begin{bmatrix} c'_1 \\ c'_2 \\ \vdots \\ c'_N \end{bmatrix} = \begin{bmatrix} c_{i1} \\ \infty \\ c_{i2} \\ \vdots \\ c_{iK} \end{bmatrix} \longrightarrow \tilde{P} : \begin{bmatrix} \tilde{c}_1 \\ \tilde{c}_2 \\ \vdots \\ \tilde{c}_K \end{bmatrix} = \begin{bmatrix} c_{i1} \\ c_{i2} \\ \vdots \\ c_{iK} \end{bmatrix}$$

The original problem P is equivalent to the reduced problem

$$\tilde{P} : \min_{\tilde{\mathbf{x}} \in \tilde{\mathcal{C}}} \tilde{\mathbf{c}}^t \tilde{\mathbf{x}},$$

where $\tilde{\mathbf{x}}, \tilde{\mathbf{c}} \in \mathbb{R}^K$ ($K \leq N$) and with the constraint set $\tilde{\mathcal{C}} = \{\tilde{\mathbf{x}} : \tilde{\mathbf{M}}\tilde{\mathbf{x}} = [1, \dots, 1]^t, \tilde{x}_\ell \in \{0, 1\}\}$ with $\tilde{\mathbf{M}} = \mathbf{M}\mathbf{R}$ and where \mathbf{R} is the *dimensionality reduction matrix* of size $N \times K$ such that $[x_{i1} \ 0 \ x_{i2} \ 0 \ \dots \ x_{iK}]^t = \mathbf{R} [\tilde{x}_1 \ \tilde{x}_2 \ \dots \ \tilde{x}_K]^t$. Once the reduced problem \tilde{P} is solved, the optimal solution to the original problem P is simply given by $\mathbf{x}^* = \mathbf{R}\tilde{\mathbf{x}}^*$.

Note that a dimensionality reduction ($K < N$) is not guaranteed for the general 3DAP, even in the most favorable case $m_P(\mathbf{x}_0) = m_P(\mathbf{x}^*)$. However, a dimensionality reduction occurs in the case of our problem since the range of the cost coefficients is wide and the optimal solution has a near-zero cost when the pose error is low. The practical interest clearly depends on the dimensionality reduction ratio (K/N). We show next that this ratio actually can be improved.

Improving dimensionality reduction: Lemma 1 uses only the integer constraint in \mathcal{C} to reach dimensionality reduction. But using the fact that the feasible set \mathcal{C} comprises permutation matrices, it is possible to reduce the dimensionality of this problem even further. To demonstrate this, we start with the following Lemma.

Lemma 2. *The integer linear problem P defined by (3) is equivalent to the following integer linear problem*

$$P'' : \min_{\mathbf{x} \in \mathcal{C}} (\mathbf{c}'')^t \mathbf{x}$$

where the minimum cost in each row is subtracted from the entire row

$$c''_{ijk} = c_{ijk} - \min_{j,k} c_{ijk}. \quad (6)$$

Proof. For lack of space, the proof is not detailed.

To show that this Lemma permits further dimensionality reduction, let us apply Lemma 1 on the new problem P'' . From (4), the cost coefficient c''_ℓ is equivalent to ∞ if $c''_\ell > m_{P''}(\mathbf{x})$. According to (6) the former condition is equivalent to

$$c_{ijk} > m_P(\mathbf{x}) - \left(\sum_{i=1}^n \min_{j,k} c_{ijk} - \min_{j,k} c_{ijk} \right)$$

The latter condition is less restrictive than $c_\ell > m_P(\mathbf{x})$ since the cost coefficients are positive. As a result, the dimensionality reduction is higher within the new problem P'' than within the original problem P . It is then preferable to consider problem P'' instead of problem P since Lemma 2 ensures that they are equivalent. It is actually possible to reduce dimensionality even further. The operation (6) can also be performed successively for the columns and depths to decrease the cost coefficients, while still ensuring equivalency to the original problem.

2.3 Optimization strategy

Integer Programming / Linear Programming: The Integer Program (1)-(2) can be directly solved with standard techniques such as branch and bound. IP problems are NP hard, however, and may take an exponential amount of computational time. It has been shown that the linear program corresponding to the 2D assignment problem (2DAP) has an integer solution even without integer constraints [2]. As well, this linear program can be solved efficiently in polynomial time using interior point methods for instance [3]. To our knowledge, however, there is no analogous result for the 3DAP. Nevertheless, we have gone ahead and implemented the linear program for the 3DAP problem followed by a test to see if its solution is binary (up to numerical errors). In all of our experiments, we have never obtained a nonbinary solution to this problem, which points to the potential validity of the 2D theoretical result in 3D as well. (We are currently investigating this theoretical issue.)

Dimensionality reduction thresholding: From Lemma 1, the degree of dimensionality reduction depends on the cost $m_P(\mathbf{x}_0)$ of a feasible solution \mathbf{x}_0 . It is possible to use a suboptimal algorithm, such as MARSHAL, to find a feasible solution \mathbf{x}_0 . Unfortunately, when there is high pose error, MARSHAL often provides such a suboptimal solution that very little dimensionality reduction can be

be achieved. Therefore, we propose instead to choose a threshold parameter η , which is essentially a “guess” as to what the cost of a feasible solution might be. This permits us to reduce the dimensionality of the problem and run the linear problem on the resultant problem. If the solution of this problem is integer and it has a cost lower than η , then it must be optimal. If the resultant cost is larger than η then the solution might be optimal, but we cannot guarantee it. It is then our option whether to accept a (potentially) suboptimal solution or to increase η and rerun the linear problem until we have a guaranteed optimal solution.

In our experiments, we determine η in the following way. Rank order all costs from lowest to highest and pick an integer K . Let η be the value of the K^{th} smallest cost coefficient. The influence of K on the rate of feasibility and optimality of the proposed method is experimentally studied in the next section.

3 Simulation and Phantom Experiments

We present a comparison between the MARSHAL algorithm and the proposed method using simulation and phantom data. We got a copy of the MARSHAL code from the authors for comparison [1]. Both algorithms were implemented in Matlab 7.1 on a Linux PC (Intel EM64T 3.6 GHz, 24GB RAM).

3.1 Evaluation of pose errors sensitivity

Two separate comparisons were performed. One compared the two algorithms to translational errors and the other to rotational errors. These are both common errors in C-arm position calibration in the operating room. Random error was modeled using a uniform probability density function. When we report results for an h error this means that each of the three components of error (in either translation or rotation) were generated as independent random variables uniformly distributed on $[-h, h]$. Following [1], a statistical bias in translation was incorporated in the generation of the datasets to account for the expected differences in directional errors in fluoroscope tracking using a fiducial. In particular, we assumed that the in-plane error is a factor of five times smaller than the through-plane error h . No analogous bias was used in the rotation errors.

Realistic simulations of prostate brachytherapy seeds implants were generated with seeds density of 2 and 2.5 seeds/cc and prostate size of 35 and 45 cc. The number of seeds in the implants were $n = \{72, 84, 96, 112\}$. A cone angle of 10° was used for the acquisition of the three simulated X-ray images. Averaged results from a total of 2,000 datasets are shown in Fig. 1.

The proposed method, with $100n$ cost coefficients remaining after dimensionality reduction, performs significantly better than MARSHAL, as shown in Fig. 1(a)-(d). It still matches correctly 89% of the seeds when rotation error reaches 4° , while MARSHAL drops to 59%. The proposed method still matches correctly 99% of the seeds when the translation error reaches 10 mm, while MARSHAL drops to 72%. The computational time of the proposed method is higher than that of MARSHAL as shown in Fig. 1(e)-(f). We point out that most of the computational time of the proposed method (solid line) is actually

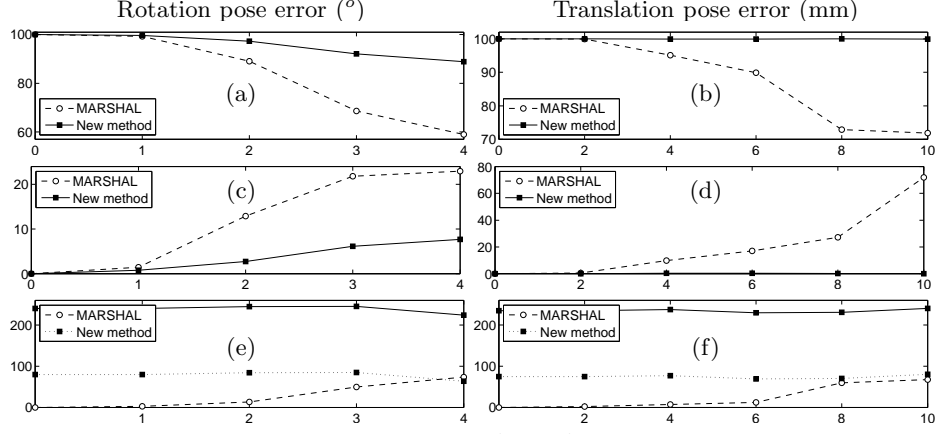


Fig. 1. Performance comparison between MARSHAL and the new method for pose error. (a)-(b): Mean of matching rate (%), (c)-(d): STD (%), (e)-(f): Computation time (s), dotted line: time required solely for cost minimization (new method).

Table 1. Feasibility and optimality of the proposed method for pose error.

Number of cost coef.	Feasibility rate					Guaranteed optimality rate				
	20n	50n	100n	500n	1000n	20n	50n	100n	500n	1000n
Error 1 °	0.9	0.96	1	1	0.98	0.88	0.91	0.94	0.98	1
Error 2 °	0.9	0.98	1	0.98	0.94	0.35	0.38	0.46	0.6	0.71
Error 3 °	0.58	0.94	0.98	0.94	0.92	0.1	0.13	0.13	0.22	0.27
Error 4 °	0.42	0.83	0.92	0.92	0.85	0.15	0.1	0.07	0.07	0.1
Error 2 mm	0.96	1	1	1	0.94	1	1	1	1	1
Error 4 mm	0.94	0.98	1	1	0.92	0.56	0.6	0.65	0.77	0.89
Error 6 mm	0.96	0.96	1	0.96	0.88	0.35	0.41	0.46	0.63	0.64
Error 8 mm	0.77	0.9	0.98	0.94	0.88	0.14	0.19	0.19	0.31	0.38
Error 10 mm	0.58	0.92	0.96	0.94	0.77	0	0.02	0.04	0.07	0.08

used in the computation of the cost coefficients. However, computing all the cost coefficients is not required since most of them will eventually be thrown out by dimensionality reduction. After further code optimization, we expect the computation time to reduce, near to the time required solely for cost minimization (dotted line).

The feasibility and optimality rates of the proposed method as a function of the number of remaining cost coefficients after dimensionality reduction are shown in Tab.1. It is expected that the feasibility rate should increase as a function of the number of cost coefficients. This is true for smaller numbers of cost coefficients but, surprisingly, the feasibility rate decreases when the number of cost coefficients reaches $500n$ ($\simeq 50,000$). This is due to the failure of `linprog` in Matlab using default parameters because “one or more of the residuals, duality gap, or total relative error has stalled”. These cases were not displayed in Fig. 1, and we are currently investigating how to cope with them.

The guaranteed optimality rate increases as a function of the number of cost coefficients. For low errors (1° and 2 mm), all solutions are guaranteed optimal given an acceptable dimensionality ratio. We point out that the guaranteed optimality is only a sufficient condition. As shown in Fig. 1(b), all solutions from 0 to 8 mm translation error of the proposed method correspond to perfect matching (100%), even if they are not all guaranteed optimal.

3.2 Phantom Experiments

A radiographic fiducial was used to track the C-arm (0.56 mm translation; 0.33° rotation accuracy) and was accurately attached to a random point cloud phantom. Phantoms of $\{40, 55, 70, 85, 100\}$ points with 1.56 *points/cc* were used. Six X-ray images within a 20° cone around the AP-axis were *randomly* taken using an *Philips Integris V3000* fluoroscope and dewarped. Thus both the seed locations and X-ray pose were not biased/optimized in any way, closely representing an uncontrolled surgical scenario. Each image was hand segmented to establish the true segmentation and correspondence.

Both MARSHAL and the proposed method perform very well on phantoms, achieving almost perfect matching, as shown in Tab. 2. Note that the accuracy of the radiographic fiducial ensures here a low pose error. The proposed method is significantly slower compared to MARSHAL. We point out that the proposed method uses here more than 90% of the computational time for the n^3 cost coefficients. We expect to reduce significantly this time as explained in Sect. 3.1.

Table 2. Performance of MARSHAL and the proposed method on phantoms.

	MARSHAL					Proposed method				
Number of seeds	40	55	70	85	100	40	55	70	85	100
Mean Match. (%)	97.6	100	98	97.7	98.2	98	99.4	97.1	100	98
STD Match. (%)	3.6	0	2.3	3.2	2.3	2.6	1.4	0	0	0
Time (s)	0.3	0.6	1	2.5	3.1	12.6	32	64.6	106.6	185

Conclusion and Future Work: In summary, we achieved significant increase in the robustness to pose errors compared to [1] by considering all images simultaneously, instead of using subsets. Experimentally, our method ensured optimality for small pose errors. C-arm tracking is a cumbersome process and easing on this constraint has great practical utility. With our method, a less accurate estimation of the pose may suffice. For example in [4], starting from an initial guess, pose was further estimated iteratively using the current 3D reconstruction, yet the seed matching remained susceptible to pose errors. Applying our method to [4] promises a clinically viable solution without using external tracker or encoder on the C-arm. We are also extending the method to reconstructing overlapping seeds that are occluded in one or more X-ray images [5, 6].

References

1. Jain, A. et al: Matching and reconstruction of brachytherapy seeds using the hungarian algorithm (marshal). *Med Phys* **32**(11) (Nov 2005) 3475–92
2. Papadimitriou, C.H., Steiglitz, K.: Combinatorial optimization: algorithms and complexity. Prentice-Hall, Inc. (1982)
3. Bertsekas, D.: Nonlinear Programming. Athena Scientific, Belmont, USA (1999)
4. Jain, A. et al: C-arm tracking and reconstruction without an external tracker. In: MICCAI. (Oct 2006) 494–502
5. Su, Y. et al: Prostate brachytherapy seed localization by analysis of multiple projections: Identifying and addressing the seed overlap problem. *Med Phys* **31**(5) (May 2004) 1277–87
6. Narayanan, S. et al: Three-dimensional seed reconstruction from an incomplete data set for prostate brachytherapy. *Phys in Med and Bio* **49**(15) (Aug 2004) 3483–94

C-arm Calibration - is it really Necessary?

Ameet Kumar Jain^a, Michael An^b, Nicha Chitphakdithai^b, Gouthami Chintalapani^a, and Gabor Fichtinger^{a,c}

^aDepartment of Computer Science, Johns Hopkins University

^bDepartment of Bio-medical Engineering, Johns Hopkins University

^cDepartment of Radiology, Johns Hopkins University

ABSTRACT

C-arm fluoroscopy is modelled as a perspective projection, the parameters of which are estimated through a calibration procedure. It has been universally accepted that precise intra-procedural calibration is a prerequisite for accurate quantitative C-arm fluoroscopy guidance. Calibration, however, significantly adds to system complexity, which is a major impediment to clinical practice. We challenge the status quo by questioning the assumption that precise intra-procedural C-arm calibration is really necessary. Using our theoretical framework, we derive upper bounds on the effect of mis-calibration on various algorithms like C-arm tracking, 3D reconstruction and surgical guidance in virtual fluoroscopy - some of the most common techniques in intra-operative fluoroscopic guidance. To derive bounds as a function of mis-calibration, we model the error using an affine transform. This is fairly intuitive, since small amounts of mis-calibration result in predictably linear transformation of the reconstruction space. Experiments indicate the validity of this approximation even for 50 mm mis-calibrations.

The problem is twofold: (a) C-arm intrinsic calibration; and (b) C-arm distortion correction. Using our theoretical and experimental analysis on mis-calibrated C-arms, we propose a hypothesis that indicates that intrinsic calibration might not be required for a family for surgical procedures. The framework also makes suggestions to the current work flow so as to further minimize the effect of any inherent mis-calibration. To address the problem of pose dependant distortion correction, we propose the use of a framework that can statistically study the maximum variation in distortion near a certain pose and then intra-operatively use an average correction. These theoretical derivations and experimental results make a strong case for the use of mis-calibrated C-arms, obviating the cumbersome intra-operative calibration process, potentially boosting clinical applicability of quantitative fluoroscopy in many procedures. We also prove this hypothesis experimentally.

Keywords: C-arm Calibration, 3D fluoroscopic guidance.

1. INTRODUCTION

C-arm fluoroscopy is ubiquitous in general surgery, due to its real-time nature, versatility, and low cost. At the same time, quantitative fluoroscopy has not found a *large scale clinical acceptance*, because of some inherent technical difficulties. It needs to solve four major problems: (1) C-arm image distortion; (2) Calibration of model parameters; (3) Pose recovery or tracking when multiple images are taken; and (4) Registration to other imaging modalities. Quantitative fluoroscopy could enable a significant improvement in the current clinical practice, the prominent works tackling some of the above problems.^{1,2}

If it is known that both image distortion³ and intrinsic calibration^{4,5} may vary significantly with pose. The intrinsic parameters themselves can be classified into two broad categories - pixel size and location of X-ray source (focal spot) with respect to the image intensifier. The pixel size of a C-arm is usually constant throughout the life of the C-arm, depending on the actual electronic hardware. The location of the X-ray source on the other hand varies from pose to pose due to the flexibility in the mechanical design and the large weight of the X-ray source.

Honorable Mention Poster Award. Send correspondence to {jain, gabor}@cs.jhu.edu

Image distortion usually has a consequential contribution to reconstruction error and needs to be compensated. Thus the additional cost of a full online calibration is not substantial. Recently developed advanced intensifier tubes allow for lesser distortion, while modern flat panel detectors obviate distortion correction altogether. This fact brings up the question whether we need to calibrate the C-arm fully at each pose. The question also leads to the broader issue, that even if it is not pose dependent, how accurate does calibration need to be. In spite of the importance of calibration in C-arm fluoroscopy, as far as the authors are aware, there has been no prior work that conducts this kind of analysis. The vision community has a similar problem^{6, 7} when cameras are used for visual serving of robots. In essence, this paper addresses the issue of sensitivity of 3D fluoroscopy to mis-calibration.

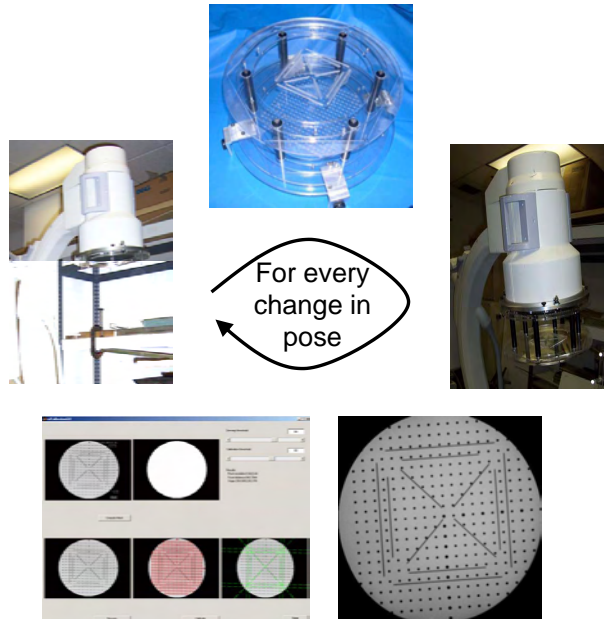


Figure 1. The C-arm intrinsic calibration is pose dependant. Hence conventional methods for fluoroscopic guidance need to calibrate the C-arm at every pose, a significant liability for intra-operative navigation. Traditionally, a calibration phantom is attached to the image intensifier, an X-ray image is taken and sent to a calibration module. The phantom is then removed, making the C-arm ready for use with the patient. This is repeated for every desired pose.

In quantitative C-arm fluoroscopy, we typically need to measure the spatial transformation between two objects, such as a vertebra and a bone drill, as compared to the transformation between an object and the C-arm itself. Thus the central intuition of this paper is that *while an incorrect calibration gives erroneous estimates for the absolute transformations, nevertheless it still provides acceptable relative estimates*. The consequence of this conjecture is potentially far reaching, as it can turn fluoroscopy to an affordable quantitative measurement tool in a large family of procedures. It should however be noted that we do not claim that calibration would always be unnecessary, since there are some applications that require accurate absolute estimates, as can be observed in cone beam computed tomography.⁵ The decision should always be made case by case, experimentally.

The driving application for the proposed hypothesis is virtual fluoroscopy (VF), where synthetically created X-ray images in conjunction with image-guidance aids the surgeon in accurately targeting the anatomy.⁸ Furthermore, it significantly decreases the amount of radiation dose imparted to the surgeon, which has been typically very high in these family of procedures. In this paper, we build a mathematical framework to formally address this issue and lend credit to the intuition that a loose estimate of the C-arm parameters might suffice. Furthermore, our theoretical derivations also provide us with minor modifications to the current VF procedures,

so as to minimize the effect of any inherent mis-calibration. In essence, we prove in theory and demonstrate experimentally that VF is feasible with an un-calibrated C-arm.

2. MATHEMATICAL FRAMEWORK

C-arm Imaging: Geometric aspects of fluoroscopic imaging can be modelled as a perspective transformation with five parameters - focal length, image origin and pixel size (Figure 2). The transformation formula is given in equation (1), (2); where F_O, F_X, F_I are the coordinate frames of an object, X-ray source and the image, respectively; P is a 3D point; P_O are the homogenous coordinates of P in F_O ; p is the projection of P on the image plane; p_I are the homogenous coordinates (in pixels) of p in frame F_I ; ${}^X F_O$ is the 4x4 rigid transformation matrix that transforms a point in F_O to F_X (also called pose); ${}^I F_X$ is the 3x4 perspective projection matrix; f is the focal length; $O = (o_x, o_y)$ is the projection of the X-ray source on the image plane (later referred to as the origin); s_x and s_y are the pixel sizes along the X and Y axis of the image.

$$p_I = {}^I F_X \quad {}^X F_F \quad P_F \quad (1)$$

$${}^I F_X = \begin{bmatrix} -f/s_x & 0 & o_x & 0 \\ 0 & -f/s_y & o_y & 0 \\ 0 & 0 & 1 & 0 \end{bmatrix}, \quad {}^X F_O = \begin{bmatrix} r_{11} & r_{12} & r_{13} & T_1 \\ r_{21} & r_{22} & r_{23} & T_2 \\ r_{31} & r_{32} & r_{33} & T_3 \\ 0 & 0 & 0 & 1 \end{bmatrix} \quad (2)$$

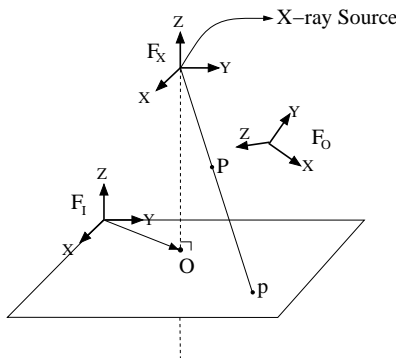


Figure 2. Projective geometry and notations for fluoroscopic imaging.

There are a total of five independent parameters that need to be evaluated by the calibration procedure - the pixel sizes (two) and the focal spot (three). Note that owing to the mathematics of projective imaging, these intrinsic parameters can only be estimated up to an arbitrary scale (which determines the physical size of the C-arm). Hence instead of the pixel sizes, the aspect ratio (ratio of pixel sizes) is typically used. Since the aspect ratio remains unchanged throughout the life of the C-arm, online-calibration essentially reduces just to the location of the focal spot. The proposed theoretical framework can be used to study sensitivity due to any of the five parameters, nevertheless, we limit ourselves only to that of the focal spot.

2.1. Model for Reconstruction Space Transformation

As illustrated in Figure 8, let A & B (with reference frames F_A & F_B) be the two objects being imaged. The assumptions are: (i) ${}^I F_A, {}^I F_B$ can be computed from the images; (ii) A & B are *not large* in comparison to the focal length; (iii) F_A and F_B are *close by*; and (iv) the quantity of interest is ${}^A F_B = ({}^I F_A)^{-1} {}^I F_B$. Let \bar{f}_1 be the true focal spot and $\bar{f}_2 = (\bar{f}_1 + \bar{D})$ be the mis-calibrated estimate. We claim that even though the absolute locations of the objects are off, their relative transformation might still be accurate.

$$[{}^I F_A(\bar{f}_1)]^{-1} {}^I F_B(\bar{f}_1) \sim [{}^I F_A(\bar{f}_2)]^{-1} {}^I F_B(\bar{f}_2) \quad (3)$$

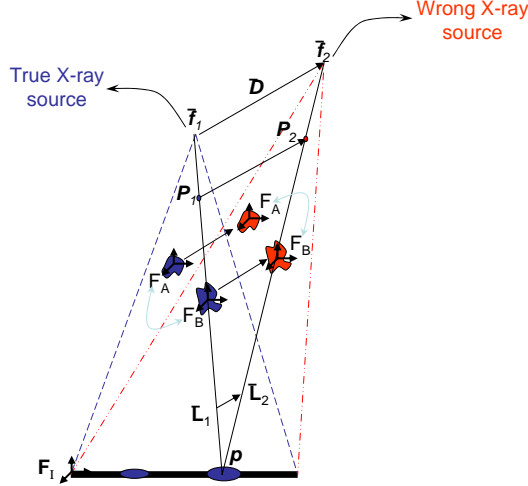


Figure 3. Mis-calibration shifts all reconstructed objects under an affine transformation.

A transformation is needed that can take the absolute location of an object reconstructed with calibration \bar{f}_1 , and compute its corresponding location with calibration \bar{f}_2 . We claim that the simplest transformation will be a linear affine model \mathcal{T} . The intuition derives from the observation that the image plane is the same in both reconstruction spaces. Thus if P_1 (not in homogenous coordinates) projects to a point p on the image, then it is constrained to be on line \bar{L}_1 in the \bar{f}_1 -space and on \bar{L}_2 in \bar{f}_2 -space. Thus we seek a continuous invertible transformation that projects \bar{L}_1 to \bar{L}_2 . By incorporating the above constraints, \mathcal{T} can be evaluated to be,

$$P_2 = \mathcal{T} \cdot P_1 = \begin{bmatrix} 1 & 0 & D_x/f_{1z} \\ 0 & 1 & D_y/f_{1z} \\ 0 & 0 & 1 + (D_z/f_{1z}) \end{bmatrix} \cdot P_1 = P_1 + (d \cdot Z/f_{1z})\hat{D} \quad (4)$$

where with respect to (wrt) F_I , $\bar{D} = (D_x, D_y, D_z)$; $d = \|\bar{D}\|_2$; $\hat{D} = \bar{D}/d$; $\bar{f}_1 = (f_{1x}, f_{1y}, f_{1z})$; and $P_1 = (X, Y, Z)$. Each point is effectively translated in direction \hat{D} by an amount proportional to its distance from the image. Experiments measuring the correctness of this affine model are available in Section 3. Thus to study sensitivity, it is sufficient to study the properties of \mathcal{T} .

Changes in Length and Scale \mathcal{T} preserves the scale along the x, y -axes, but scales the space along the z -axis. Let $P_1(X_1, Y_1, Z_1)$ & $P_2(X_2, Y_2, Z_2)$ be any two points (not necessarily close to each other) in the \bar{f}_1 -space at a distance of l_1 . \mathcal{T} maps them to points Q_1 & Q_2 in the \bar{f}_2 -space at a distance of l_2 (Figure 4 (a)). It can be shown that

$$l_2^2 = l_1^2 + \frac{d^2}{f_{1z}^2}(Z_1 - Z_2)^2 + 2\frac{(Z_1 - Z_2)}{f_{1z}}\bar{D} \cdot (P_1 - P_2) \quad (5)$$

$$\|l_2 - l_1\| \leq \frac{d}{f_{1z}}|Z_1 - Z_2| \quad (6)$$

$$\implies l_1[1 - \frac{d}{f_{1z}}] \leq l_2 \leq l_1[1 + \frac{d}{f_{1z}}] \quad (7)$$

It directly follows from Equation (6) that \mathcal{T} does not alter the length significantly. As an example, a 10 mm calibration error would affect the length of a 30 mm thoracic pedicle screw at an angle of 45° by less than 0.2 mm (focal length ~ 1 m), which is significantly less than the error from other sources. Thus F_A, F_B will not change their relative translation by a factor more than that specified by Equation (6).

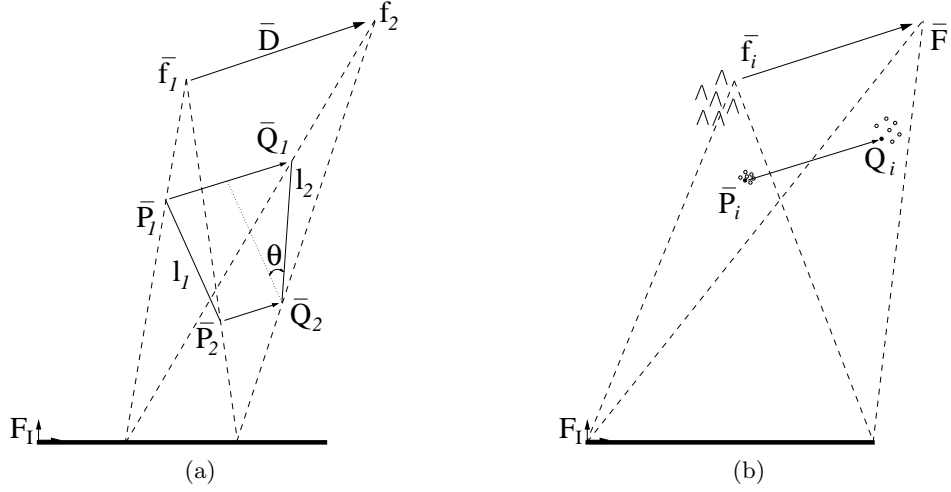


Figure 4. (a) Mis-calibration rotates and scales a straight line segment. (b) Pose dependent calibration might be successfully approximated by using the mean value.

Changes in Absolute Orientation A change in orientation results from the object having a depth (Figure 4 (a)). It can be shown geometrically that the orientation error is maximal when the vector $\bar{P}_1\bar{P}_2$ is roughly orthogonal to \bar{D} and is purely in the vertical plane. The amount (θ) and the axis ($\hat{\kappa}$) of rotation, through a series of computations can be shown to be as in Equation (8). The bound on the rotation error is dependent only on origin mis-calibration and not on that in focal length. More importantly it is independent of the height/depth of the object (as far as it is non-planar) and its distance from the image plane. Thus F_A, F_B in Figure 8 will observe the same absolute rotation, in effect not experiencing any relative rotation. Experimental results corroborating this claim are available in Section 3.

$$|\theta| \leq \arcsin \left[\frac{\sqrt{D_x^2 + D_y^2}}{f_{1z}} \right] \sim \frac{\sqrt{D_x^2 + D_y^2}}{f_{1z}} ; \quad \hat{\kappa} = \frac{1}{\sqrt{D_x^2 + D_y^2}} (D_y, -D_x, 0) \quad (8)$$

Error in Reconstruction of Point Features In many applications (particularly in brachytherapy), C-arms are used to reconstruct 3D point objects. This is done by obtaining multiple images at varying orientations and then using triangulation to obtain the desired intersection. In ideal circumstances, all the lines would intersect at a unique point. In practice however, calibration (and other) errors lead to non-intersecting lines. We will attempt to bound the error in this symbolic reconstruction of the point. Let point P be imaged from N different poses and reconstructed in a tracker frame F_A , which is stationary wrt P . Let the i^{th} pose have a focal spot error (in frame F_A) of \bar{D}_i . Without errors, each reconstructed line (l_i) would pass through P . It can be shown that due to the calibration error \bar{D}_i , the new line passes through a new point \bar{P}'_A and undergoes a rotation ϕ .

$$\bar{P}'_A \sim \bar{P}_A + [0 \ 0 \ \frac{(\bar{P}_A \cdot \bar{D}_i)}{f_{iz}}]' ; \quad \phi \sim \frac{(\hat{l}_i \cdot \bar{D}_i) \sin \theta_i}{f_{iz}} \quad (9)$$

where θ_i is the angle that l_i makes with the z-axis of F_A . The rotation is fairly small and can be ignored. Thus P_A is at a distance of $(\bar{P}_A \cdot \bar{D}_i) \sin \theta_i / f_{iz}$ from l_i . If Q is the symbolic intersection of all l_i 's, then it can be shown that Q is no further away than $(\frac{d_{max}}{f_z} \sin \theta_{max}) \|P_A\|$ away from any of the lines. Moreover, the reconstruction error (RE) can also be shown to be bounded by

$$RE = \|(Q - \bar{P}_A)\| < \frac{\sqrt{2} d_{max}}{f_z} \|\bar{P}_A\| \quad (10)$$

where d_{max} is the maximum amount of mis-calibration and f_z is the minimum focal length. Thus a 10 *mm* focal length error causes an error less than 0.5 *mm* for a point at a distance of 35 *mm*. Note that this is the worst case error analysis and in practice the dot product in Equation (9) mutually cancels positive and negative errors, leading to extremely low reconstruction errors (Section 3).

The Optimal Choice for Calibration Parameters Since the focal spot is pose dependant, and the previous results suggest robustness to mis-calibration, choosing a constant calibration for quantitative reconstruction might be viable. In the scenario that the focal spot might vary as much as 10 *mm* from one pose to another, “*what constant calibration should be chosen to minimize error*”?

Let us assume that we are imaging a point P from N different poses (Figure 2 (c)). Wrt frame F_I , let the i^{th} pose have the focal spot at $\bar{f}_i = (f_{ix}, f_{iy}, f_{iz})$ and the point be at location $P_i = (X_i, Y_i, Z_i)$. Note that we assume: (a) variations in each of $f_{ix}, f_{iy}, f_{iz}, X_i, Y_i, Z_i$ & pose are independent; (b) P_i ’s are close to the iso-center, *i.e.* variations in X_i, Y_i, Z_i are not high. We choose a constant value of $\bar{F} = (F_x, F_y, F_z)$ for the focal spot, which will displace the point P_i to $Q_i = \mathcal{T}(\bar{f}_i, \bar{F}) \cdot P_i$. The aim is to choose an \bar{F} which minimizes the net variation of $\Delta Q_i = Q_i - \mu_Q$. Through a series of computations, it can be shown that

$$\mu_Q = \mu_P + \frac{\mu_z}{\mu_{fz}}(\bar{F} - \bar{\mu}_f) \quad (11)$$

$$\Delta Q_i = (P_i - \mu_P) + \left[\frac{\Delta Z_i}{\mu_{fz}} - \frac{\mu_z \Delta f_{iz}}{\mu_{fz}^2} \right] \bar{F} + \frac{\mu_z \Delta f_{iz}}{\mu_{fz}^2} \bar{\mu}_f - \frac{\Delta Z_i}{\mu_{fz}} \bar{\mu}_f - \frac{\mu_z}{\mu_{fz}} \Delta \bar{f}_i \quad (12)$$

where $\mu_Q, \mu_P, \mu_z, \mu_{fz}, \bar{\mu}_f$ are the mean values of $Q_j, P_j, Z_j, f_{jz}, \bar{f}_j$; $Z_j = \mu_z + \Delta Z_j$ and likewise for f_{jz}, \bar{f}_j , where $j = 1 \dots N$. In the above calculations, the second order terms either summed to 0 due to the independence of the variables or were too small in comparison. Our choice of \bar{F} should be the one that minimizes the *variance*(ΔQ) = *var*(ΔQ_x) + *var*(ΔQ_y) + *var*(ΔQ_z). It should be noted that F_z scales the whole space, *i.e.* a lower value will decrease the variance, implying that the choice of $F_z = 0$ forces *var*(Q_z) = 0 by forcing all Q_i ’s to lie on a plane. Thus *var*(Q_z) does not provide sufficient constraints for F_z . We will first obtain F_x, F_y by minimizing the variance along x, y -axes (since there is no scaling in these directions), and then will compute F_z . Notice that the first term in Equation (12) is due to the relative movement in P , while the rest is due to an error in the calibration. Since we are interested only in the variance due to mis-calibration, we will ignore the variations in P . Minimizing *var*(ΔQ) and enforcing independence of f_{ix}, f_{iy} & f_{iz} gives

$$\bar{F} = \bar{\mu}_f - \frac{\sum_1^N \Delta f_{iz} \Delta \bar{f}_j}{\sum_1^N \Delta f_{iz}^2} \mu_{fz} = [\mu_{fx}, \mu_{fy}, 0]^T \quad (13)$$

As expected, $F_z = 0$ from above. To compute F_z , we need to impose length preserving constraints. Thus if we measure a line segment of length l in each image, use Equation (6) to derive the net length error, the minimization implies

$$F_z = \mu_{fz} \left(1 - \frac{\sum_1^N \Delta f_{iz}^2}{N \mu_{fz}^2} \right) \sim \mu_{fz} \quad (14)$$

Thus $\bar{F} = \bar{\mu}_f$ (the mean), which is fairly intuitive and probably in common practice. Likewise, this particular choice of F_x, F_y is also a length preserving constraint, *i.e.* it minimizes the error in lengths of line segments. Calibration error in ΔQ_i now reduces to $-\frac{\mu_z}{\mu_{fz}} \Delta \bar{f}_i$, which has a stable mean and low variance. Equation (15) gives a bound on the error when the assumed value of \bar{F} is away from the mean $\bar{\mu}_f$ by a distance d . A 10 *mm* variation in the focal length (*var* \sim 3 *mm*), P ’s roughly at the iso-center having a depth variation of 100 *mm* and the assumed calibration unusually away from $\bar{\mu}_f$ by 50 *mm* still bounds the maximum error by 0.75 *mm*.

Thus large and constant mis-calibration in many applications, might still provide sub-millimetric 3D quantitative measurements.

$$error \leq \frac{\sqrt{d^2 var(Z) + \mu_z^2 var(\|f\|)}}{\mu_{fz}} \quad (15)$$

2.2. Mis-calibration and its effect on Virtual Fluoroscopy

In traditional C-arm fluoroscopy, surgeons often use C-arms whenever they want to know the location of a tool inside the patient. In virtual fluoroscopy (VF), X-ray images are created synthetically with the position of the tool (tracked in 3D) superimposed on the 2D images. This not only adds to the targeting accuracy, but also reduces the radiation dose both to the surgeon and the patient. Thus VF allows the tool's position to be known without taking a new image each time.⁸

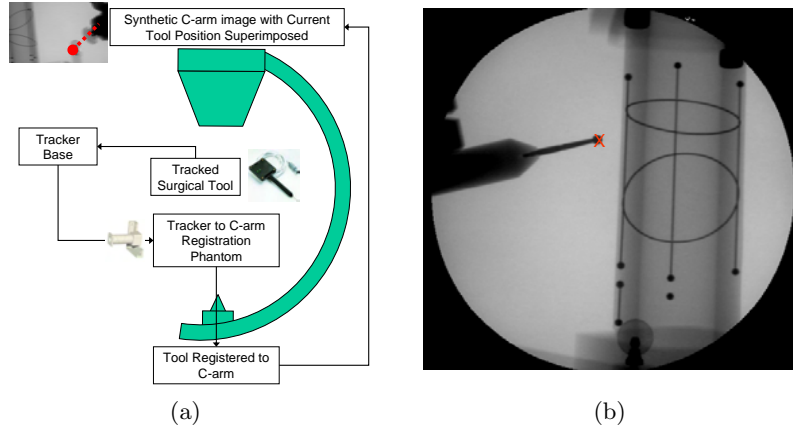


Figure 5. (a) The overall dataflow for a virtual fluoroscopy system. The current 3D tool location is registered to a previously taken C-arm image of the patient, and then rendered artificially on the image. Two such images can provide real-time 3D guidance, without the need to take more images. (b) An example screen-shot of our implemented virtual fluoroscopy system. The 'x' denotes the system's projected tool-tip position, overlaid on top of the corresponding dewarped image. For reference, the *true* location of the projected tool tip is also visible in the X-ray image. The FTRAC fiducial used to register the tracker to the C-arm is also visible.

As illustrated in Figure 5, the tool is tracked realtime in 3D using an auxiliary tracking system. The tracker is registered to the C-arm using some sort of a prefabricated precision phantom, visible both to the tracker and in the X-ray image. This allows for the projection of the current 3D tool location on a previously taken X-ray image of the anatomy, essentially creating a 'virtual' X-ray image. A prerequisite for projecting the current tool location on the image is to know the location of the X-ray image wrt the X-ray source accurately (otherwise known as C-arm calibration).

Traditionally, the C-arm is extensively calibrated with each change in pose before taking an image, which is a cumbersome procedure. A typical such phantom is illustrated in Figure 1. This naturally leads us to ask '*is it actually necessary to calibrate the C-arm for every change in pose?*'. More importantly, how precise does the calibration need to be for a *desired* accuracy in a surgical procedure. In what follows, using the mathematical framework developed so far, we study the effect of this mis-calibration on the accuracy of tool projection.

To develop the framework, we constrain the tool only to a point, which is reasonable since most tools are a collection of 3D points attached rigidly to the tracker on the tool (for ex. an insertion needle). We start with adding a calibration error of $\bar{D} = (D_x, D_y, D_z)$ in the source position wrt the image. The results in Equation

(4), (8) indicate that the primary errors are in the plane containing the true X-ray source, incorrect X-ray source and orthogonal to the image. We will refer to this plane as the *error-plane* and is illustrated in Figure 6. Thus this plane can be assumed to be the base plane with the mis-calibration $\bar{D} = (\sqrt{D_x^2 + D_y^2}, 0, D_z)$. For simplicity of calculation, we will drop the y-coefficient and assume $\bar{D} = (\sqrt{D_x^2 + D_y^2}, D_z)$.

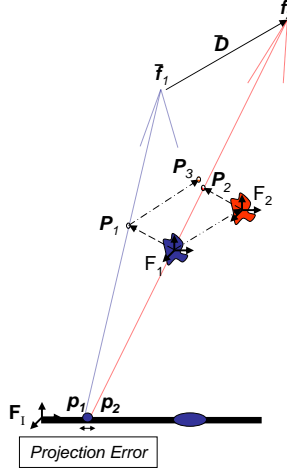


Figure 6. With the true calibration \bar{f}_1 , the 3D point P_1 wrt F_1 projects to p_1 in the image. Due to the incorrect estimate \bar{f}_2 , F_1 is mis-estimated at F_2 , moving the point from P_1 to P_2 , eventually projecting at p_2 in the image. P_3 is a convenient 3D point, which when projected from \bar{f}_2 projects on p_1 . $\|p_1 - p_2\|$ represents the error in the system due to mis-calibration. Note that the error is assumed in the X-Z plane without any loss in generality.

Let F_1 be the true frame coordinate of the Tracker to C-arm registration phantom, and F_2 be the frame of the phantom as computed using an incorrect calibration. Though illustrated such, F_1, F_2 are not necessarily in the error plane. The relationship between F_2 and F_1 is as evaluated in Equation (4), (8), involving a translation in the direction of \bar{D} and a rotation along the Y-axis. Let $P_1 = (a, b)$ be the true location of the tool tip wrt the phantom in frame F_I . Note that this value (when expressed in frame F_1) is independent of C-arm calibration and is computed using the tool to tracker-base transformation and tracker-base to phantom registration. Let P_2 (expressed in frame F_I) be the new location of the tool tip wrt the phantom when the frame of the phantom has been reconstructed using a mis-calibrated C-arm (F_2). Let p_1 be the true projection of the tool tip from P_1 , and p_2 the mis-calibrated projection of the tip from P_2 . Note that p_1, p_2 will not be the same in general, the difference representing the projection error due to mis-calibration in a VF system. We will attempt to compute an upper bound on this error.

To compute $\|p_1 - p_2\|$, we introduce another 3D point P_3 , such the P_3 when projected from the mis-calibrated X-ray source, projects on the 2D point p_1 . Thus points P_2, P_3 when projected using the mis-calibrated parameters, can be used to estimate $\|p_1 - p_2\|$. One example point for P_3 , computed using Equation (4), is as satisfied by the equation below, where Z_1 is the Z-coordinate of point P_1 wrt F_I .

$$P_3 - P_1 = \left(\frac{Z_1}{f}\right)\bar{D} \quad (16)$$

Note that P_2 wrt frame F_2 is same as P_1 wrt frame F_1 . Let this vector be \bar{v} . If θ as computed by Equation (8) be the angle of rotation (along the new Y-axis), then \bar{v} is rotated by θ along the Y-axis of the C-arm. Thus P_2 can be computed from P_1 by applying the translation and rotation of from F_1 to F_2 as given by Equations(4), (8). If Z_F is the Z-coordinate of point F_1 wrt F_I , then

$$\begin{aligned}
P_2 - P_1 &= Translation(\bar{v}) + Rotation(\bar{v}) \\
&= [(\frac{Z_F}{f})\bar{D}] + [(b, -a)\sin\theta - (a, b)(1 - \cos\theta)] \\
&\approx \frac{Z_F}{f}\bar{D} + (b, -a)\frac{\sqrt{D_x^2 + D_y^2}}{f} - (a, b)\frac{D_x^2 + D_y^2}{f^2} \\
&\approx \frac{Z_F}{f}\bar{D} + (b, -a)\frac{\sqrt{D_x^2 + D_y^2}}{f}
\end{aligned} \tag{17}$$

Note that we have not written down the components of P_1, P_2, P_3 along the Y-axis. This is because, the affine transformation model does not make any transformations (rotation or translation) along this axis, resulting in *no change* from P_1 to P_2, P_3 . From Equations (16) & (17), we get

$$\begin{aligned}
P_2 - P_3 &= \frac{-b\bar{D} + (b, -a)\sqrt{D_x^2 + D_y^2}}{f} \\
&= \frac{-b(\sqrt{D_x^2 + D_y^2}, D_z) + (b, -a)\sqrt{D_x^2 + D_y^2}}{f} \\
&= (0, -\frac{a\sqrt{D_x^2 + D_y^2} + bD_z}{f}) \\
&= (0, \beta)
\end{aligned} \tag{18}$$

Note that the x-coordinate of the vector $\bar{P}_2 - \bar{P}_3$ is zero. We will use this special structure to evaluate $\|p_2 - p_1\|$. For this computation, we can assume without loss of generality that F_I is located at the origin of the mis-calibrated image plane. If wrt F_I , $P_3 = (x, y, z)$ (y-coordinate included) then $p_1 = (f'/f' - z)(x, y)$, where f' is the mis-calibrated focal length. Since $P_2 = P_3 + (0, 0, \beta)$, it can be shown that

$$\begin{aligned}
\|\bar{p}_1 - \bar{p}_2\| &= \|\frac{f'}{f' - z}(x, y) - \frac{f'}{f' - z - \beta}(x, y)\| \\
&= \|\frac{\beta}{f' - z - \beta}\bar{p}_1\| \\
&= (\frac{f'}{f' - z}) (|\beta|) (\frac{\sqrt{x^2 + y^2}}{f' - z - \beta}) \\
&\approx m|\beta|\tan\phi
\end{aligned} \tag{19}$$

where m is the magnification factor of the 3D point and ϕ is the angle that the 3D point makes with the projection axis of the C-arm (the line joining the X-ray source and the origin, usually very close to the center of the image). Thus the error due to mis-calibration in a virtual fluoroscopy system is

$$\begin{aligned}
\|\bar{p}_1 - \bar{p}_2\| &\approx m\tan\phi \frac{a\sqrt{D_x^2 + D_y^2} + bD_z}{f} \\
\Rightarrow 3DError &\approx \frac{(a, b) \cdot (\sqrt{D_x^2 + D_y^2}, D_z)}{f} \tan\phi
\end{aligned} \tag{20}$$

From Equation (20) it can be noticed that the error in a VF system can be significantly reduced by: (a) bringing the tracked tool closer to the center of the image; and/or (b) using a registration phantom that can work near the tool workspace. To get a sense of the numbers, if the tool is somewhere in the middle of the C-arm workspace (magnification = 2) & projects at the corner of a 9" image intensifier ($\tan\phi \approx 0.12$), then a mis-calibration as high as even 50 mm will not induce an error greater than 1 mm in a VF system, if the registration phantom is used inside a 100 mm region of the tool workspace. Alternately, even if the registration phantom needs to be kept far away (at a distance of, say, 250 mm), then keeping the projection of the tool in a 40 mm diameter region near the image center, will still produce an error less than 1 mm with a 100 mm mis-calibration. Note that a 1 mm error in the image at a magnification of 2, indicates only a 0.5 mm 3D error (when multiple images are used, as is customary). Also note that in most cases, typical mis-calibrations are predominantly in the imaging direction, in which case, it suffices if the registration phantom can be used at the same 'depth' as the tool workspace. In such cases, the dot product in Equation (20) cancels out, ensuring that no error is added in the tool guidance of the VF system.

2.3. Distortion Correction

C-arm images suffer from image distortion (as high as 5 mm), owing to the curved nature of detector (radial distortion) and the earth's magnetic field³ (s-shaped distortion). In order to achieve quantitative surgical navigation, the distortion needs to be corrected for. This is cumbersome, more so, since the warp is pose dependent. Traditional distortion correction techniques use a calibration phantom¹⁻⁴ and characterize the distortion by fitting a high-order polynomial between the distorted image and the expected image. Though easy to use, they are cumbersome for intra-operative correction due to: 1) the interference between the patient anatomy and the phantom; and 2) increased radiation dose & surgical time when two images are used, one with and the other without the phantom. Alternately, the distortion parameters at a particular pose could be interpolated from the multiple neighboring poses taken pre-operatively,³ but require accurate c-arm tracking. The intra-operative use of the same c-arm pose, as was used pre-operatively for distortion correction, has also been proposed,² though it requires the c-arm pose to be repeatable and hence could become time-consuming when collecting many images. All in all, online distortion correction has been a cumbersome problem, without a reliable/robust solution.

In line with the general theme of the paper, we observe that image distortion does not radically change between two *neighboring* poses, *i.e.* small movements if the C-arm result in small variations in image distortion. This suggests that it might suffice to use a *constant* distortion correction in a *small* region of interest (ROI). Unfortunately, the definition of a *small* ROI or *neighboring* poses is not clear and tools that can crisply characterize these ideas have not yet been developed. In what follows, we propose some simple yet powerful tools to further reinforce these ideas from a quantitative perspective.

Statistical Characterization of C-arm Distortion: C-arm distortion has been traditionally modelled using a high-order polynomial. This polynomial is computed by using a phantom grid with radio-opaque beads in a known pattern, where the observed distorted image is compared to the expected image. Among the many basis polynomials, the authors have found the Bernstein basis of order 4/5 as sufficiently robust & fast, as also observed in the literature.² Once the polynomials are computed, they can be used to estimate the amount of sub-pixel distortion at any given pixel in the image. This computation can be done independently for multiple pre-operative images. To study precisely the extent of statistical variations in distortion among images of a certain ROI, a principal component analysis (PCA) can be conducted on all the distortion maps. To do so, the distortion map for each image, discretised at each pixel, is organized as a single vector in a very high dimensional space. Thus each distortion map is a single point in this high-dimensional space. To quantitatively study the amounts of variation, it shall suffice to study the statistics of this collection of points. The PCA analysis can be of tremendous aid here, and can provide a linear basis for the subspace of these points, as given below.

$$\bar{D} = \bar{M} + \sum_{i=1}^n \lambda_i \bar{D}_i \quad (21)$$

where \bar{D} is the distortion at any given C-arm pose, M is the mean distortion map of the whole space and D_i is the i^{th} strongest (principal) component (mode). Furthermore, the eigen-values (computed during PCA) associated with each principal mode indicate the variance along each associated direction. This allows for a statistical analysis of the pose-dependant C-arm distortion. It has been observed experimentally that more than 98% of the distortion can be modelled using just the first three principal modes, indicating that though complex, pose dependant C-arm distortion lies predominantly inside a 3-dimensional linear space.⁹

This experimentally determined numerical observation (for a particular C-arm) that, a small movement in the C-arm pose will result in only a small variation in image distortion, can be used to motivate two simple algorithms for distortion correction: (a) use the mean computed from Equation (21) for correcting the distortion within a certain *acceptable* region; (2) if the mean computation is unfeasible, use a *center* image that is geographically *close* to the mean image. Intuitively, if an intra-operative C-arm image is desired *near* a certain pre-calibrated pose, then compute a mean distortion *near* that particular pose. Furthermore, from a quantitative 3D guidance perspective, the use of the pre-operative distortion map itself might suffice in some cases.

3. PHANTOM EXPERIMENTS AND RESULTS

Validity of the Model: Equations (4) & (8) give the translation and rotation transformations as predicted by the affine model, the accuracy of which would furnish the validity of the model. We used the FTRAC fiducial (Figure 7), a small image-based fluoroscope tracking fiducial, which (given the calibration) can track a C-arm with an accuracy of 0.5 mm in translation and 0.65° in rotation.¹⁰ The fiducial was imaged using a Philips Integris V3000 fluoroscope and the true calibration read off the machine display. The images were not corrected for distortion. The pose of the fiducial (wrt to F_I) was first evaluated using the correct calibration, and then with the mis-calibrated parameters. The difference between the pose change predicted by the equations and the one computed using the non-linear pose estimation software, is displayed in Figure 8 (a) as a function of maximum calibration error. A total of 40,500 points (from total 75 poses) with randomly added mis-calibration were used. Even when mis-calibration is as high as 25 mm, the model can predict the rotation-axis with an accuracy of 4°, amount of rotation by 0.1° and translation under 5 mm. For extreme mis-calibrations the translation error linearly increases, while rotation is still stable. Thus the model seems to predict with an acceptable accuracy.

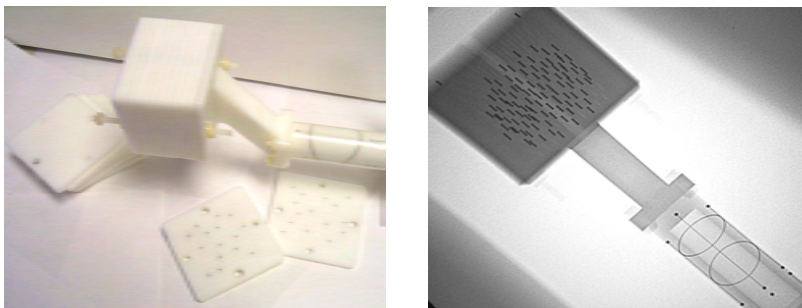


Figure 7. An image of the seed phantom attached to the FTRAC fiducial (left). The seed phantom can replicate any implant configuration, using the twelve 5 mm slabs each with over a hundred holes. A typical X-ray image of the combination (right).

Accuracy of C-arm Tracking: The FTRAC fiducial was mounted on a 0.02° accuracy rotational turntable, while the fluoroscope was kept stationary. The turntable was rotated by known precise amounts (ground truth) and images were taken. The relative poses were also computed using the pose estimation software. The accuracy in the estimation of C-arm motion is given by the difference between the computed relative pose and the true relative pose. The tracking accuracy is plotted in Figure 8 (b) as a function of mis-calibration. Even a high mis-calibration of 150 mm adds no *additional* error in C-arm motion estimation, fixing the value at 0.45 mm in

translation and 0.6° in rotation. An unusually high mis-calibration of 400 mm also only marginally decreases accuracy. Thus, mis-calibration does not increase the error of C-arm tracking .

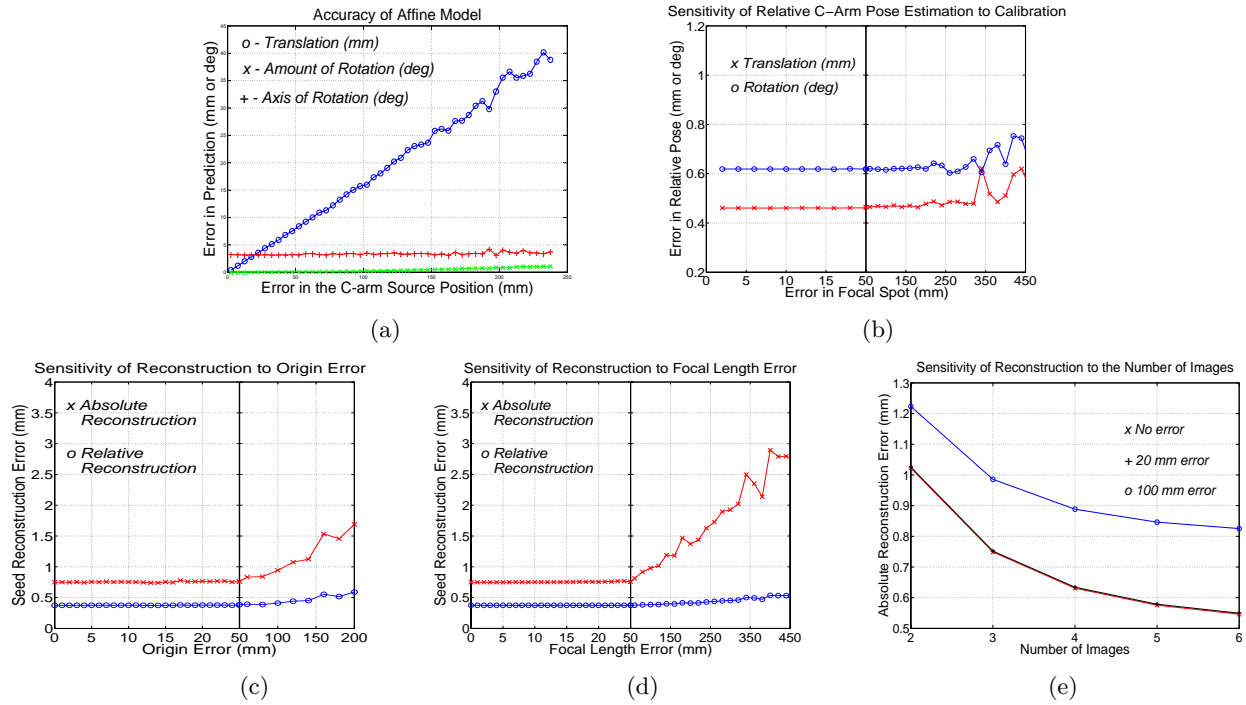


Figure 8. Note the scale variation in x-axis. (a) An affine transformation is able to predict the movement of 3D objects due to mis-calibration; (b) C-arm tracking is insensitive to mis-calibration; 3D Reconstruction is insensitive to mis-calibration in (c) origin ; (d) focal length up to 50 mm, beyond which it starts to linearly drift away from the tracking fiducial. Notice that the shape of the implant (relative error) is barely altered; (e) 3D reconstruction error decreases with an increase in images used.

3D Quantitative Reconstruction using Multiple Images: In addition to tracking a C-arm, it is equally important that multiple objects in the field of view (eg. vertebrae and screws) be reconstructed accurately relative to each other. In order to validate our hypothesis that 3D reconstruction might not be sensitive to mis-calibration, we use an accurate acetol phantom (Figure 7) having 100 dummy radioactive seeds, approximating a brachytherapy implant (Figure 7). The true 3D coordinate of each seed wrt the fiducial is known by rigid attachment. The C-arm is tracked using the FTRAC fiducial and the 3D seed coordinates are computed by triangulation (an algorithm called MARSHAL is used to establish correspondences). The difference between the computed and the true seed location gives us the 3D reconstruction error for each seed (wrt fiducial). The relative reconstruction error removes any consistent shift reflecting any change in shape. These errors are plotted as a function of mis-calibration in Figure 8 (c), (d). The reconstruction error is insensitive to mis-calibration in origin and focal length errors of up to 50 mm. The shape of the implant is stable even for large calibration errors. Figure 8 (e) shows a drop in reconstruction error as the number of images increase. Thus mis-calibration does not decrease reconstruction accuracy.

3D Virtual Fluoroscopy: We implemented an experimental setup in order to evaluate the sensitivity of a VF system to C-arm mis-calibration, the main components of the system being: (a) A GE 9600 C-arm; (b) a precise C-arm distortion correction and calibration toolkit (implemented in Matlab); (c) a Polaris tracker; (d) a calibrated Polaris pointer (calibrated using the NDI ToolViewer); (e) the FTRAC fiducial.

Distortion correction and precise C-arm calibration is performed for the C-arm images using the phantom shown in Figure 1. The phantom is a typical two plate contraption that can be attached to the intensifier. The bottom plate with the evenly spaced metal BB's corrects for any image distortion. Each straight line on the upper plate, along with its projected image-line constraints the X-ray source to a 3D plane. The least square intersection of these ten planes provides an accurate estimate of the source location wrt the image (C-arm calibration). In order to display the current location of the tool in a VF system, the tracker (Polaris) needs to be registered to the C-arm. By virtue of its design, the FTRAC fiducial can register itself to the C-arm (in every image that it is present). Thus, the Polaris to C-arm registration can be achieved by registering the FTRAC fiducial to the Polaris. To realize this, the tracked Polaris pointer was used to digitize 4 straight lines on the FTRAC fiducial, the exact location of which was precisely known from the design file. A non-linear optimization algorithm aligns these straight lines, essentially yielding the FTRAC-Polaris transformation. Note that this registration is C-arm pose independent.

At any given pose of the C-arm, the calibration phantom is used to dewarp the image and to compute the *true calibration*. The phantom is then detached and a new image is taken with both the pointer-tip and the FTRAC fiducial visible in the image (attached steadily using clamps). The 3D pointer location is measured using the Polaris. The location of the pointer tip can now be projected in the X-ray image using the transformation

$$p_{proj} = {}^I\mathcal{P}_C \cdot {}^C F_F \cdot {}^F F_P \cdot {}^P F_T \cdot p_{tip} \quad (22)$$

where p_{tip} is the location of the tool-tip wrt the tool frame (F_T), ${}^P F_T$ is the measured transformation from the tool frame to the Polaris frame (F_P), ${}^F F_P$ is the pre-computed transformation from the Polaris frame to the FTRAC frame (F_F), ${}^C F_F$ is the transformation from the FTRAC to the C-arm frame (F_C) computed for every image, ${}^I\mathcal{P}_C$ is the projective transformation that converts any 3D point to its projection in the 2D image (F_I), and p_{proj} is the (*computed*) VF projected tool-tip location in the image. Note that ${}^I\mathcal{P}_C$ and ${}^C F_F$ will change from one C-arm mis-calibration to another. If p_{seg} is the *true* projection of the tool-tip, segmented from the X-ray image, then $\|p_{proj} - p_{seg}\|$ provides the Euclidean error estimate in the VF system.

A total of 75 such X-ray images were acquired by randomly varying the C-arm pose (15 poses) and the location of the tracked tool wrt the FTRAC fiducial (5 per pose). For any known amount of artificially added mis-calibration, the series of frame transformations was used to project the pointer tip on each image (p_{proj}) and then compared to its corresponding p_{seg} . Thus to experimentally study the sensitivity of a VF system to C-arm mis-calibration, $\|p_{proj} - p_{seg}\|$ is plotted as a function of mis-calibration in various graphs as shown in Figure 9.

It can be seen that the overall average accuracy of our VF system without any mis-calibration is about 2.05 mm (STD 1 mm) in the 2D X-ray images. This indicates a 3D targeting error of about 1 mm at our magnification (0.4), which is reasonable owing to the accuracies of (a) the polaris (0.4 mm); (b) FTRAC (0.6 mm); & (c) pointer calibration (0.2 mm).

Figure 9 (a) - (c) plot the mean/std of the VF system as a function of uniformly distributed mis-calibration. Each graph is computed from a total of 40,500 random points (75 images, 12 intervals, 45 random runs per image per interval). Note that the three plots remain extremely stable & indicate a similar pattern. The mis-calibration in focal length is slightly more critical than the ones in the origin. Furthermore, the graphs indicate that a mis-calibration, as high as even 100 mm, does not result in any significant loss in accuracy. To decouple the mis-calibration errors with any intrinsic error in our VF system, in Figure 9 (d) we plot the distance of the mis-calibrated projection to the projection obtained by using perfect calibration. Thus offsetting for the inherent errors in the system, it helps us understand the *variation* in the tool projection, purely as a function of C-arm mis-calibration. It can be observed that on an average, the tool tip projection moves by less than a pixel (0.44 mm) for mis-calibration as high as even 100 mm. Figure 9 (e) plots the error in the VF system as a function of the distance between the tool tip and the FTRAC fiducial used for the registration. As indicated by Equation 20, there is a slight increase in the error of the mis-calibrated VF system as the distance between

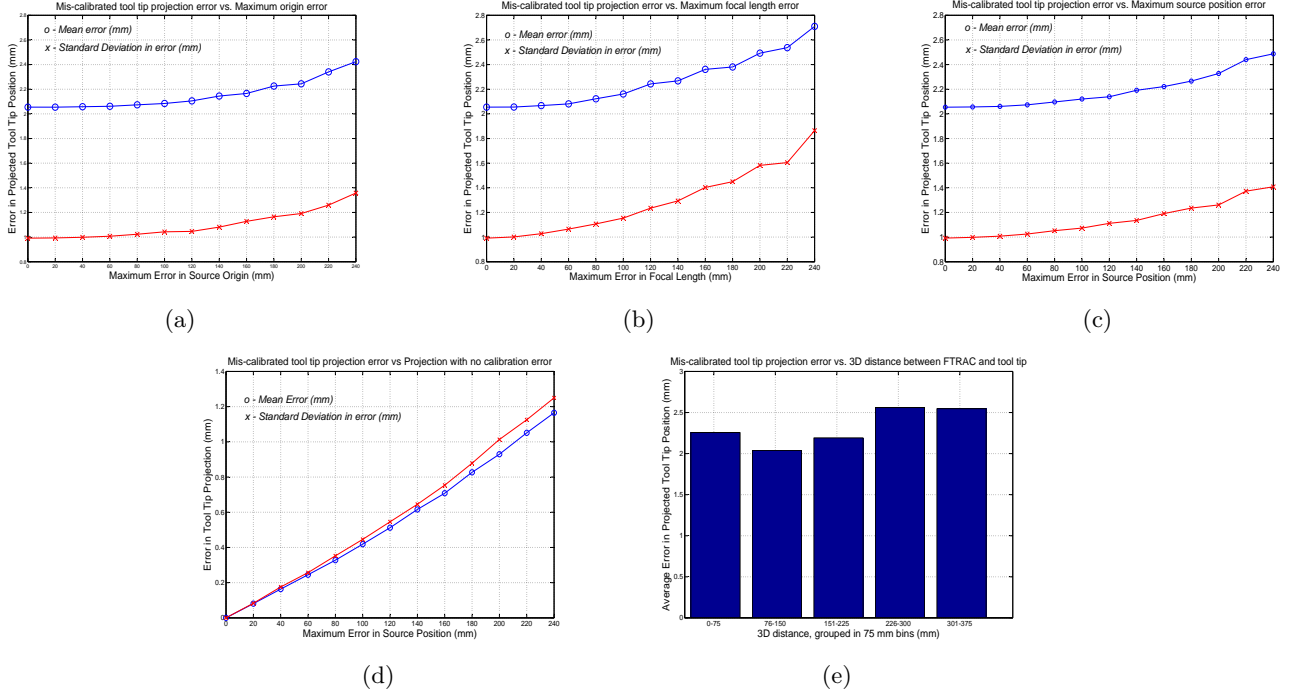


Figure 9. The error in a virtual fluoroscopy system using a total of 40,500 samples plotted as a function of mis-calibration in (a) C-arm origin ; (b) C-arm focal length ; (c) origin & focal length together. It can be noticed that VF guidance is practically independent of mis-calibration. (d) The *additional* error in the VF system is plotted as a comparison to the projection with the perfect calibration at each image. It can be noticed that the *additional* error due to mis-calibration is not significant, indicating that the primary sources of error are from other sources like tool tracking or tracker-fluoroscope registration. (e) The error in the VF system plotted as a function of the distance between the anatomy (tool-tip) from the registration fiducial. Typical patient thickness of 300 mm does not add any significant error to the system.

the tool-tip and the fiducial goes over 300 mm. Nevertheless, this increase is only marginal (less than a pixel), indicating a significant amount of robustness to the tool-tip position. Both graphs in Figure 9 (d)-(e) use the same data as used in (c). Thus, it can be concluded that mis-calibration as high as 50 mm does not add any significant amount of additional error in a VF system. Moreover, this additional error can tolerate a 350 mm distance from the tracked-tool to the registration fiducial, a number representing typical patient sizes.

Distortion Correction: With the distortion correction phantom attached to the intensifier, 86 C-arm images in a 25° cone around the AP-axis were acquired at a 5° separation. The average distortion in the images was found to be 3.31 mm with a standard deviation of 1.41 mm. Figure 10 (a) plots the average variation in the image distortion from one pose to another, as a function of angular image separation. Based on the two methods suggested in Section 2.3, Figure 10 (b), (c) plot the performance of each algorithm as a function of the repeatability of C-arm pose. The center-image distortion correction function reduces the average distortion in the image to an average value of 0.63 mm (STD 0.33 mm), using just a single center image in a 25° cone. The mean-image distortion correction function performs better, reducing the residual distortion error to an average of 0.48 mm (STD 0.3 mm). Though the center-image correction method is less accurate than the mean-image correction method, it has the convenience of using just a single pre-operative image *near* the intended region of C-arm use. Thus the results indicate that using a single distortion correction image can reduce the average distortion error in the image from 3.31 mm to 0.63 mm when the intra-operative C-arm pose can be repeatably positioned with 25° accuracy, which is sufficiently acceptable for many applications. The use of a mean-image by utilizing multiple images *close* to the intended region of use, can further decrease this error to 0.48 mm, though

at the expense of collecting multiple images in the region. Note that these numbers for residual distortion errors are close to the resolution of the X-ray images (0.44 mm).

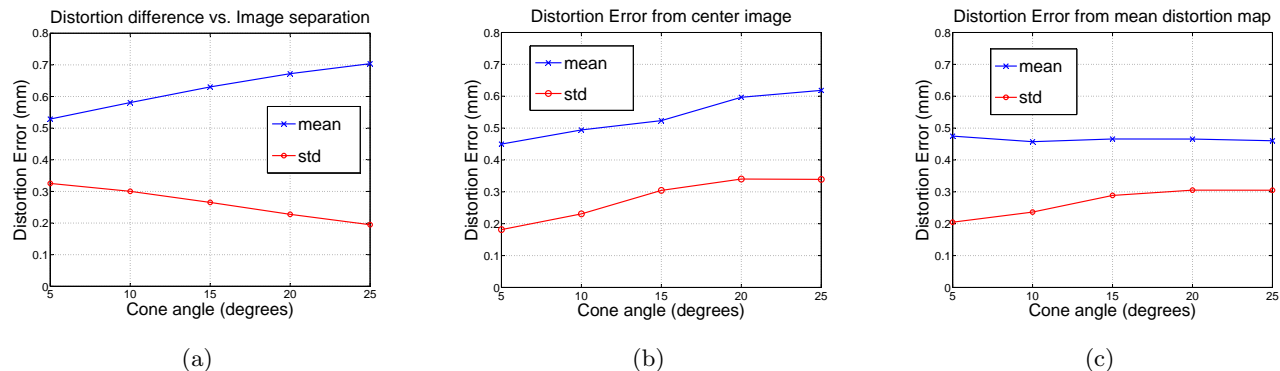


Figure 10. (a) The variation in C-arm distortion from one pose to the other as a function of angular separation. We notice that distortion is *continuous* and does not change radically near a certain neighborhood. (b) The performance of using the geographic center-image for distortion correction of all images in a region. The residual error in distortion is shown as a function of pose repeatability (cone half-angle). Only a single image is needed for distortion correction in the whole neighborhood of interest. (c) The performance (residual error) of using a computed mean-distortion map for the correction of all images inside a region. Multiple pre-operative distortion correction images in the region will be needed to compute an estimate of the mean distortion.

4. CONCLUSION

We modelled the the effects of mis-calibration on as an affine transform, and proved its validity experimentally on a variety of common fluoroscopy procedures involving C-arm tracking, 3D reconstruction or virtual fluoroscopy. We have derived bounds on the amount of scaling, translation and rotation error. For pose dependant calibration, we proved that using the mean calibration minimizes the reconstruction variance. Phantom experiments with a radiographic fiducial indicate that C-arm tracking is insensitive to mis-calibrations. We also showed that mis-calibration up to 50 mm adds no additional error in 3D reconstruction of small objects, beyond which the reconstructed objects begin to drift wrt the fiducial, while still retaining the shape. For the case when external trackers are used in conjunction with C-arms, we showed that mis-calibrations of up to 50 mm are still acceptable if the tool-projection is kept in the center of the image or if the tracker-fluoroscope registration phantom is kept close to the patient anatomy. Experimentally, we showed that virtual fluoroscopy can tolerate mis-calibrations as high as 100 mm. Furthermore, to address the problem of pose dependant distortion correction, we propose the use of a mean-image, reducing the distortion close to 1 pixel error. In conclusion, a significant family of quantitative fluoroscopy applications involving localization of small markers can function without cumbersome on-line calibration. A constant loose calibration might suffice.

5. ACKNOWLEDGMENTS

This work has been supported by DoD PC050170 - Prostate Cancer Research Program (2005) pre-doctoral Traineeship Award, NIH SBIR 1R43CA099374 01, NSF EEC-9731478.

REFERENCES

1. R. Hofstetter, M. Slomczykowski, M. Sati, and L. Nolte, “Fluoroscopy as an imaging means for computer-assisted surgical navigation,” *CAS* **4**(2), pp. 65–76, 1999.
2. J. Yao, R. H. Taylor, and et al, “A c-arm fluoroscopy-guided progressive cut refinement strategy using a surgical robot,” *Comput Aided Surg* **5**(6), pp. 373–90, 2000.

3. R. Fahrig and et al, "Three-dimensional computed tomographic reconstruction using a c-arm mounted XRII: correction of image distortion," *Med Phys.* **24**(7)(-), pp. 1097–106.
4. H. Livyatan, Z. Yaniv, and L. Joskowicz, "Robust automatic c-arm calibration for fluoroscopy-based navigation: A practical approach," in *MICCAI*, pp. 60–68, 2002.
5. J. Siewerdsen, M. Daly, G. Bahar, D. Moseley, G. Bootsma, S. Chhabra, D. Jaffray, and J. Irish, "Multimode c-arm fluoroscopy, tomosynthesis, and cone-beam ct for image-guided interventions: from proof of principle to patient protocols," in *SPIE Medical Imaging; Physics of Medical Imaging*, Feb 2007.
6. R. Kumar and A. Hanson, "Sensitivity of the pose refinement problem to accurate estimation of camera parameters," in *ICCV90*, pp. 365–369, 1990.
7. E. Malis, "Visual servoing invariant to changes in camera intrinsic parameters," *IEEE Transaction on Robotics and Automation* **20**, pp. 72–81, Feb 2004.
8. J. C. Eyke and et al., "Computer-assisted virtual fluoroscopy," *The University of Pennsylvania Orthopaedic Journal* **15**, pp. 53–59, 2002.
9. G. Chintalapani, A. Jain, and R. Taylor, "Statistical characterization of c-arm distortion with application to intra-operative distortion correction," in *SPIE Medical Imaging; Visualization, Image-Guided Procedures, and Display*, Feb 2007.
10. A. Jain, T. Mustufa, Y. Zhou, E. C. Burdette, G. Chirikjian, and G. Fichtinger, "A robust fluoroscope tracking (ftrac) fiducial," *Med Phys* **32**, pp. 3185–98, Oct 2005.

A Cheap and Easy Method for 3D C-arm Reconstruction using Elliptic Curves

David Burkhardt^a, Ameet Jain^b, Gabor Fichtinger^b

^aHaverford College

^bJohns Hopkins University

ABSTRACT

For quantitative C-arm fluoroscopy, we had earlier proposed a unified mathematical framework to tackle the issues of pose estimation, correspondence and reconstruction, without the use of external trackers. The method used randomly distributed unknown points in the imaging volume, either naturally present or induced by placing beads on the patient. These points were then inputted to an algorithm that computed the 3D reconstruction. The algorithm had an 8° region of convergence, which in general could be considered sufficient for most applications. Here, we extend the earlier algorithm to make it more robust and clinically acceptable. We propose the use of a circle/ellipse, naturally found in many images. We show that the projection of elliptic curves constrain 5 out of the 6 degrees of freedom of the C-arm pose. To completely recover the true C-arm pose, we use constraints in the form of point correspondences between the images. We provide an algorithm to easily obtain a virtual correspondence across all the images and show that two correspondences can recover the true pose 95% of the time when the seeds employed are separated by a distance of 40 mm. or greater. Phantom experiments across three images indicate a pose estimation accuracy of 1.7° using an ellipse and two sufficiently separated point correspondences. Average execution time in this case is 130 seconds. The method appears to be sufficiently accurate for clinical applications and does not require any significant modification of clinical protocol.

Keywords: Tracking, Localization, Registration, X-ray reconstruction, C-arm pose estimation

1. INTRODUCTION

With an approximate annual incidence of 220,000 new cases and 33,000 deaths prostate cancer continues to be the most common cancer in men in the United States.¹ For several decades, the definitive treatment for low risk prostate cancer was radical prostatectomy or external beam radiation therapy,² but low dose rate permanent seed brachytherapy (shortly brachytherapy thereafter in this document) today can achieve virtually equivalent outcomes.^{3,4} The success of brachytherapy chiefly depends on our ability to tailor the therapeutic dose to the patients individual anatomy. In contemporary practice, however, implant planning is based on idealistic preplanned seed patterns that, as 15 years of clinical practice has clearly demonstrated, are not achievable in the actual human body. According to a comprehensive review by the American Brachytherapy Society,⁵ the preplanned technique used for permanent prostate brachytherapy has limitations that may be overcome by intraoperative planning. At the same time, continues the re-port, the major current limitation of intraoperative planning is the inability to localize the seeds in relation to the prostate. There are excellent algorithmic and computational tools available today to optimize a brachytherapy treatment plan intraoperatively, thereby allowing for an improved dose coverage. These methods, however, critically require that the exact three-dimensional locations of the implanted seeds are precisely known with respect to the patients anatomy.

C-arm fluoroscopy is attractive as a means to generate this precise knowledge. It is the most widely used intraoperative imaging modality in general surgery. However, it presently lacks the ability for robust and easy quantitative guidance.

Further author information: (Send correspondence to Ameet Jain)

David Burkhardt: E-mail: dburkhar@haverford.edu

Ameet Jain: E-mail: ajain@cs.jhu.edu

Gabor Fichtinger E-mail: gabor@cs.jhu.edu

Quantitative fluoroscopy-guided surgery needs to solve four major problems: 1 C-arm image distortion; 2 the calibration of imaging parameters; 3 pose recovery or tracking; and 4 registration to imaging modalities. The first two are well-studied problems in the literature.⁶⁻⁸ In particular, it has been suggested that precise calibration of C-arm parameters do not significantly improve pose reconstruction.⁹ Through modeling the effects of mis-calibration as an affine transform, it is demonstrated that C-arm tracking is insensitive to mis-calibrations: mis-calibration of up to 50 mm adds no additional error in 3D reconstruction of small objects. A constant calibration can therefore be assumed for all images. On the other hand, pose recovery on unencoded C-arm machines is a major technical problem that presently does not have a clinically practical solution in many areas of application.

In current commercial C-arm fluoroscopy surgical navigation systems, pose recovery is performed through localizing the x-ray detector in room coordinates by some auxiliary optical tracker^{10,11} or electromagnetic EM tracker.¹² Unfortunately, auxiliary trackers sometimes become impractical for various reasons. They are expensive and add to the complexity of the operating room since they require an additional calibration step. Optical trackers require a line of sight, which becomes cumbersome in a clinical setting and requires an alteration in the standard work flow. The EM trackers can successfully overcome this issue, but become susceptible to field distortion from metal objects like surgical tools or the C arm itself, compromising on accuracy.

In a recent publication,¹³ the authors delineate the above problems and also say that using optical trackers reduces the useful imaging volume of the fluoroscope and potentially compromises the achievable accuracies. Despite using an optical tracker to track their surgical tools, they explicitly choose to not track the C arm using the tracker but instead use a radio-opaque fiducial. Their system has been fairly successful for various surgeries and has been in clinical use for the last four years. To make the fiducials feasible, recent publications have reported smaller fiducials by compact bead placement. In one study an artificially induced fiducial, consisting of several lines, seeds and ellipses, was demonstrated to be capable of uniquely determining correct C-arm pose with mean accuracy of .33° in rotation and .53 mm in translation.¹⁴

Solutions that require only objects naturally present in the image frame in the surgery room are more attractive still. In many applications, screw/needle ends, implanted surgical markers, special anatomy points etc. are naturally present in the images. By enforcing the "consistency" of these feature points across the images, one can potentially solve for all unknown parameters of calibration, pose recovery, matching, and reconstruction in one massive high-dimensional non-linear optimization. In particular, in the case of brachytherapy there are many seeds present that may be usable for optimization.

Accurate three dimensional reconstruction of the brachytherapy seeds requires that individual seeds be matched between multiple images. Seed matching can be formalized as a combinatorial optimization problem, and demonstrates that the Hungarian algorithm can be applied to match seeds between images. It is proved that, using the Hungarian algorithm, two images are insufficient to uniquely match seeds. Three images are necessary, and in practice more may be needed for the identification of seeds that are not visible in all images.¹⁵

Considerable work has been done in studying the usefulness of conic images in image reconstruction, both in segmenting conic curves in images and in determining pose based on successful segmentations.¹⁶⁻²⁴ It has been demonstrated that images of conics can be used in pose determination. In particular, it is possible to determine, to a single rotational degree of freedom, the pose from which an image was generated based on a single image of a circle within the image frame.²⁵

In this paper, we propose a solution to accurately estimate the pose by placing a wire in the shape of an elliptic curve in the imaging frame. We demonstrate that images of this ellipse constrain 5 of the 6 pose reconstruction degrees of freedom. Previously designed algorithms that determine a correspondence between brachytherapy seeds can be used to provide seed correspondences. These correspondences will be combined with a non-linear optimization to determine C-arm pose.

2. METHODS

2.1. Imaging Setup

A C-arm fluoroscope was used to generate three images of an artificial brachytherapy seed cloud to be used to test our ability to reconstruct C-arm pose. A fiducial device that includes two wire ellipses is placed in the



Figure 1. Fiducial device containing wire ellipses, and seed cloud phantom to be used in assessing algorithm. Within the phantom cloud block are precisely positioned sample seeds.

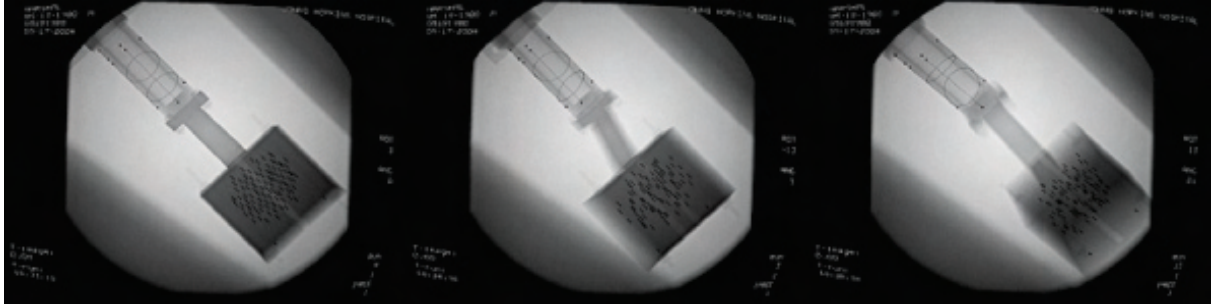


Figure 2. Three sample C-arm Images of a phantom brachytherapy seed cloud and fiducial with ellipse

imaging frame, and is used to create an image of an ellipse in each C-arm image. The design for the fiducial was refined by generating multiple rough prototypes from ABS acrylonitrile butadiene styrene using an FDM fused deposition modeling rapid prototype machine. The final fiducial design was then fabricated from a acetol rod using a four-axis CNC computer numerical control mill. The cylinder was press fit into a custom acetol mount that provided three mutually orthogonal sets of mounting holes for attaching to an accurate rotary table for validation. The dimensions of the ellipse were precisely controlled in its manufacture.

The brachytherapy seed cloud was modeled by a highly precise phantom. Real x-ray images were taken of the phantom using a fluoroscope Philips BV 3000. The system-supplied parameters were read from the DICOM header, otherwise the fluoroscope was not explicitly calibrated. Moreover, the images were not distortion corrected distortion 2 mm. The fiducial was mounted on a highly accurate 0.002° resolution rotational turntable 30000 Heavy Load Worm Gear Drive from Parker Automation, Irwin, Pennsylvania. The fluoroscope remains stationary while the fiducial moves in a known path, providing ground truth. The fiducial with seed cloud phantom attached is shown in Figure 1 A sample set of three images produced by this set-up is presented in Figure 2.

A fiducial mount was designed such that it produced zero translation and a known rotation when the turntable was rotated. The design supported the two independent rotation axes typical to C arms. Thus, given any starting pose, the relative motion between the current pose and the starting pose is known precisely from the turntable reading. The relative motion is also calculated using our algorithm from computed current pose and the computed starting pose. The difference between the computed relative motion and known relative motion is the error.

2.2. Reconstruction Algorithm Design

An algorithm was designed and executed on the C-arm images to reconstruct pose. Previously designed segmentation algorithms were used to determine the location of the ellipse and the brachytherapy seeds in the images. These algorithms produced ellipses equations of the form:

$$Au^2 + Buv + Cu^2 + Du + Fv + G = 0 \quad (1)$$

in each image, in which u and v are respectively the coordinates along the x and y axis of the image, measured in pixels, and A, B, C, D, F , and G are constants determined by the algorithm. This equation and the assumed C-arm calibration can be used to determine the equation of the three dimensional cone which has as vertex the focal point of the X-ray source. This equation will be

$$A_0x^2 + B_0xy + C_0y^2 + \frac{D_0}{f}xz + \frac{F_0}{f}yz + \frac{G_0}{f^2}z^2 = 0. \quad (2)$$

where x, y, z are coordinates in a system that has the focal point of the x-ray device as origin with z axis perpendicular to the image plane and x and y axis parallel to the imaging plane, and f is the focal length of the imaging scenario. This equation can be represented in matrix form as

$$\begin{bmatrix} x & y & z \end{bmatrix} \begin{bmatrix} A_0 & \frac{B_0}{2} & \frac{D_0}{2f} \\ \frac{B_0}{2} & C_0 & \frac{F_0}{2f} \\ \frac{D_0}{2f} & \frac{F_0}{2f} & \frac{G_0}{f^2} \end{bmatrix} \begin{bmatrix} x \\ y \\ z \end{bmatrix} = 0. \quad (3)$$

Given the dimensions of the ellipse, our task was to find the transformation between a coordinate system centered on the physical ellipse with x axis along its major axis and y axis along its minor axis and the system with origin at the imaging focal point and with x axis along the image x axis of the image, y axis along the image y axis of the image, and z axis perpendicular to the image plane.

We broke the process into several steps using a method similar to that described for the case of a circle by Costa and Shapiro.²⁵ The first step involved finding the rotation between the system of coordinates defined by the image plane, and the system with x and y axes along the major and minor axis of the cone and z axis along the cone's center. This coordinate system is of particular interest because in it the cone equation is of the form:

$$\begin{bmatrix} x & y & z \end{bmatrix} \begin{bmatrix} A_B & 0 & 0 \\ 0 & C_B & 0 \\ 0 & 0 & \frac{G_B}{f^2} \end{bmatrix} \begin{bmatrix} x \\ y \\ z \end{bmatrix} = 0 \quad (4)$$

Having the equation in this form makes it easier to work with in the next step. The rotation matrix that achieves it is just the eigenvectors of the original cone matrix M_0 , since multiplying a matrix by one of its eigenvectors and right multiplying by the transpose of that same matrix produced a diagonalized version of the initial matrix.

We next sought to find the transformation between this coordinate system with z axis perpendicular to the cone base and one with z axis perpendicular to the surface of the physical wire ellipse. Through applying constraints imposed by the ellipse, we sought to find the set of transformations that would achieve this for a given image. We parameterized the problem by defining two values, ϕ and θ which together can represent a rotation from the frame with axis aligned with the cone base to any other axis system. The coordinate system is first rotated by ϕ about the z axis of the original coordinate system, then by θ around the new y axis. This relationship is demonstrated in Figure 3 For any image, there are infinitely many possible $\phi - \theta$ combinations, corresponding to infinitely many possible physical ellipses that could generate a given ellipse image. These rotations can be expressed by the following matrices:

$$R_\phi = \begin{bmatrix} \cos(\phi) & -\sin(\phi) & 0 \\ \sin(\phi) & \cos(\phi) & 0 \\ 0 & 0 & 1 \end{bmatrix} \quad (5)$$

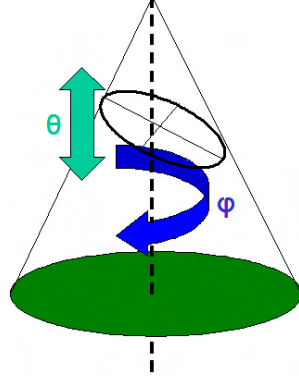


Figure 3. Graphical representation of the angles phi and theta, used in pose reconstruction

$$R_\theta = \begin{bmatrix} \cos(\theta) & 0 & \sin(\theta) \\ 0 & 1 & 0 \\ -\sin(\theta) & 0 & \cos(\theta) \end{bmatrix} \quad (6)$$

Our goal therefore is to solve for ϕ and θ such that:

$$X R_\phi R_\theta M_P R_\phi^T R_\theta^T X^T = 0 \quad (7)$$

Where M_P is the equation for the cone in the coordinate system with z axis perpendicular to the actual ellipse. We have several constraints related to this cone that we can put in place to determine the set of $\phi - \theta$ solutions. We know that any plane parallel to the x - y plane will slice the cone in a section with eccentricity equal to the eccentricity of the physical ellipse, and this eccentricity is a known constant. So, if we set Z constant we will get the equation of an ellipse with eccentricity. Doing this gives us:

$$A_P * x^2 + B_P * xy + C_P * y = K \quad (8)$$

$$A_P = G_0 * \sin^2(\theta) + C_0 * \cos^2(\theta) \sin^2(\phi) + A_0 * \cos^2(\theta) \cos^2(\phi) \quad (9)$$

$$B_P = 2\{-A_0 * \cos(\theta) \cos(\phi) * \sin(\phi) + C_0 * \cos(\theta) \sin(\phi) \cos(\phi)\} \quad (10)$$

$$C_P = A_0 * \sin^2(\phi) + C_0 * \cos^2(\phi) \quad (11)$$

The ellipse generated in this slice will be described by the equation:

$$\frac{(x * \cos(\psi) + y * \sin(\psi))^2}{a^2} + \frac{(x * \sin(\psi) - y * \cos(\psi))^2}{b^2} = K \quad (12)$$

With ψ as some rotation angle, and a and b as the major and minor axes of the real ellipse. K will be some constant dependent on the z value at which the slice was taken Expanding this equation gives us:

$$\left(\frac{\cos^2(\psi)}{a^2} + \frac{\sin^2(\psi)}{b^2}\right) x^2 + \sin(2\psi) \left(\frac{1}{a^2} - \frac{1}{b^2}\right) xy + \left(\frac{\sin^2(\psi)}{a^2} + \frac{\cos^2(\psi)}{b^2}\right) y^2 = K \quad (13)$$

So, we know that for some angle of rotation ψ :

$$\begin{aligned}
A_P &= \left(\frac{\cos^2(\psi)}{a^2} + \frac{\sin^2(\psi)}{b^2} \right) \\
B_P &= \sin(2\psi) \left(\frac{1}{a^2} - \frac{1}{b^2} \right) \\
C_P &= \left(\frac{\sin^2(\psi)}{a^2} + \frac{\cos^2(\psi)}{b^2} \right)
\end{aligned}$$

We can combine these statements to place a constraint on the allowed values of these constants relative to each other: trigonometric identities allow us to say that:

$$\begin{aligned}
A_P + C_P &= K \left(\frac{1}{a^2} + \frac{1}{b^2} \right) \\
(A_P - C_P)^2 + B_P^2 &= K^2 \left(\frac{1}{a^2} - \frac{1}{b^2} \right)^2 \\
A_P + C_P &= K \left(\frac{1}{a^2} + \frac{1}{b^2} \right) \\
(A_P - C_P)^2 + B_P^2 &= K^2 \left(\frac{1}{a^2} - \frac{1}{b^2} \right)^2
\end{aligned}$$

These can be combined to say that:

$$\frac{(A_P - C_P)^2 + B_P^2}{(A_P + C_P)^2} = \frac{(\frac{b^2}{a^2} - 1)^2}{(\frac{b^2}{a^2} + 1)^2}$$

Substituting the values for A_P , B_P , and C_P previously presented in equations 9, 10, 11 allows us to obtain an equation relating θ to ϕ . This equation is a quadratic equation in $\cos^2(\phi)$ of the form:

$$0 = K_1(\theta) * \cos^4(\phi) + K_2(\theta) * \cos^2(\phi) + K_3(\theta) \quad (14)$$

With the $K_n(\theta)$ functions of θ defined as follows:

$$K_1 = -4 * (-C_P + A_P)^2 * \frac{a}{b} * (1 - 2 * \cos(\theta)^2 + \cos(\theta)^4) / (\frac{a}{b} + 1)^2 \quad (15)$$

$$\begin{aligned}
K_2 &= \frac{(\frac{a}{b} - 1)^2}{(\frac{a}{b} + 1)^2} * (G_P * \sin(\theta)^2 + C_P * \cos(\theta)^2)^2 + \frac{(\frac{a}{b} - 1)^2}{(\frac{a}{b} + 1)^2} * A_P^2 + 2 \frac{(\frac{a}{b} - 1)^2}{(\frac{a}{b} + 1)^2} * (G_P * \sin(\theta)^2 + \\
&C_P * \cos(\theta)^2) * A_P - (G_P * \sin(\theta)^2 + C_P * \cos(\theta)^2)^2 - A_P^2 + (2 * G_P * \sin(\theta)^2 + 2 * C_P * \cos(\theta)^2) * A_P \quad (16)
\end{aligned}$$

$$\begin{aligned}
K_3 &= -4 * (2 * \frac{a}{b} * G_P * C_P * \cos(\theta)^2 - 2 * \frac{a}{b} * G_P * C_P * \cos(\theta)^4 - A_P * C_P * \cos(\theta)^2 - A_P * G_P \\
&+ A_P * G_P * \cos(\theta)^2 + \frac{a}{b} * C_P^2 * \cos(\theta)^4 + a/b * G_P^2 - 2 * \frac{a}{b} * G_P^2 * \cos(\theta)^2 + \frac{a}{b} * G_P^2 * \cos(\theta)^4 \\
&- A_P * \frac{a}{b^2} * C_P * \cos(\theta)^2 - A_P * \frac{a^2}{b} * G_P + A_P * a/b^2 * G_P * \cos(\theta)^2 + A_P^2 * \frac{a}{b}) / (\frac{a}{b} + 1)^2 \quad (17)
\end{aligned}$$

Since 14 is a quadratic equation in $\cos^2(\phi)$, for any given value of ϕ there are 4 values of θ that satisfy the constraint that it imposes. After choosing a $\phi - \theta$ combination to consider, we apply these transformations to our coordinate system. This gives us a cone equation of the form:

$$XR_\phi R_\theta M_P R_\phi^T R_\theta^T X^T = XC_E X^T = 0 \quad (18)$$

Where C_E is the cone in a coordinate system with z axis perpendicular to the face of the real ellipse. We next apply a rotation by the angle ψ to bring the x and y axes of our coordinate system parallel to the major and minor axes of the real ellipse. To solve for ψ , we solve for the values that sets B_E to 0. This angle is given by:

$$\psi = 1/2 * \text{atan}(2 * B_E / (C_E - A_E)) \quad (19)$$

Transforming the coordinate system by a rotation around the z axis of the angle ψ , which is described by the transformation matrix:

$$\begin{bmatrix} \cos(\psi) & -\sin(\psi) & 0 & 0 \\ \sin(\psi) & \cos(\psi) & 0 & 0 \\ 0 & 0 & 1 & 0 \\ 0 & 0 & 0 & 1 \end{bmatrix} \quad (20)$$

The coordinate system created by the combination of these rotations now has axes parallel to the axes of the real ellipse, but is centered at the imaging focal point. The final step in our algorithm is therefore a translation to bring the center of the coordinate system to the center of the ellipse. This translation is computed by taking a slice of the cone a distance f away from the focal points, computing its major axis at this point, and using this computation to determine where on the cone a slice would have major axis equal to the major axis of the actual real ellipse. The coordinate system is then translated by this vector.

Combining these transformations allows us to create an algorithm to determine the set of possible poses that could have created a given image. However, as infinitely many possible $\phi - \theta$ combinations exist, the ellipse image can not be used to uniquely determine the pose. It constrains 5 of the 6 degrees of freedom of pose, allowing a single degree of freedom that must be removed through further constraints.

To constrain this set to a single solution, additional information is necessary. Correspondences between points in the brachytherapy seed cloud can be used to create the necessary additional constraints. We designed an algorithm that could take as input a proposed set of poses and a set of corresponding point images, and determine the actual three-dimensional location of the image points, and the error in point segmentation that this set of poses would imply. By optimizing for minimal projection error, we were able to determine possible poses that might produce the images observed.

3. RESULTS

The algorithm was tested using C-arm images of a phantom brachytherapy seed cloud near a metal ellipse. Initially, trials were run with only one additional point correspondence. This seemed like an attractive possibility since this correspondence could come from the mean location of all segmented seeds and might allow for the seed correspondence step to be bypassed. With only one additional point correspondence, the algorithm succeeded in only 9 of 20 cases, indicating that a single correspondence is insufficient to satisfactorily resolve pose. Sets of 2 and 3 seeds were selected at random, and were used in the optimization function to attempt to reconstruct C-arm pose. Average distance between the points used in optimization was measured and recorded. A sample reconstruction is presented in Figure 4.

With the addition of other point correspondence, the success of the algorithm was shown to depend considerably on the distance between the two points being used. The algorithm was defined to have succeeded if

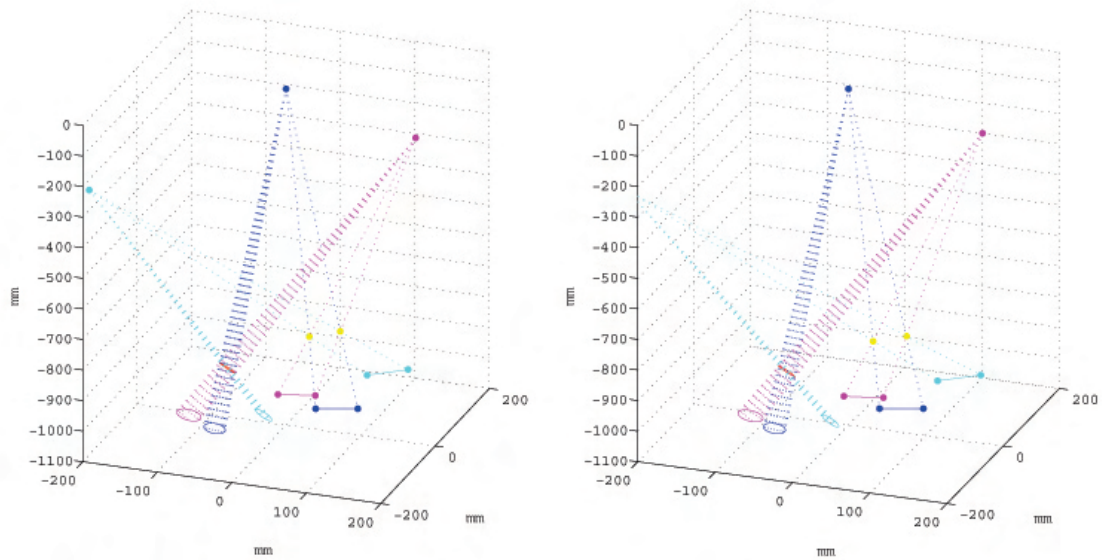


Figure 4. Sample representation of the pose reconstruction from the images presented in Figure 2. On left is the ground truth, while on right is the reconstructed pose. Each of the cone vertices represents an x-ray source, while the cone bases represent ellipse images. The three cones intersect at the location of the real ellipse. The points are points used to generate additional constraints; their images lie in plane with the ellipses to which they correspond

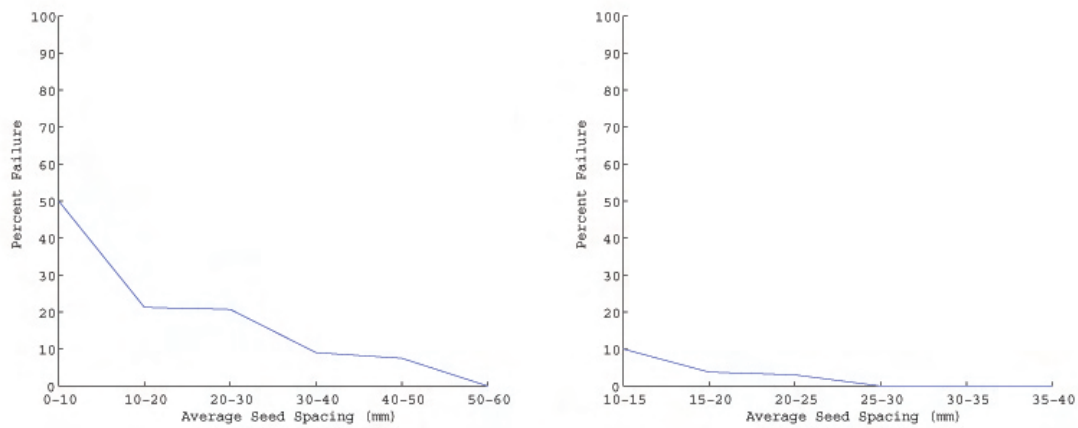


Figure 5. Observed rate of failure. On the left are the results from optimizing using 2 brachytherapy seeds, and on the right are results produced using 3 brachytherapy seeds. X axis is the average spacing between seeds used.spacings

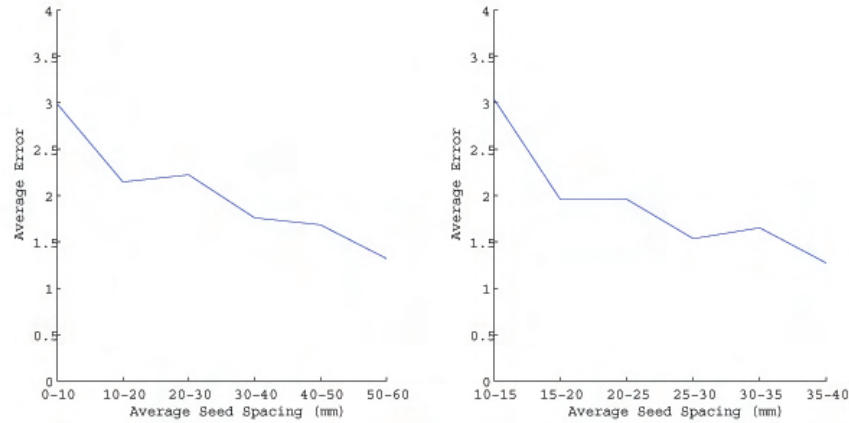


Figure 6. Observed Angular Error in non-failure cases for 2 and 3 brachytherapy seeds, using sets of seeds with various average spacings

the average error in reconstructed pose as compared with actual pose was less than 7° . The rate at which the algorithm was able to successfully reconstruct pose is presented as a function of bead spacing in Figure 5. As this figure demonstrates, for most cases with 2 points, or for cases with 3 points and wide spacing, failure rate becomes quite low. For those cases in which pose was reconstructed, the average angular error still did display some dependence on seed spacing and number of seeds used in reconstruction. This relationship is presented in Figure 6.

4. DISCUSSION

An algorithm has been presented that is capable of determining C-arm pose from three images of a single ellipse and correspondences between additional points. Coupled with previous work that enables point correspondence matching, this algorithm could be applied to reconstruct C-arm pose for three images of a brachytherapy patient, with a single artificially manufactured wire ellipse of known dimension as the only addition to the imaging situation. This represents a significant step toward a complete pose reconstruction system employing no external hardware.

An aim of further work might be to determine the number of point correspondences that should be theoretically required to exactly determine pose. In addition, it would be desirable to include the ellipse into the error calculation process; further work could focus on determining the effective weightings that should be given to the points and to the ellipse in such an error calculation.

REFERENCES

1. A. Jemal, "Cancer statistics," *Ca-Cancer J. Clin* **54**, pp. 8–29, 2004.
2. R. Peschel and J. Coldberg, "Surgery, brachytherapy, and external-beam radiotherapy for early prostate cancer," *Lancet. Oncol.* **4**, pp. 233–241, 2002.
3. G. Merrick, W. Butler, J. Lief, and A. Dorsey, "Is brachytherapy comparable with radical prostatectomy and external-beam radiation for clinically localized prostate cancer?," *Tech. Urol.* **7**, pp. 12–19, 2001.
4. J. Blasko, T. Mate, J. Sylvester, P. Grimm, and W. Cavanagh, "Brachytherapy for carcinoma of the prostate: Techniques, patient selection, and clinical outcomes," *Seminal Radiation Oncology* **12**, pp. 81–94, 2003.
5. S. Nag, J. Ciezki, R. Cormack, S. Doggett, K. DeWyngaert, G. Edmundson, R. Stock, N. Stone, Y. Yu, and M. Zelefsky, "Intraoperative planning and evaluation of permanent prostate brachytherapy: Report of the american brachytherapy society," *Int. J. Radiat. Oncol., Biol. Phys.* **51**, pp. 1422–1430, 2001.

6. R. Hofstetter, M. Slomezykowski, M. Sati, and L. Nolte, "Fluoroscopy as an imaging means for computer-assisted surgical navigation," *Comput. Aided Surg.* **4**, pp. 65–76, 1999.
7. T. Tang, "Calibration and point-based registration of fluoroscope images," Master's thesis, Queen's University, 1999.
8. J. Yao, R. Taylor, R. Goldberg, R. Kumar, A. Bzostek, R. Vorhis, and P. Kazanzides, "Conic reconstruction and correspondence from two views," *Computer Aided Surgery* **5**, pp. 373–390, 2001.
9. A. Jain, R. Kyon, Y. Zhou, and G. Fichtinger, "C-arm calibration - is it really necessary?," *MICCAI*, pp. 639–646, 2005.
10. Brainlab, Inc., Heimstetten, Germany, *Vector Vision*.
11. Medtronic Surgical Navigation Technologies, Louisville, CO., *StealthStation*.
12. GE Healthcare, Waukesha, WI, *OEC 9800 FluoroTrak*.
13. R. Phillips, A. Mohsen, W. Viant, S. Malek, Q. Li, N. Shah, M. Bielby, and K. Sherman, "A phantom based approach to fluoroscopic navigation for orthopaedic surgery," *MICCAI*, pp. 621–628, 2004.
14. A. Jain, T. Mustafa, Y. Zhou, C. Burdette, G. Chirkjian, and G. Fichtinger, "Ftrac - a robust fluoroscope tracking fiducial," **32**, pp. 3185–3198, 2005.
15. A. Jain, Y. Zhou, T. Mustafa, C. Burdette, G. Chirikjian, and G. Fichtinger, "Matching and reconstruction of brachytherapy seeds using the hungarian algorithm," **32**, pp. 3475–92, 2005.
16. J. Wright, A. Wagner, S. Rao, and Y. Ma, "Homography from coplanar ellipses with application to forensic blood splatter reconstruction," *cvpr* **1**, pp. 1250–1257, 2006.
17. P. K. Mudigonda, C. V. Jawahar, and P. J. Narayanan, "Geometric structure computation from conics," *Lancet. Oncol.* **4**, pp. 233–241, 2002.
18. L. Quan, "Conic reconstruction and correspondence from two views," *IEEE-PAMI* **18**, 1996.
19. F. Kahl and A. Heyden, "Using conic correspondence in two images to estimate the epipolar geometry," in *ICCV*, pp. 761–766, 1998.
20. S. D. Ma, "Conics-based stereo, motion estimation, and pose determination," *International Journal of Computer Vision* **10**, pp. 7–25, 1999.
21. A. Fitzgibbon, M. Pilu, and R. B. Fisher, "Direct least square fitting of ellipses," *Pattern Analysis and Machine Intelligence* **21**, pp. 476–480, 1999.
22. E. S. Maini, "Robust ellipse-specific fitting for real-time machine vision," *IEEE Transactions on Pattern Analysis and Machine Intelligence* **25**, pp. 1343–1348, 2003.
23. G. Jiang, H. Tsui, L. Quan, and A. Zisserman, "Geometry of single axis motions using conic fitting," *Lecture notes in computer science* **3704**, pp. 318–327, 2005.
24. R. Hu and Q. Ji, "Camera self-calibration from ellipse correspondences," *Proceedings of the 2001 IEEE International Conference on Robotics and Automation*, 2001.
25. M. S. Costa and L. G. Shapiro, "3d object recognition and pose with relational indexing," *Computer Vision and Image Understanding* **79**, pp. 364–407, 2000.

Statistical Characterization of C-arm Distortion with Application to Intra-Operative Distortion Correction

Gouthami Chintalapani, Ameet K. Jain and Russell H. Taylor

Dept. Of Computer Science, The Johns Hopkins University
Baltimore, USA

ABSTRACT

C-arm images suffer from pose dependant distortion, which needs to be corrected for intra-operative quantitative 3D surgical guidance. Several distortion correction techniques have been proposed in the literature, the current state of art using a dense grid pattern rigidly attached to the detector. These methods become cumbersome for intra-operative use, such as 3D reconstruction, since the grid pattern interferes with patient anatomy. The primary contribution of this paper is a framework to statistically analyze the distortion pattern which enables us to study alternate intra-operative distortion correction methods. In particular, we propose a new phantom that uses very few BBs, and yet accurately corrects for distortion.

The high dimensional space of distortion pattern can be effectively characterized by principal component analysis (PCA). The analysis shows that only first three eigen modes are significant and capture about 99% of the variation. Phantom experiments indicate that distortion map can be recovered up to an average accuracy of less than 0.1 mm/pixel with these three modes. With this prior statistical knowledge, a subset of BBs can be sufficient to recover the distortion map accurately. Phantom experiments indicate that as few as 15 BBs can recover distortion with average error of 0.17 mm/pixel, accuracy sufficient for most clinical applications. These BBs can be arranged on the periphery of the C-arm detector, minimizing the interference with patient anatomy and hence allowing the grid to remain attached to the detector permanently. The proposed method is fast, economical, and C-arm independent, potentially boosting the clinical viability of applications such as quantitative 3D fluoroscopic reconstruction.

Keywords: distortion, intra-operative distortion correction, principal component analysis, eigen modes

1. INTRODUCTION

C-arm fluoroscopy is the most commonly used intra-operative imaging modality because of its low cost and ease of use. These fluoroscopic images are distorted and need to be corrected for use in quantitative intra-operative analysis. This distortion is caused mainly due to the curved nature of the detector resulting in radial or pin cushion type of distortion and due to the earth's magnetic field deflecting the electrons resulting in an S-curve distortion. Boone *et al.* and Gutierrez *et al.* discuss the actual physical phenomenon that causes distortion. Moreover, C-arm distortion is pose-dependant, i.e., it varies with the position of the C-arm.

Several C-arm distortion correction techniques have been proposed in literature¹⁻⁷ dating back to 90's. Typically, a dense grid pattern phantom with either metal beads,^{1,3-6} or grooves² is attached rigidly to the image intensifier and is imaged at different C-arm poses. A polynomial, usually a two-dimensional fourth or fifth order polynomial depending on the number of beads in the phantom, is used to model the distortion by mapping the bead coordinates in the fluoroscopic phantom image to the correct geometrical coordinates of the phantom. An interpolation function is then used to define the distortion map for all the pixels in the image. These techniques are robust and are very effective for offline distortion correction.

These grid-based methods become cumbersome for intra-operative use (such as for 3D reconstruction), since the grid pattern either significantly corrupts the patient's image, or necessitates two X-ray shots at each pose (one with and the other without the grid). Fahrig *et al.* proposes to track C-arm, create a look up table for

Send correspondence to E-mail: greddy@cs.jhu.edu

a distortion map at each pose and then interpolate the near-by poses to determine the distortion map intra-operatively. This method is fast and overcomes the above mentioned issues, but requires the C-arm to be encoded accurately. The other option would be to remember the poses for which the distortion is measured offline and then repeat the procedure intra-operatively.² This method requires that the C-arm is tracked and the pose is repeatable. Intra-operative C-arm tracking could be slow and expensive.

In this paper, we propose a statistical framework which enables us to analyze the distortion maps at different poses and extract any inherent patterns. We have performed principal component analysis to create a statistical model for distortion patterns exhibited by a C-arm. Although C-arm distortion patterns appear to be random and complicated, our analysis shows that they can be predicted from the principal modes of variation with a very decent accuracy. In particular, we present a novel intra-operative distortion correction application with a phantom which uses very few beads on the periphery of the C-arm image intensifier along with the prior statistical knowledge. This method is fast, economical, and C-arm independent, potentially boosting the clinical viability of applications such as quantitative 3D fluoroscopic reconstruction. The motivation for this work (effective distortion correction) might become obsolete in case of flat panel detector C-arms which would replace existing C-arms in future. However, we believe that this work presents a statistical framework to characterize the distortion patterns effectively and to build applications based on this analysis.

2. STATISTICAL CHARACTERIZATION OF C-ARM DISTORTION

2.1. Method

We have designed a grid phantom with steel beads, approximately 300 beads, placed at 1 cm distance between beads in a square pattern. Several fluoroscopic phantom images were taken in various C-arm poses by rigidly attaching the phantom to the image intensifier. A basic image processing algorithm is used to segment the bead positions in all the images. These segmented bead positions are referred to as image coordinates (u_d, v_d) . The actual/nominal bead positions, (u_o, v_o) , are determined from the physical geometry of the grid phantom and the distortion is modeled using a fifth order Bernstein polynomial as shown in the following equation.

$$(u_d, v_d) = \sum_{i=0}^n \sum_{j=0}^n C_{ij} B_{ij}(u_0, v_0) \quad (1)$$

where

$$B_{ij}(u_0, v_0) = \binom{n}{i} u_0^i (1 - u_0)^{n-i} \binom{n}{j} v_0^j (1 - v_0)^{n-j}$$

For each image, a bezier matrix B is constructed using the nominal coordinates of the bead positions and the above equation can be written in matrix form as follows:

$$(U_{obs})_{m \times 2} = (B(U_{nom}))_{m \times (n+1)^2} \times C_{(n+1)^2 \times 2} \quad (2)$$

where U_{obs} is the array of distorted bead coordinates in the image; U_{nom} represents the nominal coordinates of the beads; and m being number of grid points on the phantom (here $m = 300$).

Define a distortion vector as

$$\Delta \vec{d} = (\Delta u, \Delta v) = (u_d, v_d) - (u_0, v_0)$$

The coefficient matrix C can be computed in least squares sense which minimizes the error $\Delta \vec{d}$ for each grid point. This polynomial effectively models the distortion. After computing the polynomial, the distortion vectors for each pixel in the distorted image is computed using 2 and the image is sampled in the resulting distortion map to create a rectified image. In practice, this technique has proved to be robust and accurate with sub-pixel accuracy.

This procedure is repeated for all the images acquired at different C-arm poses to create distortion maps. In order to extract patterns from these distortion maps, we have performed principal component analysis. The data matrix for this analysis is created by vectorizing the image matrix (distortion map) and by stacking each vector into a matrix Δ as shown below:

$$\Delta = \begin{pmatrix} \Delta u_{11} & \Delta u_{12} & \cdot & \cdot & \cdot & \Delta u_{1k} \\ \cdot & \cdot & \cdot & \cdot & \cdot & \cdot \\ \cdot & \cdot & \cdot & \cdot & \cdot & \cdot \\ \Delta u_{m1} & \Delta u_{m2} & \cdot & \cdot & \cdot & \Delta u_{mk} \\ \Delta v_{11} & \Delta v_{12} & \cdot & \cdot & \cdot & \Delta v_{1k} \\ \cdot & \cdot & \cdot & \cdot & \cdot & \cdot \\ \cdot & \cdot & \cdot & \cdot & \cdot & \cdot \\ \Delta v_{m1} & \Delta v_{m2} & \cdot & \cdot & \cdot & \Delta v_{mk} \end{pmatrix}$$

where $(\Delta u_{ij}, \Delta v_{ij})$ is the distortion vector of the i_{th} pixel in the j_{th} image; m is the number of pixels in the image; and k is the number of images.

For computational issues, we have ignored the background pixels and have only considered the pixels in the active area of the C-arm detector while creating the data matrix. The mean distortion map is computed by taking average of all the distortion maps. This mean value is then subtracted from the data matrix to make it a zero mean data matrix, which is essential for principal component analysis. Principal modes of variation (eigen modes) are then extracted from the covariance matrix of the input data matrix.⁸ From this analysis, we can express any distortion map as a linear combination of the principal modes.

$$\Delta \vec{d} = M_0 + \sum_{i=1}^n \lambda_i D_i \quad (3)$$

where M_0 is the mean distortion map and D_i is the i^{th} principal component. The orthogonal eigen modes represent new basis for the subspace in which the C-arm distortion patterns exist as compared to the very high dimensional parameterization using polynomials. For example, a two dimensional fifth order Bernstein polynomial has 72 coefficients.

2.2. Results

We have performed principal component analysis on two sets of distortion maps extracted from the grid phantom images. For the first dataset, we have collected 120 images of the phantom, approximately one every 3 degrees along the propeller axis of an OEC 9600 C-arm. We have relied on the gradation marks on the C-arm to position the C-arm and did not use any trackers/encoders. This would be a typical dataset for 3D reconstruction with 2D fluoroscopic images. For the OEC 9600 C-arm, there are two data outputs: 1) DICOM output through floppy and 2) video output through a frame grabber. Typically, floppy output is slow but accurate as compared to the fast but noisy video signal. The image size is 459x484 pixels and 480x720 pixels for floppy and video outputs respectively and the pixel size is 0.44 after distortion correction. We have compared both the dicom and the video images to verify that the video signal does not affect the distortion. All these images were corrected using a fifth order Bernstein polynomial. We then extracted the distortion maps for each image and performed principal component analysis on these distortion maps as explained above.

This analysis shows that the first three principal modes of variation are significant and they capture about 99% of the variation as shown in Figure 1(a). Figure 1(b) shows the results of leave-out validation test. In this test, of the 120 training images, we have used 60 images, roughly every 6 degrees, to create a statistical model and then fit this model to the remaining 60 images. The error measurement between the true distortion map and the one estimated from the model is given by

$$\epsilon = \left\| \Delta \vec{d} - \left(M_0 + \sum_{i=1}^n \lambda_i D_i \right) \right\|^2 \quad (4)$$

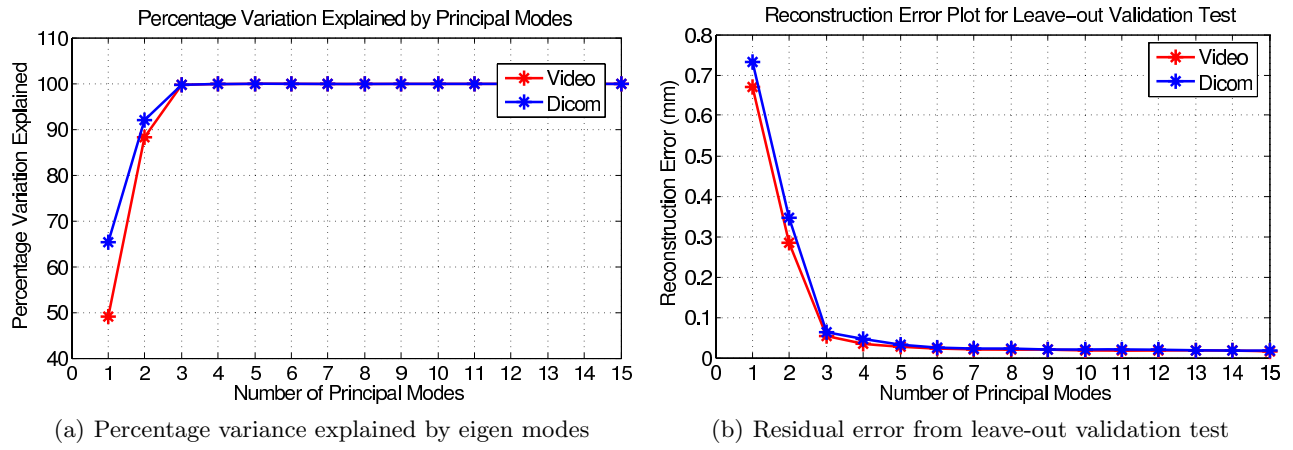


Figure 1. Principal component analysis on distortion maps. (a) Percentage variation explained by the dominant eigen modes. Note that the first three modes capture about 99% of the variation. (b) Residual error plot after projecting the leave-out distortion map onto the eigen space as function of number of modes. The average error is less than 1mm when the first three principal modes are used. Note that the results from dicom and video images are very similar.

The average raw distortion as measured from the grid phantom is about 2.1488 mm/pixel with a standard deviation of 1.1469 mm/pixel and a maximum distortion of 4.6003 mm/pixel. With the leave-out validation test, we were able to achieve an average distortion correction accuracy of about 0.0632 mm/pixel and a standard deviation of 0.0294 mm/pixel with a maximum distortion of 0.202 mm/pixel using the first three dominant eigen modes. The residual errors for video images were close to the ones from DICOM images and hence validating the fact that either output can be used for statistical analysis. These results indicate that eventhough the C-arm distortions are complicated and high-dimensional, they can be represented by the eigen modes and can be predicted fairly accurately.

The actual distortion modes from the principal modes are shown in Figure 2.2. The first principal mode appears similar to barrel distortion, second mode represents S-curve distortion and the third mode looks like a spiral distortion. We have predominantly noticed S-curve distortion in all the images taken with that C-arm. While collecting the data, we have noticed that the images were rotating in one direction until halfway and then in opposite direction for the rest of the sweep. We came to know from the manufacturer that as we move the "C" through it's propeller angles, there is a shift of weight from the bearings on one side of the detector assembly, to the bearing set on the opposite side. This causes a sudden jump and also rotates the images through the sweep. We have included this as part of the distortion model because there is no other way to explicitly measure these inconsistencies and to our surprise these inconsistencies showed up in the mode distribution plots for the mode weight parameters (Figure 2.2). The Figure 3(a) clearly shows the rotational aspect of the C-arm through the propeller axis which is in agreement with the first mode (barrel distortion due to the curvature of the detector). This distortion is more or less assumed to be constant.^{4,9} The rotation caused by the gantry can be clearly seen in this plot. The jump motion can be attributed to the jumps in plots given in Figures 3(b) and 3(c).

For the other experiment, we have collected 200 images distributed more or less uniformly in the sphere spanned by the "C" of the C-arm. We have captured only video images this time as it was convenient to copy images using the frame grabber. Similar eigen analysis on this data says that the first four eigen modes capture 99% of the variation. The distortion maps defined by the principal modes are shown in Fig 2.2. The first two modes look like barrel distortion along x, y dimensions respectively. The second mode shows the S-curve and the third mode is similar to spiral distortion. From the leave-out validation test, we are able to achieve an average accuracy of 0.07 mm/pixel, with 0.0553 mm/pixel standard deviation and 0.3578 mm/pixel maximum distortion, comparable to the results from the first dataset.

These two datasets are collected with the same phantom on the same C-arm in the same room but at different time periods. The C-arm is displaced with in the room during this time. Qualitatively, the distortion patterns from these two datasets look similar. In order to compare the distortion patterns quantitatively, we measured the

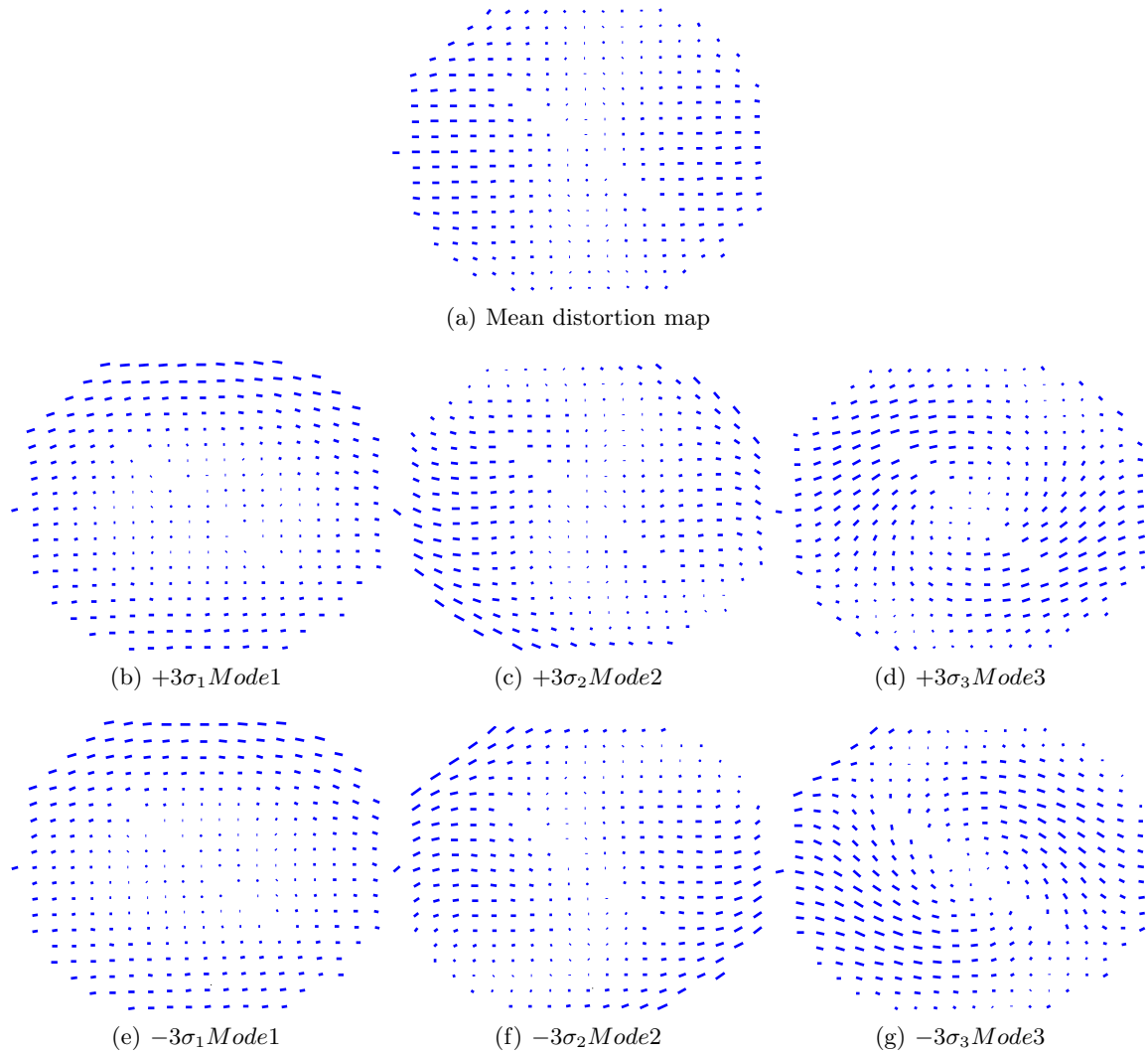


Figure 2. Distortion maps as shown by the first three eigen modes from principal component analysis. The first mode is similar to barrel distortion, second mode appears close to an S-curve distortion and the third mode shows spiral distortion

projection errors using equation (4) by projecting one dataset on to the other subspace. This measure quantifies how well one model can generalize the data from the other model. The average distortion correction accuracy is 0.2329 mm/pixel, with a standard deviation of 0.1157 mm/pixel and a maximum distortion correction of 0.6589 mm/pixel. These results show that the statistical model created from the volume data is capable of modeling the distortion patterns extracted from the full sweep data acquired at a different time. These results strongly indicate that the C-arm distortion patterns are not random and can be predicted with reasonable accuracies. A more controlled experiment with the same C-arm at different locations would provide more insights into this problem.

3. A NOVEL INTRA-OPERATIVE DISTORTION CORRECTION APPLICATION

Building upon the statistical framework presented in the previous section, we present a new intra-operative distortion correction method with a phantom that uses very few beads. We propose a new phantom design with beads on the periphery of the image intensifier. These beads can be arranged in any pattern (circular, square etc). The main idea is to use the prior statistical knowledge and the beads to drive the distortion correction process. This design suits intra-operative needs very well because it has very minimal interference with patient

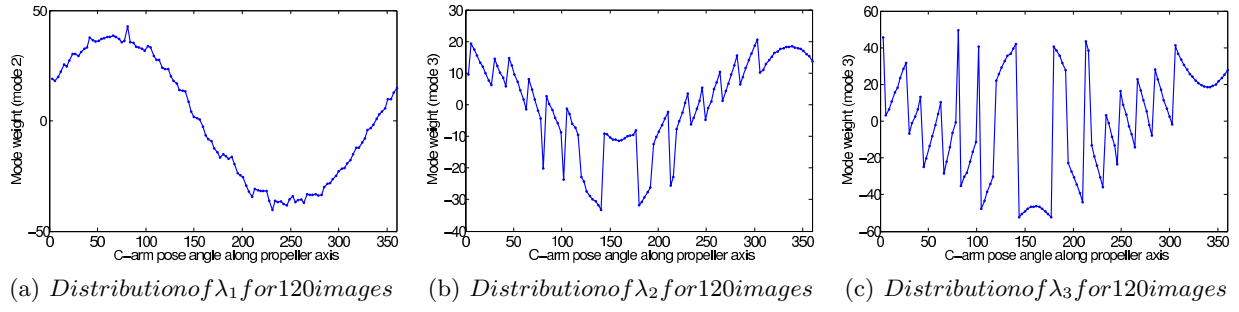


Figure 3. Distribution of the mode weight parameters for 120 images from a full sweep along the propeller axis

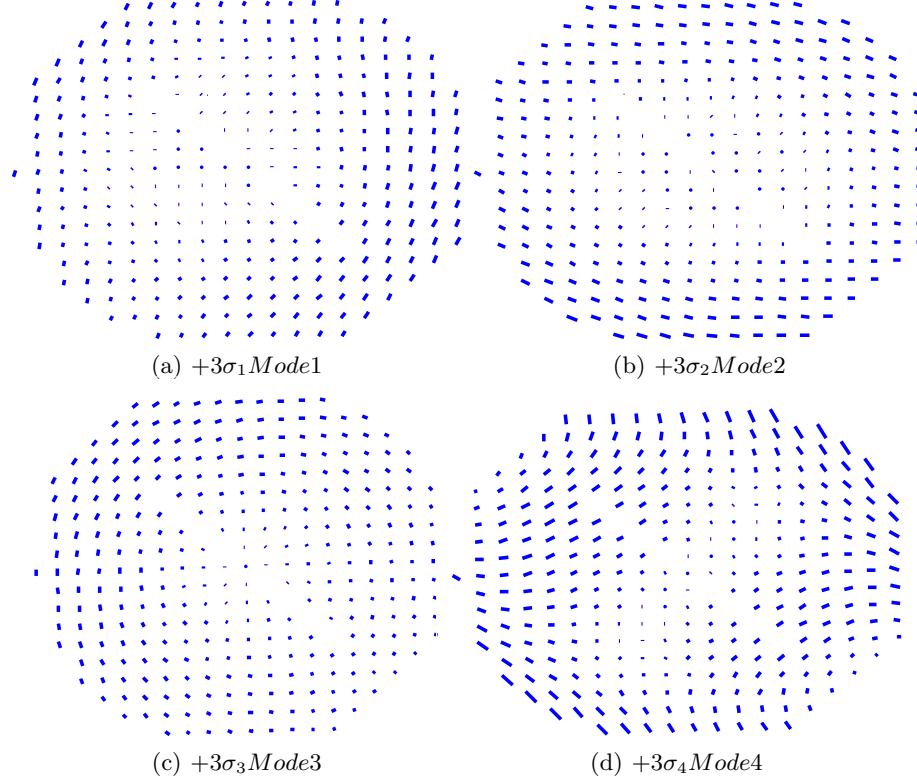


Figure 4. Distortion maps as shown by the first four eigen modes from principal component analysis. The first two modes represent barrel distortion in x,y directions, second mode shows S-curve type of distortion and the third mode is spiral distortion

anatomy and hence allows the grid to remain attached to the detector through out the surgery. The proposed method is fast, economical, and C-arm independent, potentially boosting the clinical viability of applications such as quantitative 3D fluoroscopic reconstruction. Figure 3 shows our simulation results on the number of beads needed to recover distortion parameters using the prior knowledge. In this simulation, we have used images from the full sweep dataset. Of the 120 images, we have used 60 images to create the mean distortion map and the distortion modes. The remaining 60 images were used to do distortion correction. A band of pixels was selected in each of these 60 images, from which "n" number of pixels were selected as bead locations. These pixels are selected randomly and for each experiment we have performed 100 trials for all the 60 images. For each iteration, we have optimized mode weights by minimizing a similarity measure. The similarity measure is determined by the "squareness" of the bead locations. By squareness, the bead locations after correction should be on a line and the lines should be orthogonal. In this optimization step, there is no information about

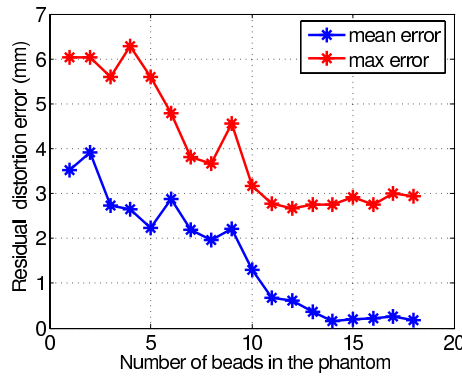


Figure 5. Residual distortion correction error as function of number of beads used for correction

the orientation of the phantom with respect to the image intensifier and hence the bead locations were made to fit a specific pattern, for example a square. We have used downhill simplex optimization method in MATLAB 7.0 with the search space being defined by the distortion modes from PCA. A linear combination of the modes would give a distortion map. This distortion map is interpolated to determine the rectified locations for the beads using bilinear interpolation. The results indicate that as few as 14 or 15 beads are required to recover the distortion parameters with an average accuracy of 0.17 mm/pixel and a maximum of 2.86 mm/pixel, accuracy sufficient for most clinical applications. The maximum error is high because the objective function is not able to capture the distortions. A slight modification to the objective function incorporating the orientation of the phantom might improve the results significantly.

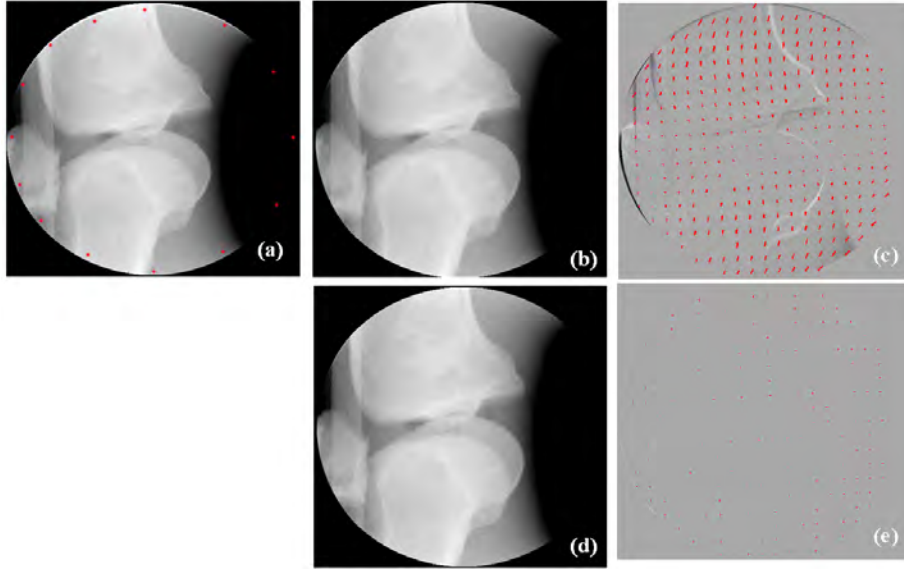


Figure 6. Simulation of the new phantom design. (a) shows the fluoroscopic image of a knee with the phantom beads highlighted in red (b) distortion corrected image using the dense grid phantom (c) true distortion map overlaid on difference image ((a)- (b)). (d) distortion corrected image using the beads from (a) and statistical modes (e) residual distortion map after correction using new phantom overlaid on the gray scale difference image ((c)-(d))

4. CONCLUSIONS AND FUTURE WORK

In this paper, we have presented a statistical framework to analyze C-arm distortion patterns. Principal component analysis on distortion maps at different orientations of the C-arm reveal the inherent patterns. Our results from two datasets indicate that even though the distortion patterns are high dimensional and complicated, they can be predicted fairly accurately using the first three to four principal modes. This analysis can be easily extended to study the distortion patterns over time, and at different locations and across different C-arms, adding more dimensions to the problem. Such analysis would give better insights in to modeling distortion patterns effectively. Apparently, this work is not applicable to flat panel detector C-arms. Nevertheless, any one using non-flat-panels have to go through the tedious distortion correction procedure. In such cases, we consider that this statistical approach would address most of the current issues with the C-arm distortion correction.

We have described a novel intra-operative distortion correction method that uses a phantom with very few beads. Our simulation experiments have shown that as few as 15 beads can recover the distortion parameters with an average accuracy of 0.17 mm/pixel. This new phantom has very minimal interference with the patient anatomy and hence can remain attached to the C-arm during surgery. We believe that this method is fast and practical and can be used effectively for intra-operative applications such as 3D reconstruction. Moving further away from the phantoms, another approach would be to do a phantom less distortion correction of patient images using patient CT as a fiducial. The 2D views from 3D patient CT can be compared to the actual x-ray images of the patient to optimize the distortion modes, hence catering to the needs of intra-operative applications.

ACKNOWLEDGMENTS

This work is supported in part by NSF ERC Grant EEC9731478, by NIH/NIBIB research grant R21-EB003616 and by DOD PC050170. We would also like to thank Iulian Iordachita for making the calibration phantom and Gabor Fichtinger for his assistance in this project.

REFERENCES

1. R. Fahrig, M. Moreau, and D.W. Holdsworth, "Three-dimensional computed tomographic reconstruction using a c-arm mounted xrii: correction of image intensifier distortion," *Med Phys*, vol. 24(7), pp. 1097–106, 1997.
2. J. Yao, R.H. Taylor, R.P. Goldberg, R. Kumar, A. Bzostek, R.V. Vorhis, P. Kazanzides, and A. Gueziec, "Robust automatic c-arm calibration for fluoroscopy-based navigation: A practical approach," in *Computer Aided Surgery (CAS)*, 2000, vol. 5(6), pp. 373–90.
3. H. Livyatan, Z. Yaniv, and L. Joskowicz, "Robust automatic c-arm calibration for fluoroscopy-based navigation: A practical approach," in *MICCAI*, 2002, vol. 2489, pp. 60–68.
4. L. F. Gutierrez, G. Shechter, R. J. Lederman, E.R. McVeigh, and C. Ozturk, "Distortion correction, calibration, and registration: Towards an integrated mr and x-ray interventional suite," in *Proc. of SPIE, Medical Imaging 2005: Visualization, Image-Guided Procedures, and Display*, 2005, vol. 5744, pp. 146–156.
5. S. Schreiner, J.H. Anderson, R.H. Taylor, J. Funda, A.Bzostek, and A.C. Barnes, "A system for percutaneous delivery of treatment with a fluoroscopically-guided robot," in *In Troccaz J, Grimson E, Mosges R, editors: Proceedings of First Joint Conference on Computer Vision, Virtual Reality and Robotics in Medicine and Medical Robotics and Computer Assisted Surgery (CVRMed-MRCAS' 97), Grenoble, France, March 1997*, 1997, pp. 747–756.
6. R. Hofstetter, M. Slomczykowski, M. Sati, and L. Nolte, "Fluoroscopy as an imaging means for computer-assisted surgical navigation," in *Proc. of Computer Aided Surgery (CAS)*, 1999, vol. 4(2), pp. 65–76.
7. B. Schueler and X. Hu, "Correction for image intensifier distortion for three-dimensional x-ray angiography," in *Proc. of SPIE, Medical Imaging 1995*, 1995, vol. 2432, pp. 272–279.
8. I.T. Jolliffe, "Principal component analysis," Berlin: Springer Verlag, 1986.
9. Boone J.M., Seibert J.A., Barrett W.A., and Blood E.A., "Analysis and correction of imperfections in the image intensifier-tv-digitizer imaging chain," *Med Phys*, vol. 18, pp. 236–242, 1991.